5. SITE 964[1]

Shipboard Scientific Party[2]

HOLE 964A

Date occupied: 17 March 1995

Date departed: 18 March 1995

Time on hole: 1 day, 00 hr, 15 min

Position: 36°15.623′N, 17°44.990′E

Bottom felt (drill-pipe measurement from rig floor, m): 3668.7

Distance between rig floor and sea level (m): 11.1

Water depth (drill-pipe measurement from sea level, m): 3657.7

Total depth (from rig floor, m): 3770.5

Penetration (m): 101.8

Number of cores (including cores having no recovery): 11

Total length of cored section (m): 101.8

Total core recovered (m): 106.1

Core recovery (%): 104.2

Oldest sediment cored:
Depth (mbsf): 101.80
Nature: foraminifer-bearing nannofossil ooze
Earliest age: early Pliocene
Measured velocity (km/s): 1.62

HOLE 964B

Date occupied: 18 March 1995

Date departed: 19 March 1995

Time on hole: 13 hr

Position: 36°15.623′N, 17°45.000′E

Bottom felt (drill-pipe measurement from rig floor, m): 3669.4

Distance between rig floor and sea level (m): 11.1

Water depth (drill-pipe measurement from sea level, m): 3658.3

Total depth (from rig floor, m): 3771.4

Penetration (m): 102.0

Number of cores (including cores having no recovery): 11

Total length of cored section (m): 102.0

Total core recovered (m): 105.3

Core recovery (%): 103.2

Oldest sediment cored:
Depth (mbsf): 102.00
Nature: clay-bearing nannofossil ooze
Earliest age: early Pliocene

HOLE 964C

Date occupied: 19 March 1995

Date departed: 20 March 1995

Time on hole: 15 hr, 30 min

Position: 36°15.627′N, 17°45.007′E

Bottom felt (drill-pipe measurement from rig floor, m): 3671.4

Distance between rig floor and sea level (m): 11.1

Water depth (drill-pipe measurement from sea level, m): 3660.3

Total depth (from rig floor, m): 3776.5

Penetration (m): 105.1

Number of cores (including cores having no recovery): 12

Total length of cored section (m): 105.1

Total core recovered (m): 106.5

Core recovery (%): 101.0

Oldest sediment cored:
Depth (mbsf): 105.10
Nature: nannofossil ooze
Earliest age: early Pliocene

HOLE 964D

Date occupied: 20 March 1995

Date departed: 20 March 1995

Time on hole: 14 hr, 45 min

Position: 36°15.632′N, 17°45.000′E

Bottom felt (drill-pipe measurement from rig floor, m): 3671.4

Distance between rig floor and sea level (m): 11.1

Water depth (drill-pipe measurement from sea level, m): 3660.3

Total depth (from rig floor, m): 3780.0

Penetration (m): 108.6

Number of cores (including cores having no recovery): 12

Total length of cored section (m): 108.6

Total core recovered (m): 112.2

Core recovery (%): 103.3

Oldest sediment cored:
Depth (mbsf): 108.60
Nature: nannofossil ooze
Earliest age: early Pliocene

HOLE 964E

Date occupied: 20 March 1995

Date departed: 21 March 1995

[1]Emeis, K.-C., Robertson, A.H.F., Richter, C., et al., 1996. *Proc. ODP, Init. Repts.*, 160: College Station, TX (Ocean Drilling Program).
[2]Shipboard Scientific Party is given in the list preceding the Table of Contents.

Time on hole: 08 hr

Position: 36°15.647′N, 17°44.999′E

Bottom felt (drill-pipe measurement from rig floor, m): 3672.0

Distance between rig floor and sea level (m): 11.1

Water depth (drill-pipe measurement from sea level, m): 3660.9

Total depth (from rig floor, m): 3757.5

Penetration (m): 85.5

Number of cores (including cores having no recovery): 6

Total length of cored section (m): 53.0

Total core recovered (m): 54.3

Core recovery (%): 102.5

Oldest sediment cored:
Depth (mbsf): 85.50
Nature: nannofossil ooze
Earliest age: Pliocene

HOLE 964F

Date occupied: 21 March 1995

Date departed: 21 March 1995

Time on hole: 11 hr, 45 min

Position: 36°15.638′N, 17°45.025′E

Bottom felt (drill-pipe measurement from rig floor, m): 3668.4

Distance between rig floor and sea level (m): 11.1

Water depth (drill-pipe measurement from sea level, m): 3657.3

Total depth (from rig floor, m): 3696.5

Penetration (m): 28.1

Number of cores (including cores having no recovery): 3

Total length of cored section (m): 28.1

Total core recovered (m): 27.9

Core recovery (%): 99.4

Oldest sediment cored:
Depth (mbsf): 28.10
Nature: nannofossil ooze
Earliest age: Pleistocene

Principal results: Site 964 is located at the foot of the Calabrian Ridge near the Ionian Abyssal Plain on a small bathymetric high. Recovery and core quality in the six holes were excellent and a complete sediment section was recovered that spans the lower Pliocene to the Holocene. Outstanding features of the sequence recovered at Site 964 are the occurrence of more than 50 distinct sapropels in the composite section, numerous ash layers and ashy turbidites, and marked color banding of the sediments. The host sediments comprise light-colored (brownish to greenish) clayey nannofossil ooze, nannofossil ooze, and nannofossil clays. Some of the light-colored intervals are interpreted as normally graded turbidites (decimeters to meters thick). Tuffs are present as discrete beds and volcanic glass is disseminated throughout. The sapropels, which are centimeters to decimeters thick, are enriched in pyrite, plant material, and amorphous organic matter (up to 25% by weight organic carbon). Individual sapropels display a wide range of depositional and postdepositional features that include lamination, bioturbation, and oxidation fronts ("burn-down").

Stratigraphic control was achieved using calcareous nannofossils and planktonic foraminifers; siliceous microfossils were not found. The 16 biostratigraphic events recognized in Hole 964A range from the late early Pliocene to the late Pleistocene and Holocene. Based on composite depth, the resulting age vs. depth relationship reveals that the sedimentation rate at Site 964 varied between 4 and 73 m/m.y., with an average of 30 m/m.y. The recovered sequence promises an excellent record of Pliocene to Holocene sapropel formation that can be integrated with land sections.

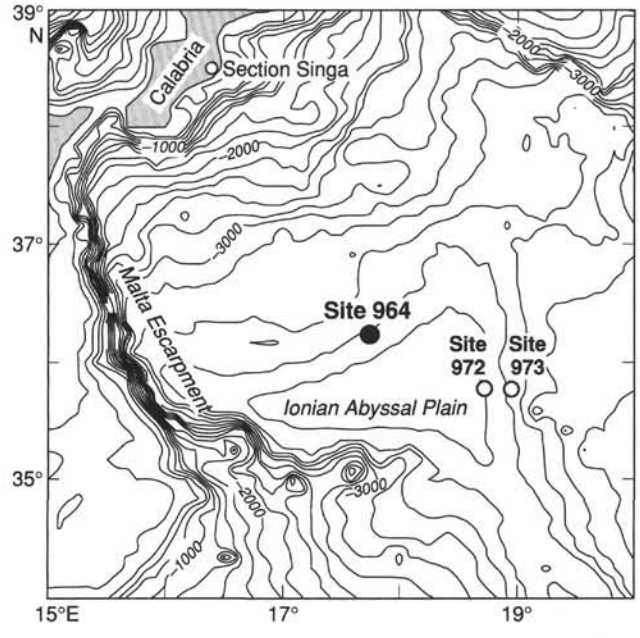

Figure 1. Location map of Site 964 on the Calabrian Ridge in the Ionian Basin. Bathymetry is from the ETOPO5 data set.

BACKGROUND AND OBJECTIVES

Site 964 is located at the foot of the Calabrian Ridge in water 3650 m deep (Fig. 1; see "Geological Setting" section, this chapter). The location was chosen to recover a sedimentary record of sapropel formation in the Ionian Basin. It also is the deep-water member of a longitudinal and depth transect across the Mediterranean Sea (ODP Legs 160 and 161) and will help constrain environmental gradients (salinity, temperature, nutrients) and their chemical and paleontological expressions. The site is close to the present-day sources of deep-water formation in the Adriatic Sea, and it is close to the Pliocene to Pleistocene land sections of Vrica and Singa in Calabria, where extensive work on the stratigraphy of sapropels has been performed (e.g., Hilgen, 1991b; Rio et al., 1994).

Long gravity cores previously recovered from this location (*Marion Dufresnes* Cores KC01 and KC01B) document sapropel occurrences back to the middle Pleistocene (Castradori, 1993; Sanvoisin et al., 1993) and sedimentation rates of approximately 30 m/m.y. Because safety concerns limited penetration at Site 964 to 100 mbsf, the record at the site was expected to extend back into the early Pliocene. Our principal objective was to construct a detailed age model from the sedimentary record through continuous and highly resolved (resolution <1 k.y.) measurements of physical parameters (density, susceptibility, color) and sedimentological correlation, which can be linked to magnetostratigraphic and paleontological age models. Tying the composite section at Site 964 to the orbitally tuned stratigraphic record from the nearby land sections will provide a clearly defined yardstick of sapropel occurrence and character and variation in sediment properties through time. This yardstick will be tested and employed, with any necessary modifications, for all sites in the Eastern Mediterranean.

The sediments recovered at Site 964 will also be used to test two arguments made to support the hypothesis of anoxia for sapropel for-

mation. The first is that the onset of deposition of each sapropel interval may be diachronous and may occur later in shallow-water settings (<2000 m) than in deep basins (>2000 m), owing to the fact that anoxic conditions in bottom waters have taken time to ascend from the seafloor into the water column. This argument implies (1) that there should be relatively more sapropels in the section at Site 964 than in shallower water settings and (2) that the bases of coeval sapropel events are diachronous at different water depths. The lag between deep- and shallow-water sapropel initiation could be large enough to be discernible in high-resolution stratigraphic records.

The second argument holds that organic carbon concentration (%OC) and preservation will be enhanced in the deep basins relative to shallow-water settings, because organic matter preservation is enhanced under anoxic conditions. Indeed, %OC in individual sapropel intervals S1 to S8 of late Pleistocene age consistently shows a positive correlation with water depth over a range of 400 to 4000 m (Murat, 1991). Because the thickness of the sapropels does not vary systematically with depth, the increase in %OC cannot be attributed to lack of dilution with inorganic sedimentary constituents. Barring dilution and assuming constant time intervals for the shallow and deep sapropel settings, the positive correlation of %OC with water depth in coeval sapropels is difficult to explain without invoking anoxia, because the ratio of sinking to produced organic carbon decreases exponentially with depth in most marine settings (Suess, 1980). The hypothesis of enhanced preservation of organic matter in deep-water settings will be tested by organic geochemical and isotopic analyses of organic matter in coeval sapropels from both deep- and shallow-water settings.

Site 964 also serves as a watchdog for deep-water formation in the Eastern Mediterranean. One reason for the development of anoxic bottom-water conditions during times of sapropel formation may be that deep-water formation was impeded (Béthoux, 1993). Eastern Mediterranean Deep Water originates in the northern Adriatic Sea during the winter months. Cold, oxygen-rich, and relatively fresh surface waters sink, mix with deeper waters, and cascade into the Ionian Basin before spilling into the Levantine Basin at depth (see "Paleoceanography and Sapropel Introduction" chapter, this volume). Site 964 is ideally positioned to record variability in bottom-water formation and character through faunal, chemical, and isotopic proxy indicators in the sediments, as well as the physical properties of the sediments (e.g., nature of lamination).

GEOLOGICAL SETTING

Site 964 is located on the Pisano Plateau between the Beato Angelico Trough and the Raffaello Basin (Kastens, 1984; Blechschmidt et al., 1982; Fig. 2), adjacent to the Ionian Abyssal Plain located to the east and southeast. Some workers also refer to particularly the southern part of the Ionian Abyssal Plain as the Messina Abyssal Plain.

The bathymetry of the site indicates that it is located on a small ridge on the lower slope of the southern Calabrian Ridge, approximately 200 m above the level of the Ionian Abyssal Plain, which is approximately 35 km to the southeast. The site is on an area of enigmatic "cobblestone topography" and, as a result of hyperbolic seismic reflections, the deeper structure is poorly constrained. The precruise site-survey data and the underway seismic profiles reveal a strong reflector beneath a poorly resolved upper sedimentary unit (see "Site Geophysics" section, this chapter).

In this area, the floor of the Ionian Abyssal Plain is underthrust beneath the Calabrian arc, resulting in the detachment of deep-sea sediments to form an accretionary wedge (Finetti, 1982; H.G. Kahle and St. Mueller, unpubl. data; Fig. 3). The location of the site, elevated approximately 200 m above the floor of the Ionian Abyssal Plain, implies a location near the toe of the Calabrian accretionary wedge (Kastens, 1984). However, the site is located on Finetti's (1982) summary tectonic map well within his Ionian Abyssal Plain. It appears more likely that the actual size of the Ionian Abyssal Plain in the north is smaller than that depicted by Finetti. The discrepancy could be partly because no topographic trench is present in this area, and the distinction between the accretionary wedge and the abyssal plain is therefore blurred. Also, Finetti (1982; fig. 1) inferred a broad zone of "sliding" ahead of his accretionary front in some areas. This "sliding zone," possibly including Site 964, can be interpreted as lying within the toe of the accretionary wedge in that it would overlie the most frontal décollement.

The Ionian Abyssal Plain is underlain by thick Messinian evaporites and very thick (approximately 10 km) underlying sediments,

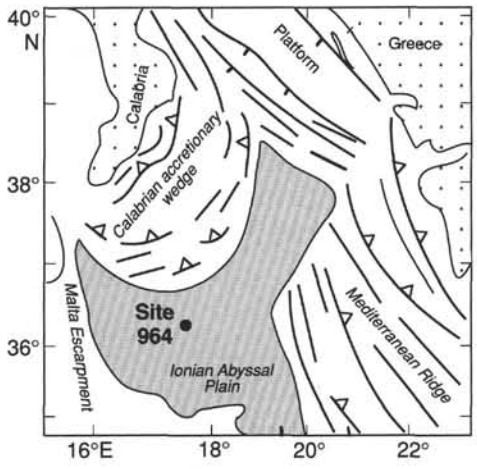

Figure 2. Outline tectonic map of the Calabrian Ridge in relation to the Ionian Abyssal Plain and the Mediterranean Ridge. Simplified from Finetti (1982). The site is located on the lower slope of the Calabrian accretionary wedge, and thus Finetti's figure needs modification.

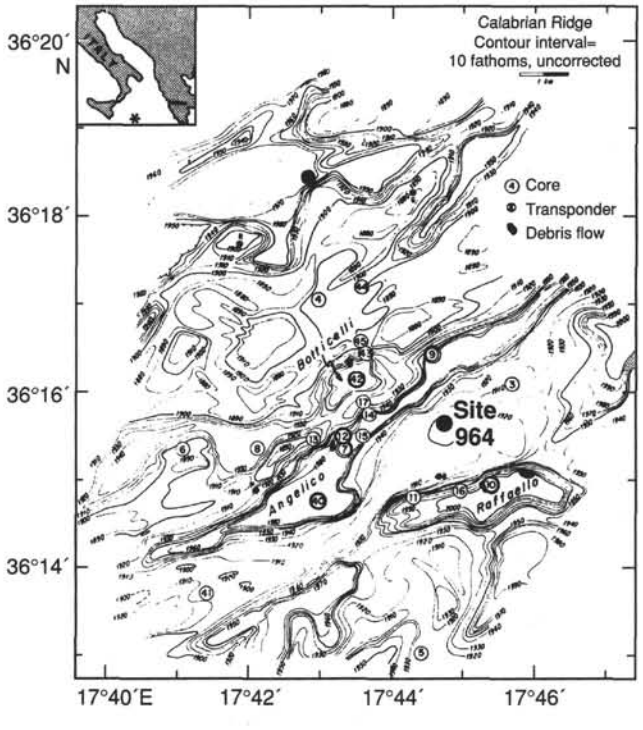

Figure 3. Bathymetric map of the vicinity of Site 964. From Blechschmidt et al. (1982).

which in turn are believed to overlie old Tethyan oceanic crust (Finetti, 1982), of either early or late Mesozoic age. H.G. Kahle and St. Mueller (unpubl. data) depicted this area as free of compressional deformation and as underlain by crust of questionable origin, possibly Tethyan oceanic crust in the south passing northward into a remnant of the Apulian continental margin.

The southern Calabrian Ridge was first explored in detail by Blechschmidt et al. (1982), who recovered 23 piston cores and dredge samples from the area adjacent to Site 694. The cores were taken on topographic highs, slopes, and the floors of basins and recovered upper Pliocene, Pleistocene, and Holocene sediments. The plateau cores contained fine-grained nannofossil-rich sediments with sapropels and tephra; the slope cores showed evidence of omission of Holocene age sediment; and the basinal cores contained a several-meter-thick layer of "homogenite." The homogenite is structureless and fine grained with a fining-upward sandy basal layer (Cita et al., 1982; Kastens and Cita, 1981). In addition, one core near the base of a slope contained numerous discrete debris flows. The above authors also pointed out that identical homogenites could be recognized in adjacent basins on the Calabrian Ridge over a distance of 300 km. One possibility is that the homogenites represent turbidites triggered by tsunamis (Kastens and Cita, 1981; Cita et al., 1982). Indeed, such turbidites could represent the distal effluents of very large turbidites deposited on the Ionian Abyssal Plain, with the dilute suspensions of fine sediment carried up the approximately 200-m slope onto the lower Calabrian Ridge by low-density turbidity currents. It is interesting to note that silt turbidites cored at Site 964 are similar in many respects to the homogenites (see "Lithostratigraphy" section, this chapter), and may well have had a similar origin.

Further evidence of Pliocene-Quaternary sedimentation came from a single long piston core from the Pisano Plateau close to Site 964 (Core KC01B). This core recovered 36.65 m of sediment, including nannofossil-rich ooze, tephra, and sapropels, extending back to 1.1 Ma.

Several hypotheses for the origin of the enigmatic cobblestone topography (Belderson et al., 1972; Kastens, 1981) have been proposed for both the Calabrian and Mediterranean Ridges: (1) as megaripples (Emery et al., 1966); (2) as olistostromes (Mulder et al., 1975); (3) as the result of subaerial karstification (Ryan, Hsü, et al., 1973); (4) as subaqueous karstification (Belderson et al., 1972); or (5) as mud diapirs and mud volcanoes (Camerlenghi et al., 1992). Blechschmidt et al. (1982) discounted each of these hypotheses for the southern Calabrian Ridge, and left the origin open. Based on a study of the northwestern Mediterranean Ridge west of Zakinthos, Stanley (1977) emphasized the role of neotectonic uplift in influencing the formation of cobblestone topography.

The "Summary and Conclusions" section (this chapter) for this site emphasizes the important paleoceanographic results and also notes that there is also significant information of tectonic interest. Indeed, the results of drilling at Site 964 show that the most likely explanation of the cobblestone topography in this area is that the complex seismic diffraction patterns reflect a highly irregular topography created by active tectonics related to uplift and faulting at the toe of the Calabrian accretionary wedge (Fig. 3). Indeed, the 3.5-kHz echo-sounder records show folding and increasing northward deformation across the boundary between the Ionian Abyssal Plain and the accretionary prism. This is typical of a compressional origin for such arc-parallel relief. Further evidence of this tectonic control comes from the large number of normal faults and a smaller number of reverse faults that were encountered at Site 964 (see "Structural Geology" section, this chapter). Many of these faults are oriented subparallel to the trend of the structures on the Calabrian Ridge near Site 964.

Further evidence of Pliocene-Quaternary vertical tectonics can be inferred from the sedimentary record cored at Site 964. The base of the cored interval was marked by a foraminifer sand of unknown depositional processes. Above this, nearly homogeneous turbidites consist mainly of resuspended nannofossil ooze (see "Lithostratigraphy" section, this chapter) and terrigenous silt (with admixed volcanic glass and other constituents). Such sediment could have accumulated from turbidity currents in a basinal setting near the toe of the accretionary wedge. By contrast, turbidites are absent from the upper part of the succession, which today is located on a high. The implication is that once-basinal sediments were uplifted to form the present small high. The existence of important extensional faults, as inferred from lithologic correlation between holes (see "Lithostratigraphy" section, this chapter), abundant small-scale faults, and minor occurrences of debris flows (three were noted; see "Structural Geology" section, this chapter) indicate such tectonic movements.

The floor of the Ionian Abyssal Plain is simultaneously being subducted both eastward beneath the toe of the Mediterranean Ridge and northwestward beneath the Calabrian Ridge (Fig. 3; H.G. Kahle and St. Mueller, unpubl. data). The décollement probably lies beneath the interval drilled at Site 964, as no structural evidence of its existence was observed in the cores (e.g., intense shearing, layer-parallel extension, dewatering). The available evidence thus indicates that Site 964 penetrated the upper plate of the toe of the Calabrian accretionary wedge (Fig. 4). The seafloor topography was initially subdued, possibly merging with the Ionian Abyssal Plain in the early Pliocene, which was followed by approximately 200 m of tectonic uplift accompanied by faulting during the Pliocene-Quaternary to form the present-day northeast-southwest-trending series of ridges and basins.

OPERATIONS

Transit to Site 964 and Site Survey

The 217-nmi sea voyage to Site 964 (proposed Site MEDSAP-3A) required 18.5 hr at an average speed of 11.7 kt. A seismic survey of 21 nmi was run over target Site MEDSAP-3A in 3.2 hr at 6.3 kt. A Datasonics 354M beacon (S/N 772, 15.0 kHz) was deployed at 2014 hr local time on 17 March 1995 at 36°15.612′N, 17°44.990′E.

Hole 964A

The first attempt at coring produced a water core with mud inside the shoe. The bit was lowered 5 m, and a 6.80-m core was recovered, indicating a seafloor depth of 3657.7 m by drill-pipe measurement. APC Cores 160-964A-1H through 11H were taken from 0 to 101.8 mbsf (Table 1), with 101.8 m cored and 106.12 m recovered (104.2% recovery). Cores were oriented from Core 160-964A-3H. The last two cores (160-964A-10H and 11H) were partial strokes with full recovery. The maximum gas detected was 4 ppm methane. There were no coring problems.

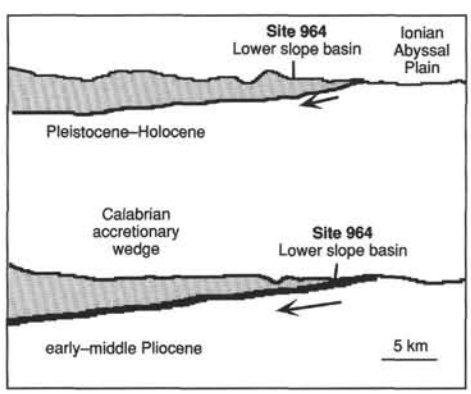

Figure 4. Simple tectonic sketch showing the inferred setting of Site 964 in the early-middle Pliocene and in the Pleistocene-Holocene. See text for explanation.

Table 1. Coring summary for Site 964.

Core	Date (March 1995)	Time (UTC)	Depth (mbsf)	Length cored (m)	Length recovered (m)	Recovery (%)
160-964A-						
1H	18	0850	0.0–6.8	6.8	6.80	100.0
2H	18	0950	6.8–16.3	9.5	9.78	103.0
3H	18	1050	16.3–25.8	9.5	9.85	103.0
4H	18	1155	25.8–35.3	9.5	9.97	105.0
5H	18	1300	35.3–44.8	9.5	9.89	104.0
6H	18	1400	44.8–54.3	9.5	9.95	105.0
7H	18	1455	54.3–63.8	9.5	9.98	105.0
8H	18	1600	63.8–73.3	9.5	9.91	104.0
9H	18	1700	73.3–82.8	9.5	9.90	104.0
10H	18	1815	82.8–92.3	9.5	10.06	105.9
11H	18	2030	92.3–101.8	9.5	10.03	105.6
Coring totals:				101.8	106.1	104.2
160-964B-						
1H	18	2215	0.0–8.1	8.1	8.10	100.0
2H	18	2320	8.1–17.6	9.5	9.83	103.0
3H	19	0010	17.6–27.1	9.5	9.79	103.0
4H	19	0110	27.1–36.6	9.5	9.77	103.0
5H	19	0225	36.6–46.1	9.5	10.03	105.6
6H	19	0325	46.1–55.6	9.5	9.86	104.0
7H	19	0415	55.6–65.1	9.5	9.73	102.0
8H	19	0535	65.1–74.6	9.5	10.04	105.7
9H	19	0625	74.6–84.1	9.5	9.87	104.0
10H	19	0735	84.1–93.6	9.5	9.83	103.0
11H	19	0835	93.6–102.0	8.4	8.41	100.0
Coring totals:				102.0	105.3	103.2
160-964C-						
1H	19	1030	0.0–5.1	5.1	5.15	101.0
2H	19	1135	5.1–14.6	9.5	9.84	103.0
3H	19	1245	14.6–24.1	9.5	9.82	103.0
4H	19	1345	24.1–33.6	9.5	9.95	105.0
5H	19	1445	33.6–43.1	9.5	9.55	100.0
6H	19	1555	43.1–52.6	9.5	10.04	105.7
7H	19	1700	52.6–62.1	9.5	9.76	103.0
8H	19	1805	62.1–71.6	9.5	9.69	102.0
9H	19	1920	71.6–81.1	9.5	10.07	106.0
10H	19	2030	81.1–90.6	9.5	10.04	105.7
11H	19	2145	90.6–95.6	5.0	5.09	102.0
12X	20	0010	95.6–105.1	9.5	7.48	78.7
Coring totals:				105.1	106.5	101.3
160-964D-						
1H	20	0200	0.0–4.1	4.1	4.11	100.0
2H	20	0255	4.1–13.6	9.5	9.71	102.0
3H	20	0345	13.6–23.1	9.5	9.79	103.0
4H	20	0440	23.1–32.6	9.5	9.92	104.0
5H	20	0535	32.6–42.1	9.5	9.57	101.0
6H	20	0630	42.1–51.6	9.5	9.84	103.0
7H	20	0730	51.6–61.1	9.5	9.74	102.0
8H	20	0830	61.1–70.6	9.5	10.08	106.1
9H	20	0830	70.6–80.1	9.5	9.28	97.7
10H	20	1025	80.1–89.6	9.5	9.94	104.0
11H	20	1125	89.6–99.1	9.5	10.08	106.1
12H	20	1450	99.1–108.6	9.5	10.14	106.7
Coring totals:				108.6	112.2	103.3
160-964E-						
1H	20	1700	0.0–5.5	5.5	5.54	101.0
2H	20	1755	5.5–15.0	9.5	9.88	104.0
3H	20	1900	15.0–24.5	9.5	9.79	103.0
4H	20	2100	57.0–66.5	9.5	10.01	105.3
5H	20	2210	66.5–76.0	9.5	9.10	95.8
6H	20	2315	76.0–85.5	9.5	10.00	105.2
Coring totals:				53.0	54.3	102.5
160-964F-						
1H	21	0100	0.0–9.1	9.1	9.17	101.0
2H	21	0200	9.1–18.6	9.5	9.95	105.0
3H	21	0300	18.6–28.1	9.5	8.82	92.8
Coring totals:				28.1	27.9	99.4

Hole 964B

The ship was offset 10 m to the east, where a seafloor depth of 3658.3 m was indicated by Core 160-964B-1H. APC Cores 160-964B-1H through 11H were taken from 0 to 102.0 mbsf (Table 1), with 102.0 m cored and 105.26 m recovered (103.2% recovery). Two liners imploded, and the last two cores were partial strokes.

Hole 964C

The ship was offset 10 m to the east, and Hole 964C was spudded at 1110 hr on 19 March. A seafloor depth of 3660.3 m was indicated by Core 160-964C-1H. APC Cores 160-964C-1H through 11H were taken from 0 to 95.6 mbsf (Table 1), with 95.6 m cored and 99.00 m recovered (103.6% recovery). Cores were oriented from Core 160-964C-3H. Core 160-964C-11H was a partial stroke with a collapsed liner and it had to be pumped out. XCB Core 160-964C-12X was taken from 95.6 to 105.1 mbsf and recovered 7.48 m (79% recovery) of foraminifer sand. The foraminifer sand was apparently the reason for the APC refusal.

Hole 964D

The ship was offset 10 m to the north, and Hole 964D was spudded at 0240 hr on 20 March. A seafloor depth of 3660.3 m was indicated by Core 160-964D-1H. APC Cores 160-964D-1H through 12H were taken from 0 to 108.6 mbsf, with 108.6 m cored and 112.2 m recovered (103.3% recovery). Cores were oriented from Core 160-964D-7H. A temperature measurement was taken after Core 160-964D-11H, but the temperature did not stabilize, possibly because the probe may have been in a foraminifer sand with some permeability and flow. Cores 160-964D-10H through 12H were partial strokes with 40–50-klb overpull. Core 160-964D-9H had an imploded liner on the bottom.

Hole 964E

The ship was offset 10 m to the west, and Hole 964E was spudded at 1735 hr on 20 March. A seafloor depth of 3660.9 m was indicated by Core 160-964E-1H. APC Cores 160-964E-1H through 3H were taken from 0 to 24.5 mbsf. The hole was washed from 24.5 to 57.0 mbsf. APC Cores 160-964E-4H through 6H were taken from 57.0 to 85.5 mbsf, with 53.0 m cored and 54.32 m recovered (102.5% recovery). However, the section recovered has core breaks at nearly the same depths as in the offset holes.

Hole 964F

The ship was offset 10 m west, and Hole 964F was spudded at 0140 hr on 21 March. A seafloor depth of 3657.3 m was indicated by Core 160-964F-1H. APC Cores 160-964F-1H through 3H were taken from 0 to 28.1 mbsf, with 28.1 m cored and 27.94 m recovered (99.4% recovery). The pipe was pulled out of the hole, the BHA was secured for sea voyage at 1224 hr on 21 March, and the beacon was retrieved to end Site 964.

SITE GEOPHYSICS

Several short seismic lines were run in order to assess the suitability of this site. Two possible sites were considered, one at the location determined with the Global Positioning System of a long piston core (KC01) that had obtained a good series of sapropels, and one at the less accurately determined cross point of two *Urania* seismic lines about 1 nmi to the northeast along a northeast-southwest-oriented ridge (Fig. 5). The ridge is seen on site-survey bathymetric charts to broaden in the vicinity of the crossed *Urania* lines, which made it a more attractive target, but the KC01 location was advantageous to consider because it was known to be a good site at least from a consideration of the upper sediments. One difficulty in surveying the site was the presence of considerable seafloor relief on the order of 100 m. Abrupt changes in depth over short distances cause so many diffractions that it is difficult to distinguish true seafloor reflections.

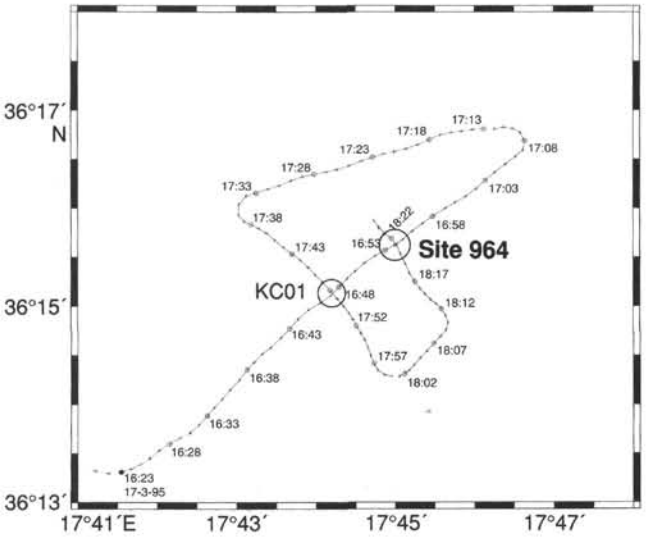

Figure 5. Location of the ship's track for the Leg 160 survey of Site 964.

The first line was run along the ridge and plateau from the southwest to the northeast through both the KC01 location and the cross lines originally picked as the proposed MEDSAP-3 site (Fig. 6). This line followed a *Urania* line, for comparison purposes. The second line was run at a right angle to the first, through the KC01 site from the northwest to the southeast, and a third was run through the MEDSAP-3 location from south to north. The topography and upper sedimentary unit down to a strong reflector at about 200 ms two-way traveltime (TWT) was known from the site survey by *Urania.*

Seismic basement in this area of low penetration is the strong reflector lying beneath an upper sedimentary unit that varies in thickness up to about 200 ms TWT in this area. The strong reflector deepens slightly to the northeast along the ridge from about 4.9 to about 5.0 s TWT, and the upper unit generally thickens slightly in the same direction. The ridge lies roughly perpendicular to the assumed direction of compression in this part of the Calabrian arc accretionary prism. The relief on the seismic basement is relatively flat in comparison with the seafloor relief, which at times drops almost to the level of the basement. Cross sections of the ridge showed that both potential sites were reasonably good targets; however, the original MEDSAP-3 site was chosen because it is located on a broader and slightly shallower part of the ridge.

LITHOSTRATIGRAPHY

The lithostratigraphic section recovered from six holes at the site consists of 112.2 m of sediment of early Pliocene to Holocene age. The composition is dominated by nannofossil clay, clayey nannofossil ooze, and nannofossil ooze with limited intervals of foraminifer-bearing nannofossil ooze, foraminifer sand, and clay. On average, the clay component decreases downsection. The sequence consists of numerous light-colored intervals (decimeter to meter thick) of nannofossil clay, nannofossil ooze, and clayey nannofossil ooze; some are massive, some grade normally, and some are slightly to moderately bioturbated. Faint color banding and mottling are common throughout many of these intervals. Below 83 mbsf, the thickness of the graded beds increases from decimeters to meters. These beds have been interpreted as fine-grained turbidites. Volcanic glass is disseminated throughout the section.

The dominant light-colored intervals alternate with beds (55 in total) of dark-colored nannofossil clay and clay. All these beds contain disseminated organic matter and pyrite with variable amounts of volcanic glass, quartz, inorganic calcite, and plant fragments. The dark-colored beds are enriched in organic carbon.

Numerous thin reworked glass-rich silt layers occur sporadically throughout the section. These are on average 2–3 cm thick and range between <0.5 and 6 cm. The thicker layers typically exhibit poorly developed normal grading.

The extent and sedimentary composition of the sapropels varies. Individual sapropels are 1–25 cm thick. Some are massive, whereas some exhibit lamination at a millimeter to submillimeter scale. Many of the sapropels are characterized by sharp color boundaries, but some have gradational color contacts. Traces of burrows occur across some boundaries and within some dark-colored intervals. Foraminifers are disseminated throughout the intervals or concentrated in thin (centimeter thick) bands close to depositional boundaries. The organ-

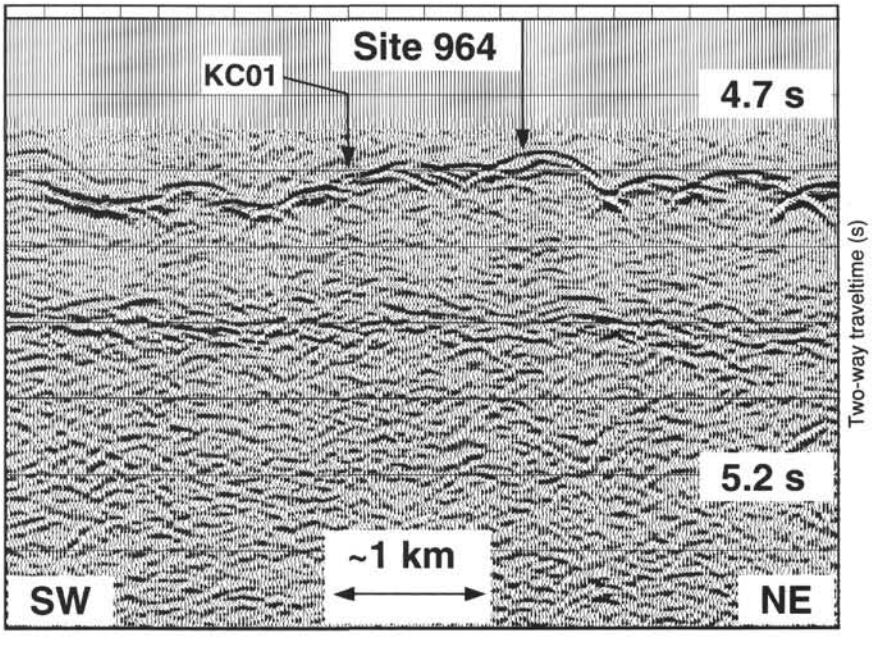

Figure 6. Seismic profile for Site 964.

ic carbon content of the sapropels varies between approximately 2% and 25% (see "Organic Geochemistry" section, this chapter). Authigenic minerals are present as minor components throughout the sequence, with pyrite ubiquitous in all the sapropels.

Criteria employed in lithostratigraphic description and classification at Site 964 included (1) visual observation of color; (2) visual observation of sedimentary structures, including bioturbation; (3) smear-slide examination; (4) reflectance spectrophotometry measurements; (5) magnetic susceptibility and intensity measurements; (6) carbonate determinations; and (7) X-ray diffraction (XRD) analysis.

Because the dominant lithology of the sequence exhibits little downcore lithologic variation, the sediments were classified as a single lithostratigraphic unit. Within this unit, sapropel and ash are present as minor lithologies. The sedimentological composition and frequency of occurrence of sapropels within the section is presented within the unit description. A lithostratigraphic summary of Site 964 is presented in Figure 7.

Interhole Correlation and Development of a Composite Section

In order to provide a stratigraphic correlation among the holes at Site 964, distinctive lithologic markers were identified in all holes drilled. The sedimentological characteristics and position of each sapropel were recorded, as were the position and composition of the more distinctive turbidites and ash layers. A check on the visual correlation was provided by color-scanner data (see "Color Reflectance," this section), and reference was also made to selected MST data.

Discrepancies in the number of sapropels recovered in the various holes can be attributed to (1) the presence of gaps in coring between successive cores (see "Composite Depths" section, this chapter) and (2) attenuation of the sequence by extensional soft-sediment faulting (see "Structural Geology" section, this chapter, and as discussed below). In comparing the sequences obtained from different holes, localized significant high-angle extensional faulting (e.g., Fig. 25, "Structural Geology" section, this chapter) was found to be associated with absence of sapropels relative to more complete sequences in adjacent holes. Some sapropels appear to have been faulted out of the section and, in some instances, the sheared remnants of sapropels were observed along fault planes (see Fig. 24, "Structural Geology" section, this chapter). A complete list of all sapropels recovered at Site 964 is shown in Table 2, and the stratigraphic correlation is presented in Figure 8. From the six holes drilled, a composite section was constructed using the most intact sequences in which no obvious faulting could be recognized (see Table 7 ["Composite Depth" section, this chapter], Figs. 8, 9). This lithologically based composite section differs in some key intervals from the preliminary composite section prepared from color data using the "splicer" program without reference to the cores (see "Composite Depths" section, this chapter) as the latter did not take into account the possibility that parts of the sequence might be absent owing to extensional faulting.

A revised spliced composite section was prepared using the color reflectance data based on the pathway shown in Figure 8 and Table 7. As the original composite section included some cores with tectonically removed sections (e.g., as much as 5 m in Core 160-964A-6H), the revised splice is somewhat longer. Future shore-based sampling to produce a high-resolution time-series will be based on the lithologic stratigraphic correlation.

Color Reflectance

The cores from Holes 964A, 964B, 964D, and 964E; three cores from Hole 964C (160-964C-9H through 11H); and one core from Hole 964F (160-964F-2H) were scanned at 2-cm resolution to ensure complete representation of the stratigraphic section.

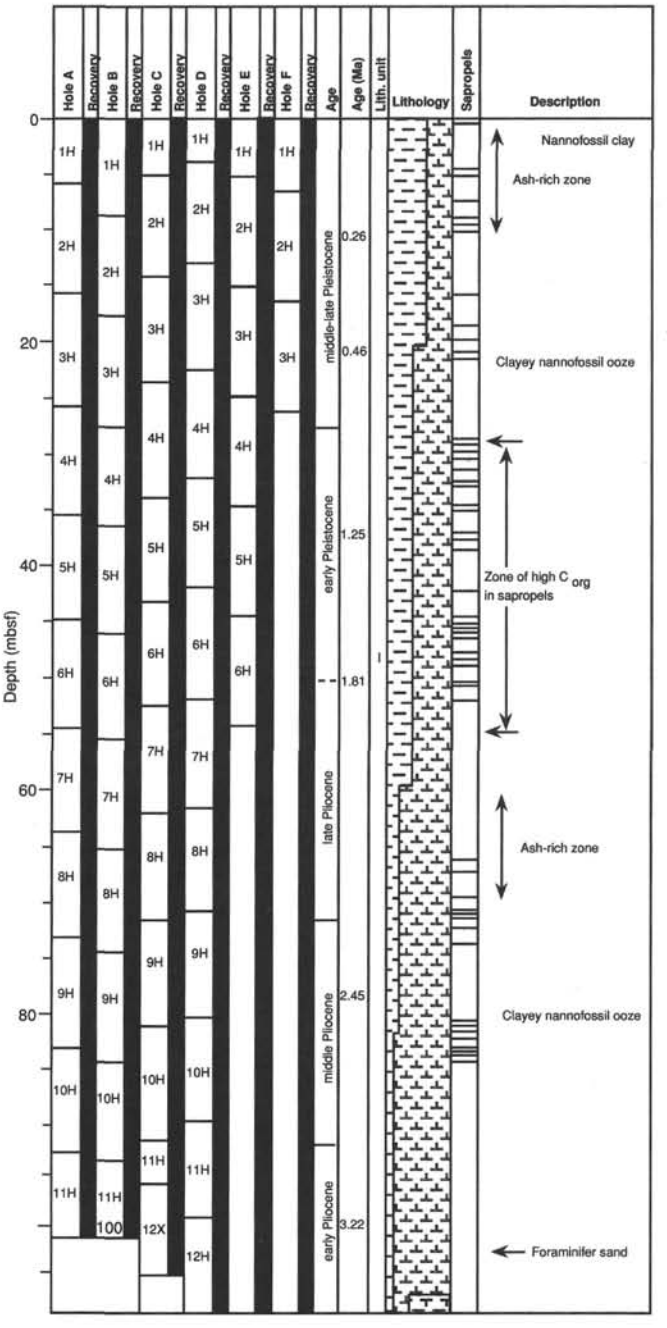

Figure 7. Core recovery, lithostratigraphic summary, and age information for Site 964.

Although there was considerable variation in color within the dominant sediment type owing mostly to diagenetic features such as oxidation fronts, the dominant lithology generally appeared as a light-colored background against which the other features stood out. Sapropels, ash layers, and massive turbidites provided the most useful tie points for color correlation between holes, although by correlating these features it appeared that more subtle lithologic changes and even some of the diagenetic fronts could be identified between holes.

The sapropels have sharp dark peaks, which are represented as minima of reflectance values at 550 nm; these peaks are usually well bounded on both sides by lighter sediments with a less extreme reflectance signature (Fig. 10). At 2-cm spacing it was possible to re-

Table 2. Position of sapropels recovered at Site 964.

Core, section, interval (cm)	Depth (mbsf)	Thickness (cm)	Number	Core, section, interval (cm)	Depth (mbsf)	Thickness (cm)	Number	Core, section, interval (cm)	Depth (mbsf)	Thickness (cm)	Number
160-964A-				160-964B-				160-964C-			
1H-1, 72–84	0.72	12	1	1H-1, 66–72	0.66	6	1	1H-1, 59–61	0.59	2	1
				1H-5, 13–38	6.13	25	2	1H-4, 19–25	4.69	6	2
2H-1, 90–105	7.7	15	3	1H-5, 118–138	7.18	19.5	3	2H-1, 24–31	5.34	2	3
2H-3, 80–138	10.6	58	4	2H-2, 11–77	9.71	66	4	2H-3, 88–96	8.98	8	4
2H-4, 67–76	11.97	9	5	2H-2, 142, to 2H-3, 5	11.02	13	5				
2H-4, 131–150	12.61	19	6								
2H-5, 57–59	13.37	2	7	2H-3, 44–46	11.54	2	7				
3H-2, 104–108	18.84	4	8	2H-7, 12–22	17.22	10	8	3H-1, 42–43	15.02	1	8
3H-4, 103–107	21.83	4	9	3H-3, 5–10	20.65	5	9	3H-2, 145, to 3H-3, 2	17.55	7	9
3H-5, 86–96	23.16	10	10	3H-3, 133–142	21.93	9	10	3H-3, 119–128	17.6	9	10
3H-6, 69–71	24.49	2	11	3H-4, 117.50–120	22.53	2.5	11	3H-4, 94–98	18.79	4	11
3H-6, 111–116	24.91	5	12	3H-5, 14–19	23.74	5	12	3H-4, 133.5–142	20.04	8.5	12
4H-3, 98–99	29.78	1	13					4H-1, 49–56	24.59	7	13
4H-1, 148–2	30.3	3	14					4H-1, 100–103	24.64	3	14
4H-4, 37.5–39.5	30.68	2	15					4H-1, 142–144	25.1	2	15
4H-4, 101.5–107.5	31.32	6	16					4H-2, 62–67	25.52	5	16
4H-5, 50–60	32.35	10	17	4H-3, 26–37	30.36	11	17	4H-3, 6–11	26.22	5	17
4H-5, 148–150	33.28	6	18	4H-3, 118–122	31.28	4	18	4H-3, 93–98	27.16	5	18
4H-7, 14–17	34.94	3	19	4H-4, 126–129	32.86	3	19	4H-4, 99–101	28.03	2	19
5H-1, 113–122	36.43	9	20	4H-6, 58–61	35.18	3	20	4H-6, 33–36	29.59	3	20
5H-3, 29–35	38.59	6	21								
5H-4, 101–103	40.81	2	22	5H-2, 52–56	38.62	4	22	5H-2, 45.5–47.5	31.93	2	22
5H-5, 44–55	41.74	11	23	5H-2, 142, to 5H-3, 15	39.52	23	23	5H-2, 133–142	35.555	9	23
5H-5, 98.5–103	42.29	4.5	24	5H-3, 49–54	40.09	4.5	24	5H-3, 31–36	36.43	5	24
				5H-5, 84–90	43.44	6	25	5H-5, 46–52	36.91	8	25
6H-1, 83–88	45.63	5	26	5H-6, 35–39	44.45	4	26	5H-5, 141–146	40.06	5	26
6H-3, 41–47	48.21	6	27					6H-1, 103–107	41.01	5	27
				6H-2, 28–35	47.88	7	29	6H-2, 1–8	44.13	7	29
6H-4, 31–39	49.61	8	30	6H-2, 84–98	48.44	14	30	6H-2, 51–58.5	44.61	7.5	30
				6H-2, 145–150	49.05	5	31				
6H-5, 14–18.3	50.94	4.3	32	6H-3, 126–134	50.36	8	32	6H-3, 28–34.5	45.165	6.5	32
				6H-4, 29–41	50.89	12	33	6H-3, 71.5–72.5	46.38	1	33
								6H-3, 107–113	46.815	6	34
6H-6, 83–85	53.13	2	35	6H-5, 36–39	52.46	3	35	6H-4, 85.5–87.5	47.17	2	35
6H-6, 93–95.5	53.23	2.5	36					6H-4, 95.5–99	48.455	3.5	36
6H-7, 17–22	53.97	5	37	6H-5, 116–121	53.26	5	37	6H-5, 21–24.5	48.575	3.5	37
								7H-2, 37–40	49.31	3	38
7H-4, 107–113	59.87	6	39					7H-3, 9–13	54.47	4	39
				7H-4, 115–120	61.25	5	40	7H-4, 85–90	55.69	5	40
				7H-5, 86–90	62.46	4	41	7H-5, 52–58	57.95	6	41
8H-1, 65.5–73	64.46	7.5	42	7H-6, 44–64	63.54	20	42	7H-6, 17–37	59.12	20	42
8H-1, 85–95	64.58	10	44	7H-6, 85–86	63.72	1	44	7H-6, 51–60	59.46	9	44
				8H-7, 36–38	74.46	2	45	9H-1, 136–137.5	60.43	1.5	45
				8H-CC, 29.50–31	75.01	1.5	46	9H-2, 53–57	72.96	4	46
								9H-2, 75–79	73.63	4	47
8H-6, 21–26	71.51	5	48	9H-2, 6.50–13	76.17	6.5	48	9H-3, 86–93	73.85	7	48
				9H-6, 7–10	82.18	3	49	9H-6, 70–70.5	75.46	0.5	49
9H-3, 40–42	76.45	2	50	9H-6, 100–103	83.1	3	50	9H-CC, 7–10	79.8	3	50
9H-4, 31–37	78.11	6	51								
9H-5, 89–95	80.19	6	54					10H-1, 2–6	80.67	4	54
9H-6, 12–20	80.92	8	55					10H-1, 76–82	81.12	6	55
9H-6, 85–92	81.17	7	56					10H-1, 140–145	81.86	5	56
9H-7, 4–6	82.34	2	57					10H-2, 56–58	82.5	2	57
9H-CC, 6–14	82.92	8	58					10H-2, 112–120	83.16	8	58
10H-1, 140–3	83.54	13	60	10H-3, 65–74	88.72	9	60	10H-3, 72–86	84.18	14	60

solve many of the multiple-banded dark-colored sapropels; this was especially useful for correlation purposes. The thick fine-grained turbidite intervals toward the bottom of the sequence provided a distinctive monochromatic signal that was well defined in each hole and thus aided correlation. In addition, many of the silt layers and ash layers provided second-order tie points.

Description of Lithostratigraphic Unit

Lithostratigraphic Unit I

Description: Nannofossil clay, clayey nannofossil ooze, and nannofossil ooze

Intervals: Cores 160-964A-1H through 11H, 160-964B-1H through 11H, 160-964C-1H through 12X, 160-964D-1H through 12H, 160-964E-1H through 6H, and 160-964F-1H through 3H

Depth: 0–101.8 mbsf, Hole 964A; 0–102.0 mbsf, Hole 964B; 0–105.1 mbsf, Hole 964C; 0–108.6 mbsf, Hole 964D; 0–53.0 mbsf, Hole 964E; 0–28.1 mbsf, Hole 964F

Age: early Pliocene to Holocene

The lithology of Unit I is dominated by alternations of light grayish-brown (10YR 5/2), light gray (10Y 6/1), gray (10Y 4/1), and greenish-gray (5GY 5/1) nannofossil clay, clayey nannofossil ooze, and nannofossil ooze. Smear-slide analyses reveal that the sediment is composed of between 30% and 80% nannofossils and between 5% and 60% clay. The clay component, on average, decreases downhole. The results of smear-slide analyses (of selected components of the dominant and minor lithologies) are presented in Figure 11A, B. Results of quantitative determination of carbonate (see "Organic Geochemistry" section, this chapter) indicate fluctuation throughout the unit, ranging from a minimum of 40% to a maximum of 80%. Organic carbon levels in the light-colored interval are low (0.1%–0.5%, see "Organic Geochemistry" section, this chapter). Minor components include quartz, volcanic glass, inorganic calcite, and authigenic minerals, in particular pyrite. Limited intervals in the section consist of gray (10Y 4/1) foraminifer sand, especially below 100 mbsf. Many of the light-colored intervals grade normally on a decimeter to meter scale. The thickest turbidites (>10 m, cf., Core 160-964D-12H) occur

Table 2 (continued).

Core, section, interval (cm)	Depth (mbsf)	Thickness (cm)	Number	Core, section, interval (cm)	Depth (mbsf)	Thickness (cm)	Number	Core, section, interval (cm)	Depth (mbsf)	Thickness (cm)	Number
160-964D-				160-964E-				160-964F-			
1H-1, 62–85	0.62	13	1								
2H-1, 48–57	4.5	9	2					1H-5, 38–47	6.38	9	2
2H-3, 28–31	7.38	3	3					1H-5, 114–126	7.14	12	3
2H-3, 62–86	7.7	23	4					2H-1, 13–14	9.23	1	4
2H-4, 17–28	8.75	11	5	2H-1, 60–63	6.1	3	5	2H-1, 137–142	10.47	7	5
2H-4, 83–104	9.3	21	6	2H-1, 106–123	6.56	17	6	2H-2, 34–42	10.94	9	?
2H-5, 15–20	10.2	5	7	2H-2, 17–25	7.17	8	7	2H-4, 102–110	14.62	8	?
3H-2, 83–86	15.8	3	8					2H-6, 134–138	17.94	4	7
				2H-CC, 16–23	15.3	7	?				
3H-4, 47–51	18.5	4	9	3H-2, 97–102	17.21	5	9	3H-1, 79–84	19.39	5	9
3H-5, 25–35	19.8	10	10	3H-3, 70–80	18.7	10	10	3H-2, 53–63	20.63	10	10
3H-5, 122–129	20.82	7	11	3H-4, 50–52	20	2	11	3H-3, 36–38	21.96	2	11
3H-6, 21–25	21.25	4	12	3H-4, 90–95	20.4	5	12	3H-3, 76–79	22.36	3	12
4H-4, 114–126	28.74	12	13								
4H-5, 20–25	29.3	5	14								
4H-5, 65–68	29.75	3	15								
4H-5, 140–147	30.5	7	16								
4H-6, 85–97	31.45	12	17								
4H-7, 32–38	32.42	6	18								
5H-1, 20–22	32.8	2	19								
5H-2, 82–90	34.92	8	20								
5H-2, 104–106	35.14	2	21								
5H-3, 141–143	37.01	2	22								
5H-4, 53–67	37.63	14	23								
5H-4, 137–142	38.47	5	24								
5H-7, 18–24	41.78	6	25								
6H-2, 68–75	44.28	7	27								
6H-3, 55.50–58.30	45.655	3	28								
6H-3, 113–118	46.23	5	29								
6H-4, 12–22	46.72	10	30								
6H-4, 68–69	47.23	1	31								
6H-5, 56–61.50	48.66	5.5	32								
6H-5, 121–123.50	49.31	2.5	33								
6H-6, 39–42	49.99	3	34								
6H-6, 112–114	50.72	2	35								
6H-6, 120–124	50.8	4	36								
6H-7, 48.50–52.80	51.585	4	37								
7H-4, 48–51	66.08	3	38								
7H-5, 28–32	67.38	4	39								
7H-6, 97–102	69.57	5	41	4H-2, 36–42	58.86	6	41				
7H-7, 51–52	70.61	1	42	4H-2, 138, to 4H-3, 10	59.88	22	42				
7H-CC, 0–8.00	70.88	8	43	4H-3, 68–72	60.68	4	43				
				4H-4, 135–137	62.85	2	44				
9H-1, 75–77	71.35	2	46	5H-3, 75–80	70.25	5	?				
9H-1, 147–149	72.07	2	47								
9H-2, 149, to 9H-3, 6	73.59	7	48	5H-5, 92–98	73.42	6	48				
				6H-2, 31–33	77.81	2	50				
				6H-2, 131–143	78.81	12	51				
10H-1, 59–61	80.69	2	52	6H-3, 105–110	80.05	5	52				
10H-1, 103–110	81.13	7	53	6H-4, 1–10	80.51	9	53				
10H-2, 0–6.50	81.6	6.5	54	6H-4, 52–53	81.02	1	54				
10H-2, 62–67.50	82.22	5.5	55	6H-4, 114–122	81.64	8	55				
10H-2, 117–122	82.77	5	56	6H-5, 25–32	82.25	7	56				
10H-3, 15.50–18	83.255	2.5	57	6H-5, 87–103	82.88	16	57				
10H-3, 62.50–70.50	83.725	8	58	6H-6, 5–12	84.08	7	58				
10H-3, 111–113	84.21	2	59	6H-6, 59–61	84.67	2	59				
				6H-6, 85–92	85.52	7	60				

toward the base of the recovered section, below approximately 85 mbsf. The basal contacts of many of the turbidite intervals are highlighted by medium- to fine-grained dark greenish gray (5GY 5/1) silts consisting of quartz, mica, inorganic calcite, and foraminifers.

One of the features most noticeable in some of the light-colored intervals is the common occurrence of dark gray, ?iron-sulfide-rich intervals, including staining in thin horizontal bands and/or sparsely disseminated pyrite. In general, these intervals are adjacent to intervals that are yellow-brown in color. The color banding is probably of diagenetic origin and related to pore-water ionic diffusion gradients and redox boundaries.

Sapropels

The dominant background lithology alternates with 55 discrete centimeter- to decimeter-thick dark olive gray (5Y 3/2), very dark gray (5Y 3/1), and black (5Y 2.5/1, 2.5/2) beds of nannofossil clay and clay (Table 2). All of these intervals are enriched in pyrite and variable amounts of amorphous organic matter; some contain admixtures of foraminifers (mainly planktonic but including some benthic species), volcanic glass, quartz, and fragments of higher plant material (e.g., seed plant cuticles are well preserved in some sapropels). All of the dark-colored intervals are carbonate poor (0%–20%) and organic carbon rich (2%–25%) (see "Organic Geochemistry" section, this chapter). Clusters of dark-colored intervals with higher organic carbon values occur between 0 and 20 mbsf, 25 and 55 mbsf (highest C_{org} values), and 65 and 80 mbsf (see "Organic Geochemistry" section, this chapter).

The sapropels at Site 964 are 1–25 cm thick and display a range of textural and color variation. Distinctive color zonation (gray and gray-blue) exists close to both the upper and basal contacts of most sapropels. This pattern can be identified in most sapropels even when the organic matter has been oxidized.

A classification of the sapropels recovered at Site 964, based upon extent, color, and structure, is presented below (see also Tables 2, 3).

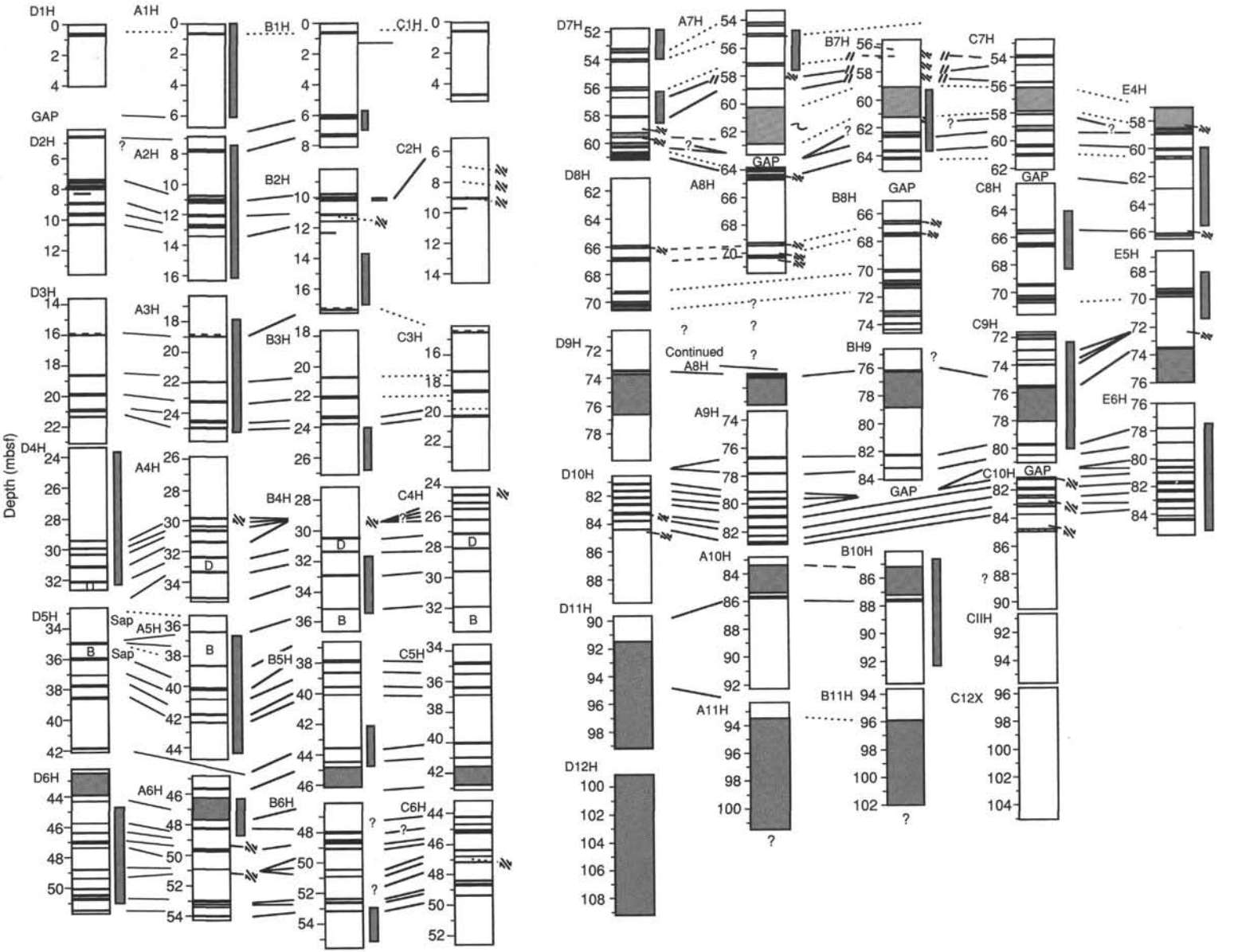

Figure 8. Correlation among Holes 964A, 964B, 964C, 964D, and 964E. The shaded bar on the right-hand side of the schematic indicates the intervals of each hole used to compile the composite lithologic spliced section.

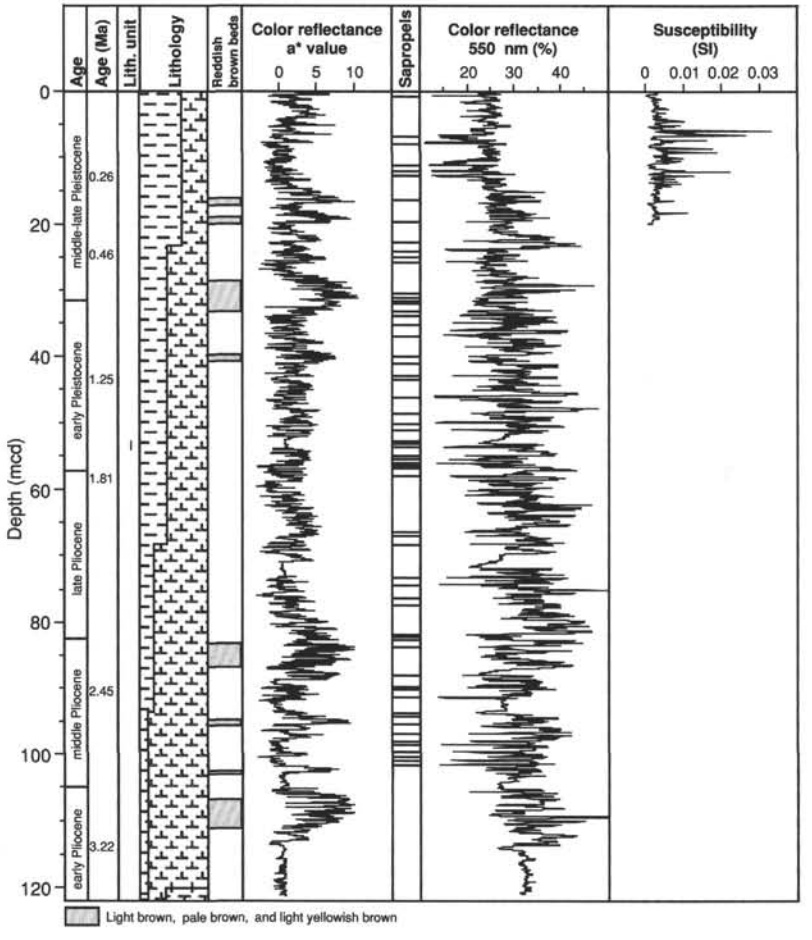

Figure 9. Spliced composite section of Site 964 as given in Table 7 (see text for discussion). Columns indicate, from left to right: age; lithologic summary; location of "reddish brown beds" indicating intervals where the sediment ranges from light brown (10YR 6/3) to reddish brown (5YR 5/4); color reflectance a* value (values greater than zero indicate a red chroma); location of sapropels; color reflectance at 550 nm; and magnetic susceptibility.

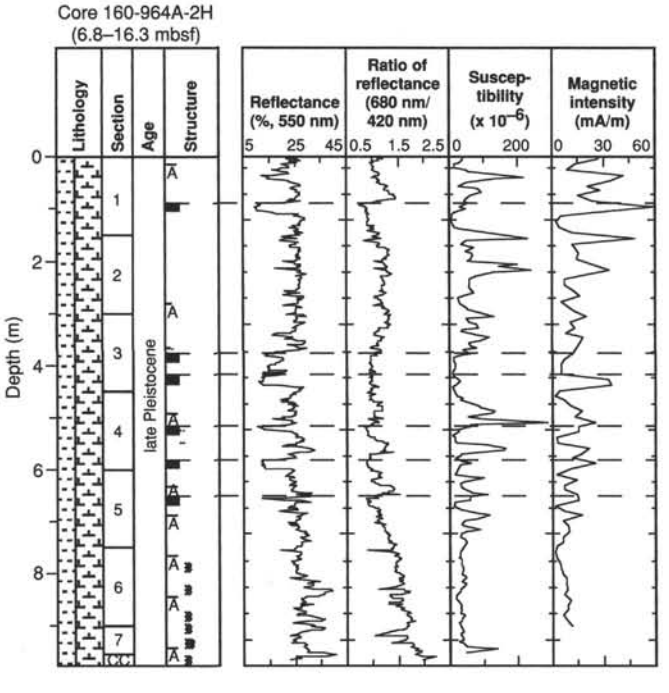

Figure 10. Example of correlation between lithology, color reflectance, and selected MST data. "A" denotes an ash layer.

Thin-bedded Sapropels

These beds are between 1 and 5 cm thick and are the most common in occurrence (50% of total). Beds range in color from dark olive gray (5Y 3/2) to very dark gray (5Y 3/1) and black (5Y 2.5/1, 2.5/2). Thin-bedded sapropels can have sharp upper and lower color contacts and contain no visible lamination or they are faintly laminated at the millimeter to micron scale; some of the lamination is disrupted by bioturbation. Several of the thin-bedded sapropels in the interval between 30 and 55 mbsf and below 80 mbsf are black (5Y 2.5/1, 2.5/2) throughout and contain very high levels of organic carbon (cf., Fig. 12A). Many beds display gradational color boundaries (Fig. 12B); some have a gradational base and/or upper boundary. Many of these beds display a darkening-upward trend from dark olive gray (5Y 3/2), through very dark gray (5Y 3/1), to black (5Y 2.5/1, 2.5/2). Some beds have foraminifers disseminated throughout, whereas others have discrete concentrations of foraminifers (0.5–1 cm thick) near the upper and/or basal contacts.

Thick-bedded Sapropels

These beds are greater than 5 cm thick and are dark olive gray (5Y 3/2) to very dark gray (5Y 3/1) or black (5Y 2.5/1). In some cases, the basal 1–2 cm of the sapropel is olive gray (5Y 3/2) and the upper part is black (5Y 2.5/1). Color boundaries vary; most are sharp although some are gradational (cf., lower gradational boundary in Fig. 13A). Most of these sapropels contain millimeter- to micron-scale lamination (Fig. 13A). This may be continuous or intermittent (alternating with massive layers) and some is irregular (probably as a result of

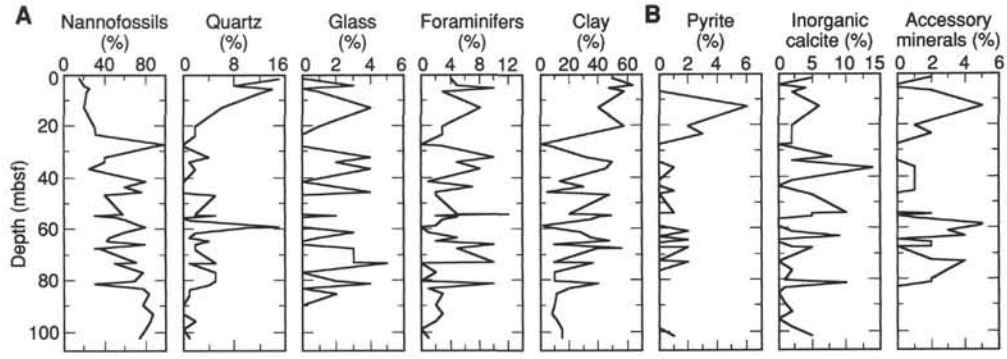

Figure 11. Smear slide data for (**A**) selected dominant sedimentary components and (**B**) minor sedimentary components at Site 964.

Table 3. Sapropel beds within lithologic composite section at Site 964.

Hole, core, section, interval (cm)	Depth (mbsf)	Thickness (cm)	Number	Classification[a]
964A-1H-1, 72.0–84.0	0.84	12	1	2
964B-1H-5, 13.0–38.0	6.38	25	2	3(2)
964B-1H-5, 118.0–138.0	7.38	19.5	3	2
964A-2H-3, 80.0–138.0	11.18	58	4	3(4)
964A-2H-4, 67.0–76.0	12.06	9	5	2
964A-2H-4, 131.0–150.0	12.8	19	6	2
964A-2H-5, 57.0–59.0	13.39	2	7	4
964A-3H-2, 104.0–108.0	18.88	4	8	4
964A-3H-4, 103.0–107.0	21.87	4	9	1
964A-3H-5, 86.0–96.0	23.26	10	10	3(2)
964A-3H-6, 69.0–71.0	24.51	2	1	1(4)
964A-3H-6, 111.0–116.0	24.96	5	12	1
964D-4H-4, 114.0–126.0	28.86	12	13	3(2)
964D-4H-5, 20.0–25.0	29.35	5	14	3(2)
964D-4H-5, 65.0–68.0	29.78	3	15	1
964D-4H-5, 140.0–147.0	30.57	7	16	2
964D-4H-6, 85.0–97.0	31.57	12	17	3(2)
964B-4H-3, 118.0–122.0	31.32	4	18	1
964B-4H-4, 126.0–129.0	32.89	3	19	1
964B-4H-6, 58.0–61.0	35.21	3	20	1
964A-5H-3, 29.0–35.0	38.65	6	21	2
964A-5H-4, 101.0–103.0	40.83	2	22	1
964A-5H-5, 44.0–55.0	41.85	11	23	2
964A-5H-5, 98.5–103.0	42.33	4.5	24	1
964B-5H-5, 84.0–90.0	43.5	6	25	2
964B-5H-6, 35.0–39.0	44.49	4	26	1
964D-6H-2, 68.0–75.0	44.35	7	27	2
964D-6H-3, 55.5–58.3	45.68	3	28	1(4)
964D-6H-3, 113.0–118.0	46.28	5	29	1
964D-6H-4, 12.0–22.0	46.82	10	30	3(2)
964D-6H-4, 68.0–69.0	47.29	1	31	1
964D-6H-5, 56.0–61.5	48.72	5.5	32	2
964D-6H-5, 121.0–123.5	49.34	2.5	33	4
964D-6H-6, 39.0–42.0	50.02	3	34	3(3)
964D-6H-6, 112.0–114.0	50.74	2	35	1
964D-6H-6, 120.0–124.0	50.84	4	36	3(2)
964B-6H-5, 116.0–121.0	53.31	5	37	1
964D-7H-4, 48.0–51.0	56.61	3	38	1
964D-7H-5, 28.0–32.0	57.92	4	39	1
964B-7H-4, 115.0–120.0	61.3	5	40	1
964B-7H-5, 86.0–90.0	62.5	4	41	1
964E-4H-2, 138.0, to 4H-3, 10.0	60.1	22	42	3(2)
964E-4H-3, 68.0–72.0	60.72	4	43	4
964E-4H-4, 135.0–137.0	62.87	2	44	4
964C-9H-1, 136.0–137.5	72.98	1.5	45	1
964C-9H-2, 53.0–57.0	73.67	4	46	1
964C-9H-2, 75.0–79.0	73.89	4	47	3(2)
964C-9H-3, 86.0–93.0	75.53	7	48	2
964C-9H-6, 77.0–79.0	79.89	2	49	1
964E-6H-2, 31.0–35.0	77.85	4	50	1
964E-6H-2, 131.0–135.0	78.85	4	51	1
964E-6H-3, 105.0–108.0	80.08	3	52	1
964E-6H-4, 1.0–10.0	80.6	9	53	2
964E-6H-4, 52.0–53.0	81.03	1	54	1
964E-6H-4, 114.0–122.0	81.72	8	55	3(2)
964E-6H-5, 25.0–32.0	82.32	7	56	4
964E-6H-5, 87.0–103.0	83.03	16	57	3(2)
964E-6H-6, 5.0–12.0	83.62	7	58	2
964E-6H-6, 59.0–61.0	84.11	2	59	1
964E-6H-6, 85.0–94.0	84.44	9	60	4

[a]1= thin-bedded sapropel; 2 = thick-bedded sapropel; 3 = composite sapropel (figure in parentheses indicates number of dark-colored beds within composite); 4 = oxidized sapropel.

bioturbation). Most of these beds contain foraminifers disseminated throughout. A few are structureless (Fig. 13B).

Composite Sapropels

These beds are characterized by two, or sporadically more, distinct dark-colored beds greater than 1 cm thick, alternating with light-colored sediments. Composite sapropels at Site 964 are between 7 and 25 cm thick and usually have sharp upper and basal color boundaries. Some composite sapropels contain foraminifers disseminated throughout, whereas in others they were found only in the lower dark-colored interval (Fig. 14A). In some instances the light-colored sediment separating the dark beds is bioturbated (Fig. 14B). In other respects, the composite sapropels display many of the characteristics of the thin- and thick-bedded sapropels listed above.

Oxidized Sapropels

These beds display gradational horizontal yellow-brown-orange color banding (5YR–10YR). Several are easily recognized as they contain the distinctive laminated to irregularly laminated fabrics characteristic of dark-colored sapropels. A complete record of oxidized sapropels was not obtained from Site 964, as not all were immediately obvious during core description. Consequently, Table 2 lists only the more prominent of these layers. It appears that most organic matter within the oxidized sapropels has been removed; however, in some instances, it appears that only partial removal has occurred (Fig. 15). Variable oxidation of the sapropels between holes was also observed. In one instance (sapropel 11 of Table 2), the sapropel was observed to be oxidized in all the holes except in Section 160-964C-3H-3, 36–38 cm, where the corresponding bed is composed of a 2-cm-thick dark-colored layer.

Background and Depositional History

Site 964 builds upon the lithologic findings of previous drilling in the area (DSDP Leg 42A, Site 374 on the Messina Abyssal Plain—Hsü, Montadert, et al., 1978). The sequence recovered at Site 964 provides the continuous marine sediment core section containing upper Pliocene to upper Pleistocene (Holocene) sapropels. This sequence bridges the gap between existing marine sediment cores (McCoy, 1974; Rohling, 1994) and the on-land outcrop (Hilgen, 1991a).

The sediments recovered at Site 964 indicate that the depositional processes and oceanographic conditions in the region have fluctuated significantly since the early Pliocene.

Light-colored, organic-carbon-poor sediments, in particular, the intervals of nannofossil clay, clayey nannofossil ooze, and nannofossil ooze, are indicative of sedimentation within an oxygenated environment. The presence of sapropels, in the main deposited during the

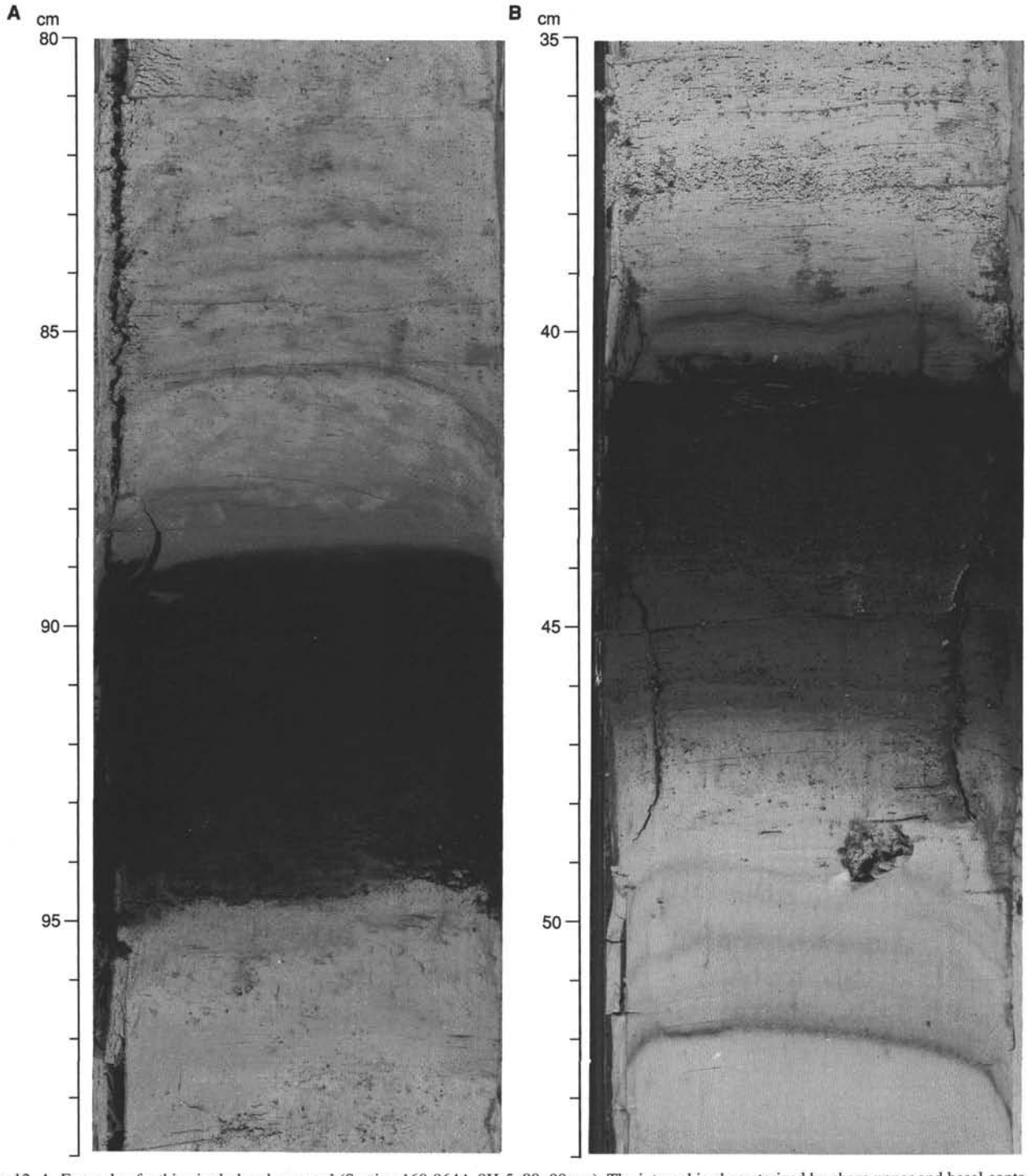

Figure 12. **A.** Example of a thin single-band sapropel (Section 160-964A-9H-5, 80–99 cm). The interval is characterized by sharp upper and basal contacts and black color throughout. Note the faint horizontal color-banding (?diagenetic) and infilled burrows in the interval at 83–88.5 cm, a feature common in many similar sapropels. **B.** Example of a thin single-band sapropel (Section 160-964A-6H-3, 35–54 cm). Note the gradational darkening in color in the interval at 46–41 cm. Boundaries in this case are color gradational. Foraminifers are disseminated throughout.

middle Pliocene, late Pliocene–early Pleistocene (organic carbon values of some of these recovered sapropels are up to 25%, see "Organic Geochemistry" section, this chapter), and middle late Pleistocene (see Fig. 7), infers either a significant change in the flux of organic matter into this area and/or enhanced preservation of organic matter.

The composition of the sapropels recovered at Site 964 points to a variety of depositional and postdepositional processes. Primary lamination within some beds is indicative of anoxic conditions. The presence of benthic foraminifers would infer oxygen at or near the sediment/water interface during deposition of some of these beds. Both abrupt and gradational color contacts probably reflect changes in the depositional environment, and/or postdepositional alteration. Amorphous organic matter is ubiquitous in many beds; some contain fragments of terrestrial plant material—this may reflect initial input, preferential sorting/burial, or postdepositional alteration.

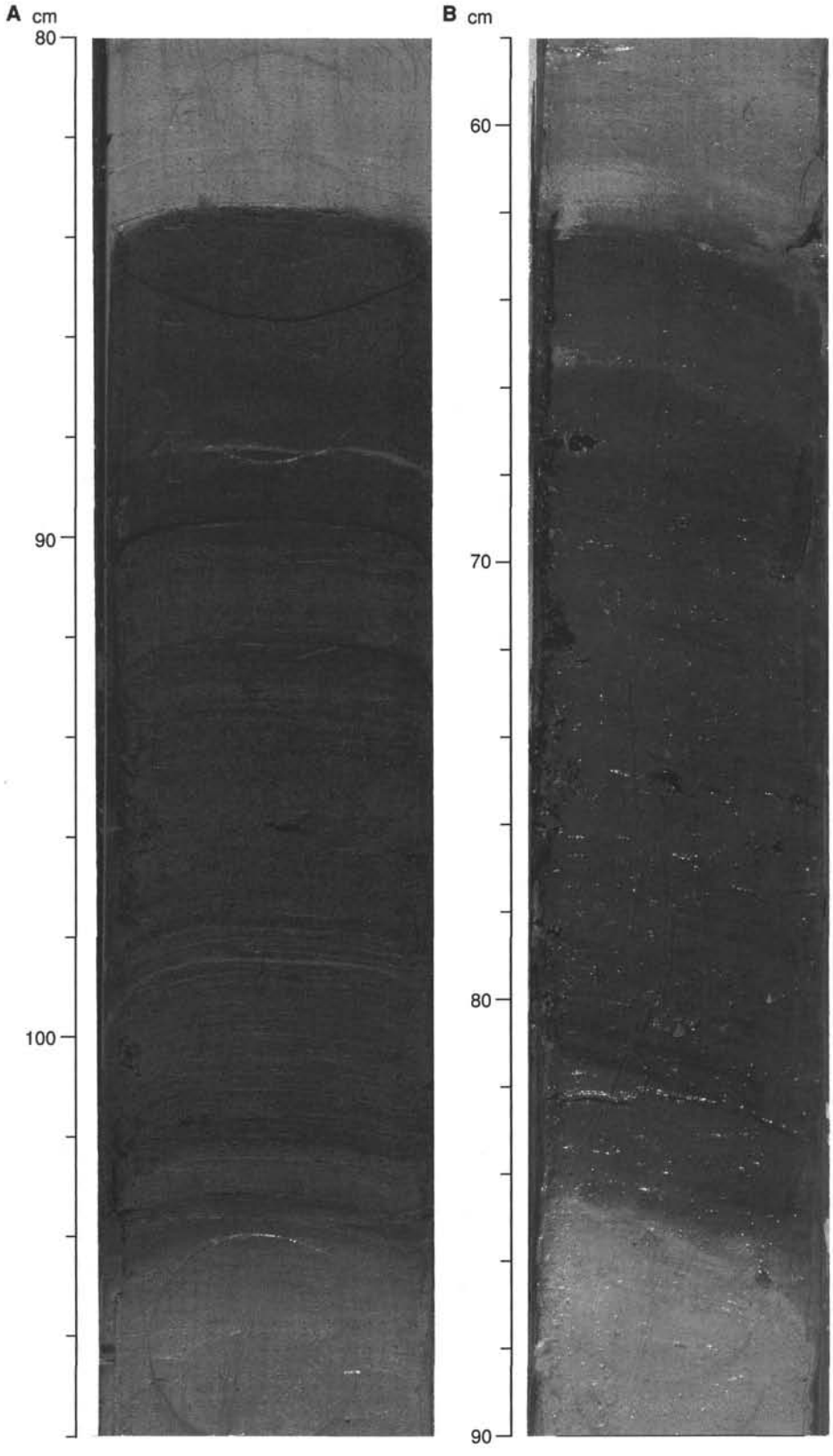

Figure 13. **A.** Example of a thick single-band sapropel (Section 160-964D-2H-4, 80–108 cm). Note the gradational basal and sharp upper boundaries, slight darkening in color toward the top, and millimeter- to micron-scale laminae, especially evident in the interval between 88 and 104 cm. **B.** Example of a thick single-band sapropel (Section 160-964D-1H-1, 58–90 cm). This sapropel does not display structural lamination, although faint color banding is evident. Pteropod fragments are visible scattered throughout the sapropel. This is an example of the most recently deposited Holocene sapropel (S1 at 7–9 ka, according to the nomenclature of McCoy, 1974), which is found throughout the Eastern Mediterranean.

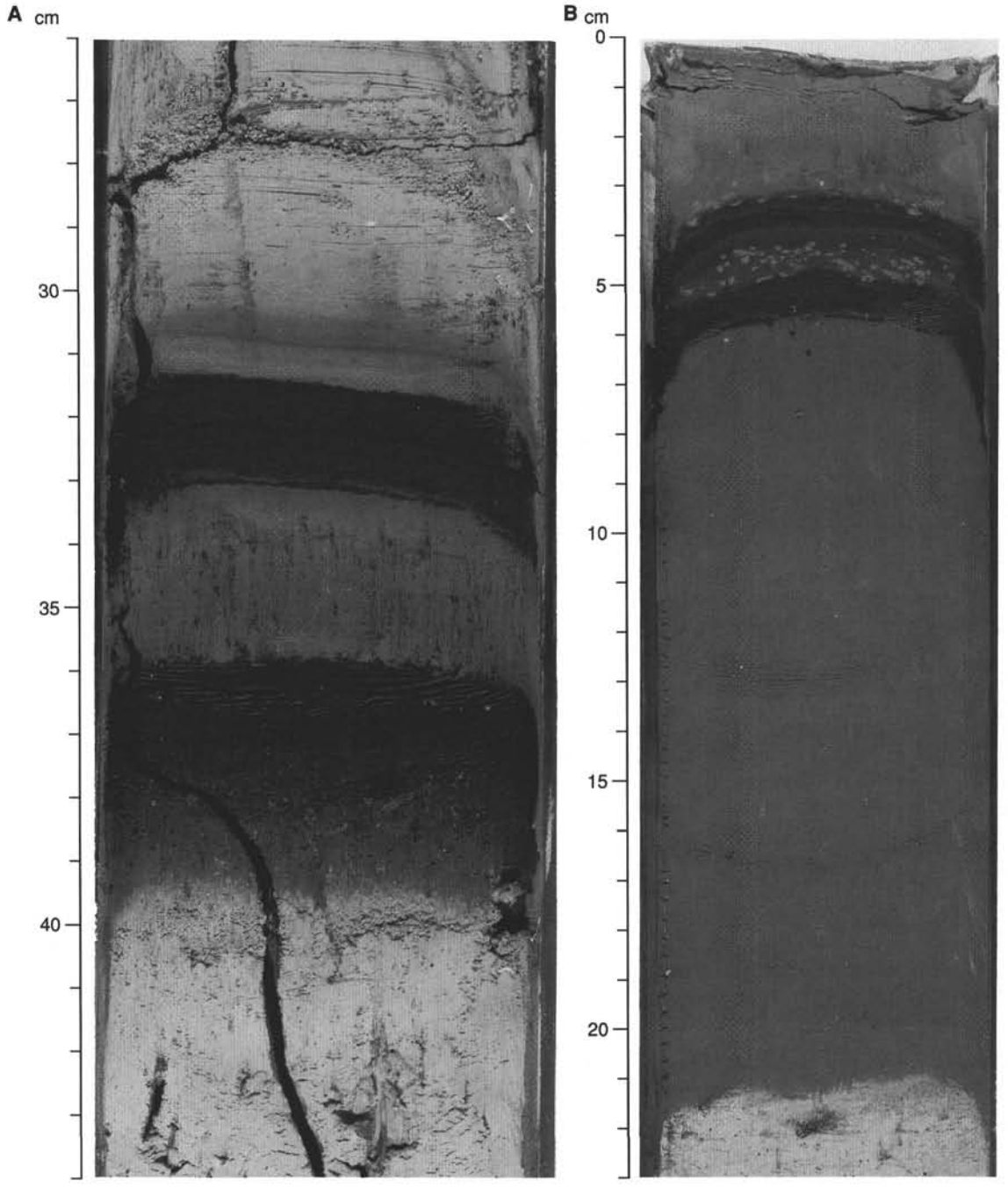

Figure 14. **A.** Example of a multiple-banded sapropel (Section 160-964A-6H-4, 26–44 cm). Note the gradational color boundary at base of lower band and sharp color boundaries elsewhere. The interval at 33–36 cm is slightly darker than the over- and underlying light-colored nannofossil ooze/clays, though this may be in part the result of postdepositional ?diagenetic alteration. **B.** Example of a multiple-banded sapropel (Section 160-964A-9H-7, 0–23 cm). Note the infilled *Chondrites* burrows "sandwiched" between two thin (approximately 1–0.5 cm thick) dark-colored intervals and also on the interface at the top of the upper dark-colored interval. It is interesting to note also the abrupt color change that occurs at approximately 21 cm in the core, and the flecks/blebs of light-colored sediment scattered throughout the darker interval between 6 and 21 cm.

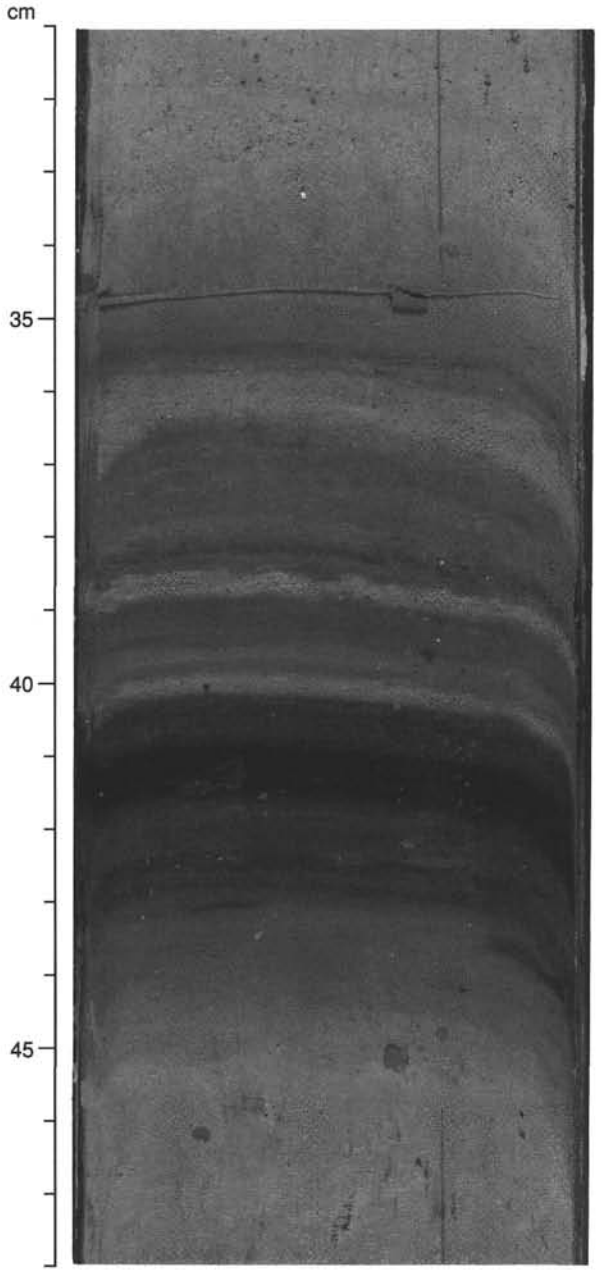

Figure 15. Example of a partially oxidized sapropel (Section 160-964C-3H-1, 31–48 cm). Note the highly distinctive color-banding, especially within the interval at 36–40 cm.

Attempts to correlate some of the oxidized sapropels between holes has corroborated previous observation with regard to the distribution of contemporaneous deposition and the spatial variability of sapropels and variable redox potential in the sedimentary column (Higgs et al., 1994).

BIOSTRATIGRAPHY AND SEDIMENTATION RATES

Calcareous Nannofossils

Calcareous nannofossils were studied from core-catcher samples and a supplemental sample from each section of core in Hole 964A. Two samples per section were also collected from Core 160-964D-8H to correlate with an interval in Hole 964A that was difficult to zone because of reworking.

The calcareous nannofossil biostratigraphy in Hole 964A is typified by assemblages that range from the Pleistocene through the early Pliocene in age. Calcareous nannofossils are abundant or common in all of the slides analyzed. Preservation is good, but overgrowths and broken specimens are common in samples that contain high quantities of silt and volcanic ash. These intervals of diminished preservation are usually from intervals that are interpreted as turbidites (see "Lithostratigraphy" section, this chapter) and contain reworked nannofossils. Reworked species of late middle Pliocene discoasters with Cretaceous forms vary in quantity from rare to few. The abundances of *Braarudosphaera bigelowii* and *Scyphosphaera* sp. fluctuate throughout the cores studied. A summary of the biostratigraphy is displayed in Figure 16.

The base of the first biozone (MNN21b) was detected in Sample 160-964A-1H, 84 cm. This zone is defined by the acme of *Emiliania huxleyi.* The accompanying assemblage includes small *Gephyrocapsa* (<3.5 µm), *Gephyrocapsa oceanica* s.l., *Helicosphaera kamptneri, Coccolithus pelagicus, Rhabdosphaera clavigera,* and *Pontosphaera japonica.*

Samples 160-964A-1H-2, 80 cm, through 2H-2, 50 cm, are in Zone MNN21a and contain *E. huxleyi* in quantities lower than those of the acme zone, which was identified upsection. The accompanying assemblage is similar to that found uphole. Minor reworking of the upper Pliocene sediments is evidenced by the presence of *Discoaster brouweri, Discoaster pentaradiatus, Discoaster surculus,* and *Discoaster tamalis.*

Samples 160-964A-2H-3, 90 cm, through 3H-3, 90 cm, were placed into Zone MNN20, which is a gap zone defined by the absence of both *E. huxleyi* and *Pseudoemiliania lacunosa.* The accompanying in situ and reworked assemblages are similar to those found uphole.

Samples 160-964A-3H-4, 90 cm, through 4H-3, 40 cm, contain nannofossils from Zone MNN19f. The upper boundary of the zone is defined by the last occurrence of *P. lacunosa,* whereas the lower boundary is defined by the first occurrence of *Gephyrocapsa* sp. 3. The placement of the upper boundary of this zone is difficult because *P. lacunosa* is found in rare abundances in samples uphole. The interpretation of where the zone begins in these samples is subjective and based solely upon an increase in abundance of *P. lacunosa* from rare to few. The uphole occurrences are interpreted as reworked, whereas the samples herein are considered in situ. This boundary will be refined by a quantitative analysis in a shore-based study. The in situ and reworked assemblages that accompany *P. lacunosa* are similar to those found uphole.

Samples 160-964A-4H-4, 62 cm, through 4H-CC contain nannofossils from Zone MNN19e. This interval is interpreted as a gap zone identified by the absence of both *Gephyrocapsa* sp. 3 and large *Gephyrocapsa* (>5.5 µm). Because *Helicosphaera sellii* was commonly found reworked upsection, the last occurrence of large *Gephyrocapsa* (>5.5 µm) was used as a marker for the base of this zone. Small *Gephyrocapsa* and *P. lacunosa* dominate the accompanying assemblage. Sample 160-964A-4H-7, 23 cm, is from a sapropel (see "Lithostratigraphy" section, this volume). The assemblage in this sample is both diverse and well preserved.

Samples 160-964A-5H-1, 62 cm, through 5H-7, 24 cm, contain nannofossils from Zone MNN19d. This zone is identified by the presence of large *Gephyrocapsa* (>5.5 µm). The accompanying in situ and reworked assemblages are similar to those found uphole.

Sample 160-964A-5H-CC contains nannofossils from Zone MNN19c. This zone is a gap zone defined at the base by the disappearance of *Calcidiscus macintyrei* and at the top by the appearance of large *Gephyrocapsa* (>5.5 µm). Small *Gephyrocapsa* and *G. oceanica* s.l. dominate the assemblage. Reworking is minimal.

Samples 160-964A-6H-1, 123 cm, and 6H-3, 57 cm, contain nannofossils from Zone MNN19b. This zone is identified by the presence of both *G. oceanica* s.l. and *C. macintyrei.* The accompanying

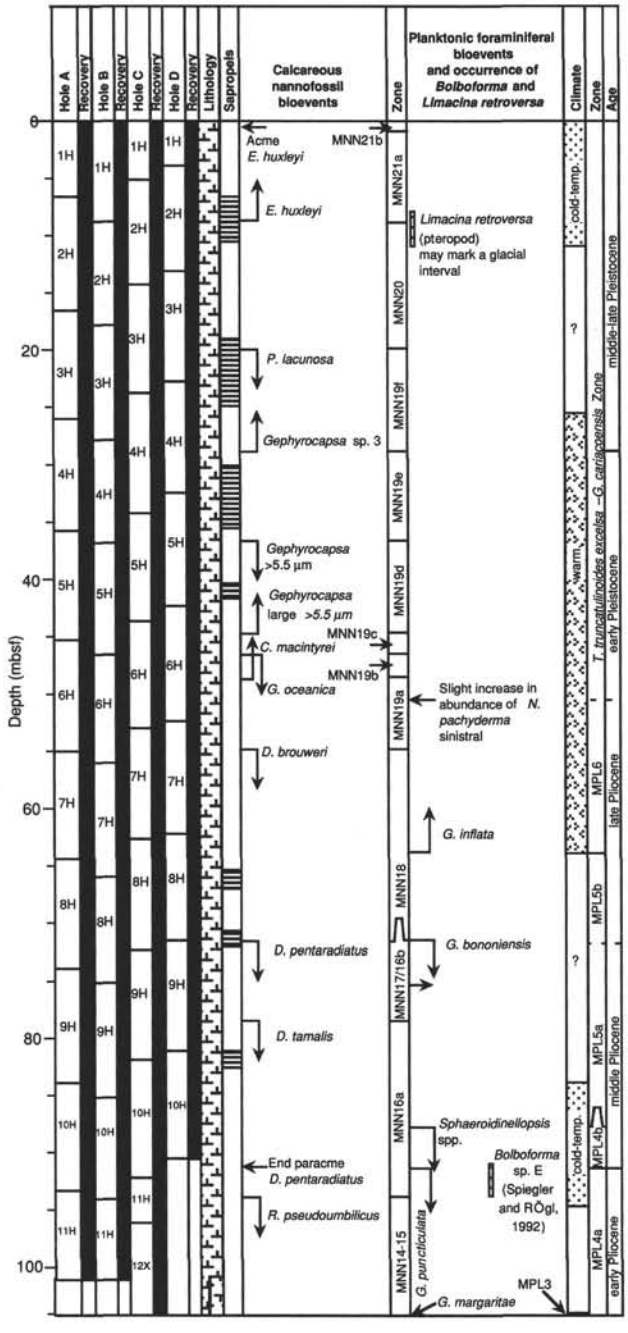

Figure 16. Composite of biostratigraphic events recognized at Site 964 including the lithostratigraphic record. The bars mark the distribution of *Limacina retroversa* (pteropod) and *Bolboforma* sp. E (Spiegler and Rögl, 1992). The base of the *Emiliania huxleyi* acme could not be identified with confidence during shipboard analysis.

in situ and reworked assemblages are similar to those found in the previous sample.

Samples 160-964A-6H-4, 92 cm, through 6H-7, 40 cm, contain nannofossils from Zone MNN19a. This zone is identified by the absence of both *G. oceanica* s.l. and *D. brouweri.* The accompanying assemblage is diverse and includes *H. kamptneri,* small *Gephyrocapsa, Syracosphaera pulchra,* and small reticulofenestrids.

Samples 160-964A-6H-CC and 8H-5, 80 cm, contain nannofossils from Zone MNN18. This zone is identified as the interval in which *D. brouweri* is present after the last occurrence of *D. pentaradiatus.* Fluctuations in the abundance of *Discoaster triradiatus* characterize the upper part of this interval starting at Sample 160-964A-7H-5, 51 cm. Reworked assemblages and diminished abundance are typical in the upper five sections of Core 160-964A-8H. This interval contains turbidites and is most likely missing some of the geologic section because of faulting (see "Lithostratigraphy" and "Structural Geology" sections, this chapter). Additional samples were collected from Hole 964D across this interval and used to augment the reworked intervals from Hole 964A. The uppermost samples from Core 160-964D-8H include common *D. brouweri* in the absence of other discoasters, which suggests that the samples belong in Zone MNN18.

Samples 160-964A-8H-6, 80 cm, through 9H-1, 80 cm, contain nannofossils from Zone MNN17–16b. This zone is defined as the interval that contains *D. pentaradiatus,* but is above the last common occurrence of *D. tamalis.* The accompanying in situ and reworked assemblages are similar to those found uphole.

Samples 160-964A-9H-2, 80 cm, through 10H-CC contain nannofossils belonging to Zone MNN16a. This zone is identified by the presence of *D. tamalis* above the last occurrence of *Reticulofenestra pseudoumbilicus* (>7 µm). The accompanying in situ assemblages are similar to those found in the Pliocene interval. The reworked nannofossils are similar to those found uphole.

Samples 160-964A-11H-1, 120 cm, through 11H-CC contain nannofossils belonging to Zone MNN14–15. This zone contains both *R. pseudoumbilicus* (>7 µm) and common specimens of *Discoaster asymmetricus.* The accompanying in situ assemblages are similar to those found uphole. The reworked nannofossils are similar to those found uphole.

Planktonic Foraminifers

Hole 964A was studied in detail in order to provide a complete stratigraphic record of the sedimentary sequence. Eleven core-catcher samples and 47 additional samples were analyzed for planktonic foraminiferal content. Planktonic foraminiferal assemblages were also analyzed in Samples 160-964B-2H-CC, 3H-CC, and 4H-CC and 160-964C-12X-CC.

Planktonic foraminifers are generally abundant to dominant at Site 964 and consist of diversified and poorly to well-preserved Pleistocene and Pliocene faunas. Using the zonation scheme of Cita (1975) emended by Sprovieri (1993), the interval spanning the *Truncorotalia truncatulinoides excelsa–Globigerina cariacoensis* Zones was identified for the Pleistocene and five zonal boundaries were identified for the Pliocene encompassing Zones MPL4a through MPL6.

As observed at Site 963, the zonal boundary between the *Truncorotalia truncatulinoides excelsa* and *Globigerina cariacoensis* Zones was not recognized owing to the scarcity of *T. truncatulinoides excelsa.* The two zones span the entire Pleistocene from Samples 160-964A-1H-2, 66–67 cm, through 6H-1, 31–33 cm.

Faunal assemblages are generally well preserved and abundant and very similar to those observed for Site 963.

The transition between the *T. truncatulinoides excelsa–G. cariacoensis* Zones and Zone MPL6, equated to the Pliocene/Pleistocene boundary, had no distinctive marker but probably occurs in Core 160-964A-6H between Sections 1 and 4, where an increase in the abundance of sinistral *Neogloboquadrina pachyderma* and the highest occurrence of the Pliocene taxon *Globigerinoides obliquus* were observed. Zone MPL6 is identified through Sample 160-964A-7H-7, 19–20 cm.

Globorotalia puncticulata, Globorotalia bononiensis, and *Globorotalia inflata* collectively represent a group of morphologically related taxa with a discontinuous distribution in the Mediterranean that provides an excellent stratigraphic zonation tool (Spaak, 1981). The lowest occurrence of *G. inflata* in Sample 160-964A-7H-7, 19–20 cm, marks the base of MPL6 and top of the Zone MPL5b. This lat-

ter zone was identified from Samples 160-964A-7H-CC through 8H-4, 138–140 cm.

Zone MPL5a was identified from Samples 160-964A-8H-6, 56–60 cm, through 10H-2, 129–131 cm. It is recognized by the last occurrence of *G. bononiensis* in Sample 160-964A-8H-6, 56–60 cm.

Samples 160-964A-10H-3, 129–131 cm, and 10H-4, 8–10 cm, contain *Sphaeroidinellopsis* spp. in the absence of *G. puncticulata.* This assemblage marks Zone MPL4b.

The highest occurrence of *G. puncticulata,* in Sample 160-964A-10H-5, 42–44 cm, marks the top of MPL4a.

Zone MPL3 was identified only in Sample 160-964C-12X-CC based on the presence of several specimens of *Globorotalia margaritae.*

Planktonic foraminiferal assemblages do not display significative changes throughout the sequence with the exception of the first occurrence and last occurrence of the marker species and climatically induced variations in species abundance. Recognized Pliocene taxa include *Orbulina universa, Orbulina bilobata, G. obliquus, Globigerinita juvenilis, Sphaeroidinellopsis subdehiscens, Sphaeroidinellopsis cocki, Globigerinella obesa, Neogloboquadrina acostaensis, Globigerina falconensis, G. inflata, Globorotalia crassaformis, Globigerinoides ruber, Globigerinoides sacculifer, Globigerinoides conglobatus, Globigerinoides quadrilobatus, Globigerinoides trilobus, Globigerinoides pyramidalis, Globigerinoides elongatus, Globorotalia scitula, Globigerina bulloides, Turborotalita quinqueloba, Globigerinita glutinata, Neogloboquadrina pachyderma* (both dextral and sinistral forms), *Neogloboquadrina dutertrei,* and *Zeaglobigerina woodi.*

Rare taxa include *Beella digitata, Globigerinita uvula, Tenuitella anfracta, Pulleniatina obliquiloculata,* and *Globigerinoides gomitulus.*

Reworking has not severely affected the planktonic foraminiferal assemblages, although many of the samples contain clearly reworked Pliocene, Miocene, Oligocene, and Eocene specimens (e.g., *Chiloguembelina* sp., *G. margaritae, Praeorbulina glomerosa, Praeorbulina transitoria, Globigerinoides subsacculifer, Paragloborotalia siakensis, Paragloborotalia birnageae, Paragloborotalia pseudokugleri, Pseudohastigerina* sp., *Pulleniatina praecursor, Turborotalita multiloba,* and *Zeaglobigerina druryi*).

Bolboforma

Only very few specimens of Bolboforma were found in Hole 964A. They occur in Samples 160-964A-10H-6, 9–12 cm, and 10H-5, 42–44 cm, (lower Pliocene) and they may possibly be attributed to *Bolboforma* sp. E (Spiegler and Rögl, 1992).

Several microfossil specimens morphologically similar to Bolboforma were also found in Hole 964A. They exhibit a rounded theca with a large aperture, some of which are bordered by a collar and an apparently reticulate wall texture. These forms occur from Samples 160-964A-6H-1, 31–33 cm, through 10H-6, 9–12 cm (lower Pleistocene to upper lower Pliocene). Scanning electron microscope studies on these forms will be needed to clarify their taxonomic position.

Paleoenvironmental Remarks

A preliminary paleoclimatic interpretation based on planktonic foraminiferal assemblages is reported in Figure 16.

The occurrence of abundant *Limacina retroversa* (cool-water pteropod) in Samples 160-964A-2H-2, 41–44 cm, and 2H-4, 32–34 cm, may indicate a glacial interval in Core 160-964A-2H.

Two samples were taken from within and three samples were taken near sapropels for foraminiferal analyses. Sample 160-964A-4H-7, 14–15 cm, is within a sapropel in the Pleistocene *T. truncatulinoides excelsa–G. cariacoensis* Zones. It contains common abundances of *G. bulloides, O. universa,* and *G. ruber* and may reflect a warm to temperate paleoclimate. In addition, the typical occurrence of *N. dutertrei* within this sapropel suggests a high supply of nutrients. The preceding conditions may have been temperate, as suggested by the occurrence of *Globorotalia crassaformis hessi* in Sample 160-964A-4H-7, 19–20 cm, just below the sapropel.

Three samples within the Pleistocene *T. truncatulinoides excelsa–G. cariacoensis* Zones were taken from two closely spaced sapropel events. Sample 160-964A-5H-1, 108–109 cm, occurs above the sapropel and may represent a warm paleoclimate owing to the common occurrence of *G. sacculifer, O. universa,* and *G. scitula.* Between the sapropels, Sample 160-964A-5H-1, 119–121 cm, contains a common abundance of *O. universa, G. conglobatus,* and *T. quinqueloba,* suggesting a warm paleoenvironment. Sample 160-964A-5H-1, 123–125 cm, occurring below the second sapropel, contains common abundances of *G. bulloides, O. universa,* and *G. ruber* and may reflect a warm to temperate paleoclimate.

The third studied sapropel (Sample 160-964A-9H-5, 91–94 cm) is within Zone MPL5a in the upper Pliocene. It contains abundant *O. universa* and *G. sacculifer* and may reflect a warm paleoenvironment.

Sedimentation Rates

Sedimentation rates for Hole 964A were calculated using 16 calcareous nannofossil and planktonic foraminiferal events (Table 4). The data are plotted on the age vs. depth curve shown in Figure 17.

Table 4. Stratigraphic list of calcareous nannofossil and planktonic foraminifer events for Site 964.

Event	Core, section, interval (cm)	Depth (mbsf)	Depth (mcd)	Age (Ma)
	160-964A-			
FO *E. huxleyi**	2H-2, 80	9.1	8.72	0.26
LO *P. lacunosa*	3H-4, 90	21.70	21.39	0.46
FO *Gephyrocapsa* sp. 3	4H-3, 40–42	29.22	29.89	0.99
LO *Gephyrocapsa* >5.5 µm	5H-1, 62	35.92	37.33	1.25
FO *Gephyrocapsa* >5.5 µm	5H-7, 24	44.64	46.05	1.5
LO *C. macintyrei*	6H-1, 123	46.03	48.50	1.62
FO *G. oceanica* s.l.	6H-3, 126	49.06	51.53	1.75
Increase in abundance of *N. pachyderma* sinistral	6H-4, 73–75	50.04	52.51	1.81
LO *D. brouweri*	6H-CC	54.48	56.95	1.99
FO *G. inflata*	7H-7, 19–22	63.49	67.12	2.13
LO *G. bononiensis*	8H-6, 56–60	71.86	76.75	2.45
LO *D. pentaradiatus*	8H-6, 80	72.11	76.97	2.51
LCO *D. tamalis*	9H-2, 80	75.60	88.74	2.82
LO *Sphaeroidinellopsis* spp.	10H-3, 129–131	87.10	99.60	3.22
LO *G. puncticulata*	10H-5, 42–44	89.23	101.73	3.57
LO *R. pseudoumbilicus*	11H-1, 120	93.50	106.47	3.85

Notes: FO = first occurrence; LO = last occurrence; LCO = last common occurrence; * = to be confirmed by scanning electron microscopy.

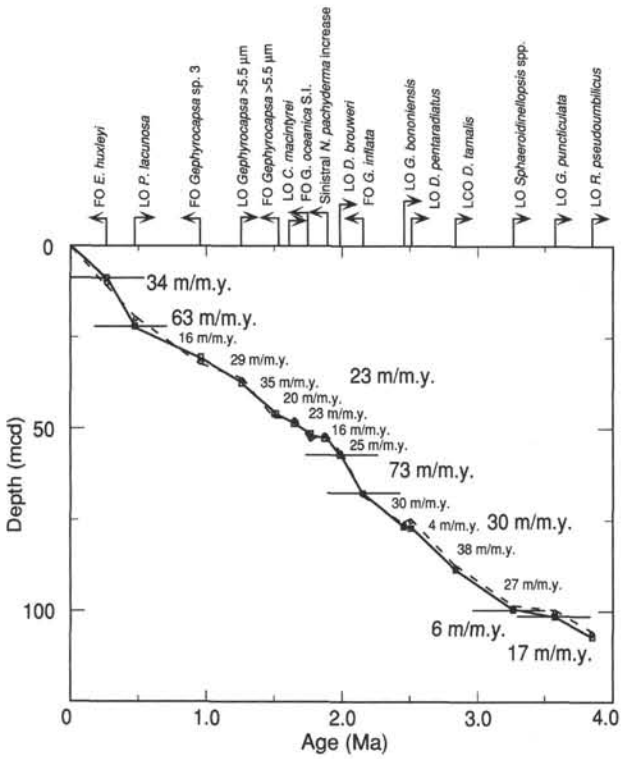

Figure 17. Age vs. depth diagram showing selected calcareous nannofossil and planktonic foraminifer datums with corresponding sedimentation rates. The line corresponds to the sample where the marker species was found for a corresponding first or last occurrence datum; the dashed line corresponds to the nearest sample where the marker species was not found.

An error line (dashed) is shown on the figure to indicate the degree of uncertainty as to the location of the nannofossil and foraminiferal events within the hole.

Calculated sedimentation rates vary from 4 to 73 m/m.y. through the sequence. Seven significant shifts in sedimentation rates can be observed. From the seafloor to the first occurrence of *E. huxleyi* (0.26 Ma) the sedimentation rate was approximately 34 m/m.y. The sedimentation rate increased to 63 m/m.y. in the interval from the first occurrence of *E. huxleyi* to the last occurrence of *P. lacunosa* (0.46 Ma). Sedimentation generally declined to 23 m/m.y. in the interval from *P. lacunosa* to the last occurrence of *D. brouweri* (1.99 Ma). In the interval between the latter bioevent and the first occurrence of *G. inflata* (2.13 Ma), the sedimentation rate reached a maximum of 73 m/m.y. From the first occurrence of *G. inflata* to the last occurrence of *Sphaeroidinellopsis* spp. (3.22 Ma), the average sedimentation rate declined to 30 m/m.y. The sedimentation rate further declined to a minimum of 6 m/m.y. from the last occurrence of *Sphaeroidinellopsis* spp. to the last occurrence of *G. puncticulata* (3.57 Ma). The final interval, from the last occurrence of *G. puncticulata* to the last occurrence of *R. pseudoumbilicus* (3.85 Ma), showed a sedimentation rate of 17 m/m.y.

PALEOMAGNETISM

Retrieval of a detailed and complete stratigraphic record was a major aim of drilling at Site 964. Paleomagnetic measurements were therefore made on cores from Holes 964A through 964E in order to obtain a high-resolution magnetostratigraphy. Paleomagnetic measurements at Site 964 followed the methods discussed in the "Explanatory Notes" chapter (this volume). The NRM was routinely measured at 10-cm intervals on the archive half of each core section after AF demagnetization at 20 mT for Hole 964A and at 25 mT for Holes 964B, 964C, 964D, and 964E. Rapid core recovery precluded demagnetization at more than a single level. NRM intensities were measurable throughout the 100-m sequence recovered and were well above the noise level of the magnetometer (Fig. 18). Large intensity peaks, most of which are associated with sapropels, are evident at each hole at Site 964. The high intensities in the sapropels most likely result from diagenetic enhancement, a fuller description of which is given by Roberts et al. (this volume).

Numerous zones of normal and reverse polarity are evident on whole-core logs of demagnetized inclination for Holes 964A through 964D (Fig. 19). However, there is no clear correlation among polarity zones for the different holes. Discrete samples were taken from every core section in Hole 964A. Stepwise AF demagnetization of selected discrete samples reveals characteristic remanence components that are directed toward the origin of vector component diagrams (Fig. 20). Inclinations derived from stably magnetized discrete samples from Hole 964A are plotted along with the whole-core data in Figure 21. In the upper 45 m of Hole 964A, the agreement between the two types of data is good, with the discrete-sample data reproducing several features in the whole-core record. However, discrepancies between whole-core and discrete samples were observed in two stratigraphic intervals (69 and 85–92 mbsf). Inclinations from the discrete data in these intervals indicate shallow reversed polarity, in contrast to the whole-core data, which are indicative of normal polarity. This result is enigmatic because characteristic remanence directions are isolated by peak AFs of 20–25 mT in discrete samples from this interval (Fig. 20D). The fact that the whole-core results do not indicate reverse polarity at the same demagnetization level suggests that the in-line demagnetization process is less efficient in removing secondary components of magnetization and that whole-core results may be contaminated by normal overprinting. The coercivity spectra of many demagnetized samples indicate the presence of a magnetically "hard" mineral such as hematite (Fig. 20A, B). This is consistent with the occurrence of intervals of red sediment in which significant hematite was observed in smear slides (e.g., Sample 160-964B-2H-7, 20 cm). Because hematite is relatively resistant to AF demagnetization, it will be necessary to undertake thermal demagnetization studies in order to assess the contribution of different magnetic minerals to the sediment magnetization and to check the reliability of the results from AF demagnetization studies. Any polarity information inferred from Figure 19 must be considered preliminary until a more thorough characterization of the magnetization can be made. Despite the preliminary nature of these results and the likelihood of normal overprinting, the whole-core record may permit derivation of an initial, but incomplete, magnetic polarity stratigraphy. Intervals where reverse polarities are consistently recorded are considered more reliable, because such zones are less likely to have been adversely affected by normal polarity overprinting during the Brunhes Chron or from overprinting imparted by the drill string or BHA (e.g., "Paleomagnetism" section, "Site 963" chapter, this volume).

Construction of a magnetic polarity stratigraphy can be attempted by splicing together a composite record from undisturbed and continuous sequences in each hole. The principal means of correlation was the identification of matching features in the color reflectance and physical stratigraphic records, including correlations between sapropels from overlapping cores from adjacent holes at Site 964 (see "Lithostratigraphy" and "Composite Depths" sections, this chapter). Significant color variations throughout the stratigraphic sequence make color reflectance the most useful parameter for interhole correlation. The color reflectance and sapropel correlations were used to devise a composite record (see "Composite Depths" section, this chapter) that approximates a continuous sequence. Direct comparisons of the paleomagnetic record can be made where similar stratigraphic sequences were identified in different holes.

There is generally good agreement among the paleomagnetic records from the upper 25 m of all holes (Fig. 20). This correlation is evident using the meter composite depth scale for Holes 964A and

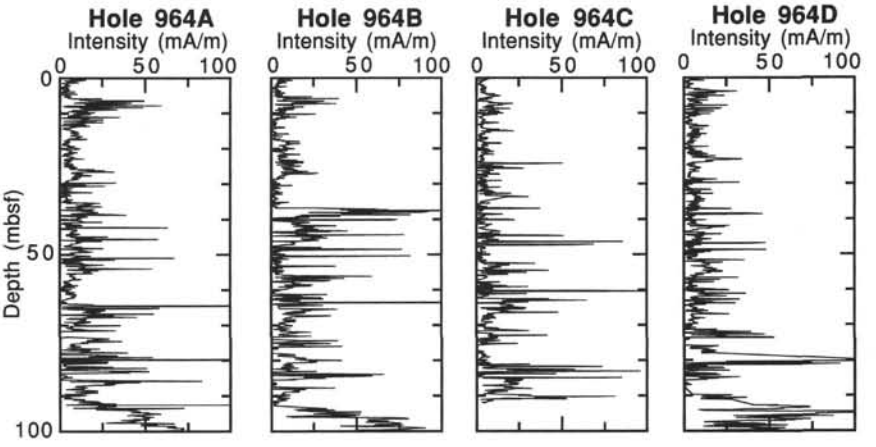

Figure 18. NRM intensity after AF demagnetization at 20 mT for Hole 964A and at 25 mT for Holes 964B, 964C, and 964D. The results from Hole 964E are not shown because a complete stratigraphic sequence was not recovered at that hole.

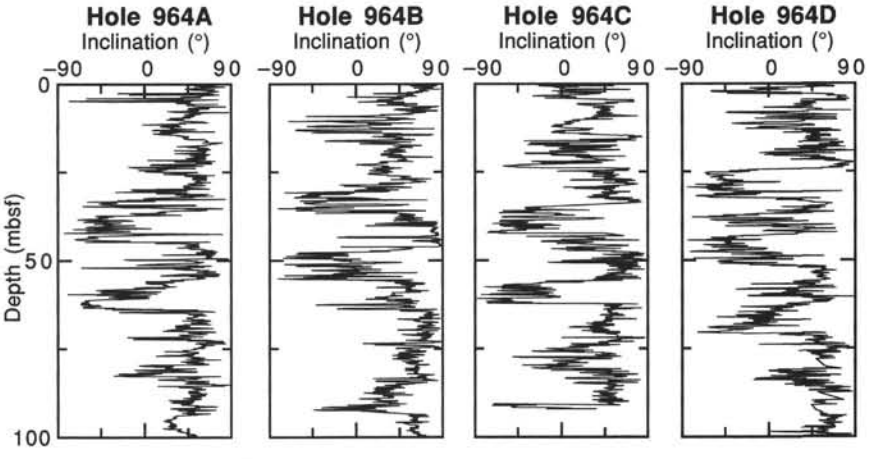

Figure 19. Paleomagnetic inclination measured on archive-half cores using the shipboard pass-through magnetometer for Hole 964A (after AF demagnetization at 20 mT) and Holes 964B, 964C, and 964D (after AF demagnetization at 25 mT). The results from Hole 964E are not shown because a complete stratigraphic sequence was not recovered in that hole.

964D (Fig. 22). Minor offsets between features in these records correspond with minor offsets in the shipboard correlation of color reflectance features (Fig. 27 from "Composite Depths" section, this chapter). Color reflectance variations cannot be correlated in the interval from 25.5 to 30 mcd, whereas correlation is again possible below 30.5 mcd. The paleomagnetic records in the interval from 25.5 to 30 mcd are also markedly different (Fig. 22). Hole 964A records a zone of normal polarity, whereas Hole 964D records a reverse to normal polarity transition. Core 160-964D-4H may contain the most complete record of the time interval containing the Matuyama/Brunhes polarity transition (at about 26 mcd), which is not evident in any of the other records. Micropaleontological results from Hole 964A indicate that the first occurrence of *Gephyrocapsa* sp. 3 occurs within Core 160-964A-4H (see "Biostratigraphy and Sedimentation Rates" section, this chapter). This datum normally occurs in the Jaramillo Subchron at about 0.99 Ma (Sprovieri, 1993), suggesting that the zone of normal polarity recorded in the upper part of Core 160-964A-4H (at about 26.5–30 mbsf) is of Jaramillo age and that this material has been juxtaposed against sediments of Brunhes age. This interpretation implies that there is an interval of reverse polarity that is missing in three of the recovered records. If this interpretation is correct, it suggests significant structural displacement that may have been accommodated along a normal fault although there is little structural evidence to support such a large displacement (see "Structural Geology" section, this chapter). Nevertheless, this observation has significant implications for the continuity of the recovered stratigraphic sequences and it further justifies the use of a composite-section approach to establish a complete stratigraphic record from Site 964. It also suggests that there may be difficulties in making detailed comparisons between the Site 964 records and the nearby KC01B piston core record of Dekkers et al. (1994). The relationship between these records must be checked by more detailed post-cruise investigations.

Zones of reversed polarity that presumably represent the Matuyama Chron are evident in the whole-core inclination logs, as are zones of normal polarity that may represent the Jaramillo and Olduvai Subchrons and the Gauss Chron (Fig. 19). Detailed comparison of records correlated by color reflectance data do not always reveal an unambiguous polarity interpretation. This may be due to unrecognized imprecisions in the composite stratigraphy or to variability in normal overprinting between records from adjacent holes. It is not possible to distinguish between these possibilities with the current data set, and construction of an accurate magnetostratigraphy awaits detailed post-cruise studies on discrete samples.

STRUCTURAL GEOLOGY

The six holes drilled at Site 964 all contain a horizontally bedded succession with numerous faults. It was possible to measure these faults in three dimensions on the ship only in Holes 964A and 964D because of the necessity of preserving intact sections for post-cruise sapropel sampling. Tensor orientation tool data are available for Cores 160-964A-3H through 9H and 160-964D-8H through 12H, and in these intervals the calculated true dips were corrected to geographic coordinates. Table 5 records the data collected.

The intensity and abundance of the deformation structures vary from core to core and from hole to hole. Fault deformation is present in all holes, but is most common in Hole 964A. The most intense faulting occurs in Section 160-964B-3H-1, 30–55 cm, where both normal and reverse microfaults were observed. Tilted bedding was

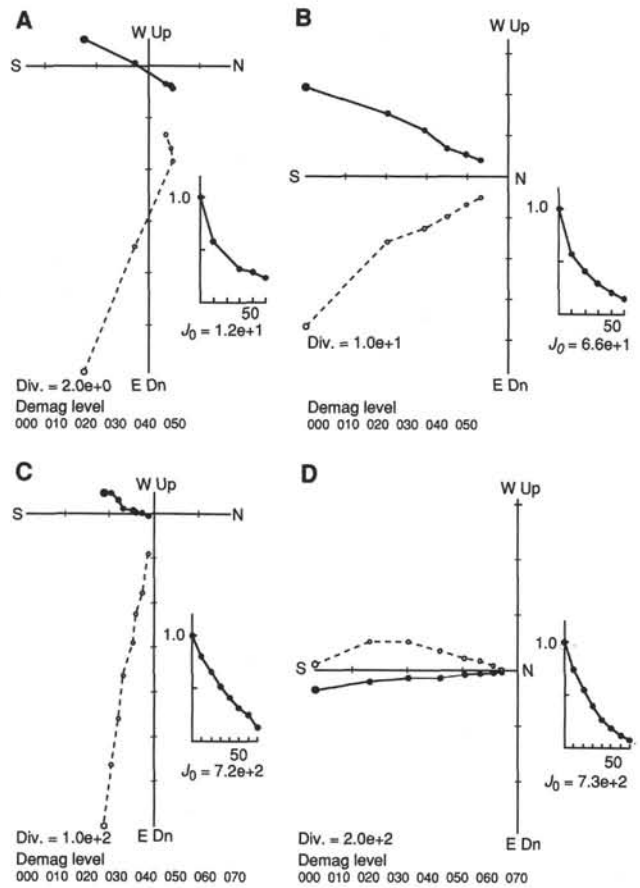

Figure 20. Representative vector component demagnetization diagrams for discrete samples that were subjected to stepwise AF demagnetization. **A.** Sample 160-964A-3H-4, 44 cm (21.24 mbsf); **B.** Sample 160-964A-6H-2, 66 cm (46.92 mbsf); **C.** Sample 160-964A-11H-7, 59 cm (101.89 mbsf); **D.** Sample 160-964A-10H-5, 119 cm (89.99 mbsf). Open (solid) symbols represent projections onto the vertical (horizontal) plane. Demagnetization steps (in mT) are shown below each diagram.

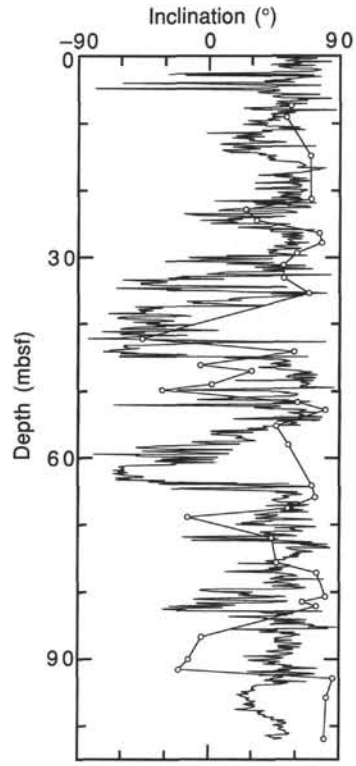

Figure 21. Whole-core inclination for Hole 964A compared with inclinations from stepwise-demagnetized discrete samples. Inclinations for discrete samples were determined by linear regression fits to multiple demagnetization points in each case. These data reproduce many of the features seen in the whole-core results; however, in some intervals (e.g., 69, 85–92 mbsf) it is evident that normal overprints obscure the primary polarity. A polarity log is not shown because of the stratigraphic complexities described in the text.

identified mainly in Holes 964C and 964D (e.g., Sections 160-964C-1H-1 and 2 and 160-964C-2H-1 through 3).

Description of the Faults

Normal Faults

The majority of the faults observed at Site 964 are high-angle planar faults with normal offsets in the order of 0.5–2 cm (e.g., Sections 160-964B-7H-1, 160-964C-3H-4, and 160-964D-3H-1, 5H-1, and 10H-1). The angles of dip of almost all of the faults for which it was possible to calculate a true dip cluster between 45° and 90° (Fig. 23). Along some of the faults (e.g., in Cores 160-964A-9H and 10H), material of contrasting color was entrained along the fault planes. Comparative studies of smear slides of the material from both within these fault zones and the host sediments revealed no obvious difference in grain size or composition. Sporadic planar discontinuities with dark organic-rich material entrained along them were observed (e.g., Fig. 24).

A variety of fault geometries was observed. The most common is a single high-angle fracture (Fig. 25). Small-scale grabenlike structures are visible both on the core face and perpendicular to it, in the 360°–180° core coordinates plane. Many of the faults, although clearly visible on one side and in the center of the core, were difficult to trace across the entire core face (Fig. 25, F_1). In many cases the area of ambiguity exists close to the core liner, where lithologic and/or color contrasts are limited. A lower hemisphere stereographic projection plot of poles to fault planes (Fig. 26) illustrates a nearly symmetrical distribution, with faults striking north-south with respect to the core coordinates.

Reverse Faults

Rare reverse faults were observed at Site 964. In general, these are of considerably lower angle than the normal faults. Offsets are in the order of a few centimeters or less. It is not possible to determine the sense of movement on a fault where the offset is too large to allow the matching of beds above and below it. Many of faults where this is the case are higher angle than the reverse faults identified, and it is not possible to exclude a reverse sense of movement for them.

Strike-slip Faults

A phenomenon observed consistently in all the holes is the appearance of long, nearly vertical, curving to irregular fractures with indeterminate offsets (e.g., Sections 160-964C-3H-6 and 160-964E-5H-5). Where the offset can be seen, it appears to vary along the length of the fracture. These faults could have a strike-slip component of movement.

Other Evidence of Faulting

Interhole correlation (e.g., Cores 7H and 8H in Holes 964A and 964D) suggests that faulting has taken place, producing stratigraphic

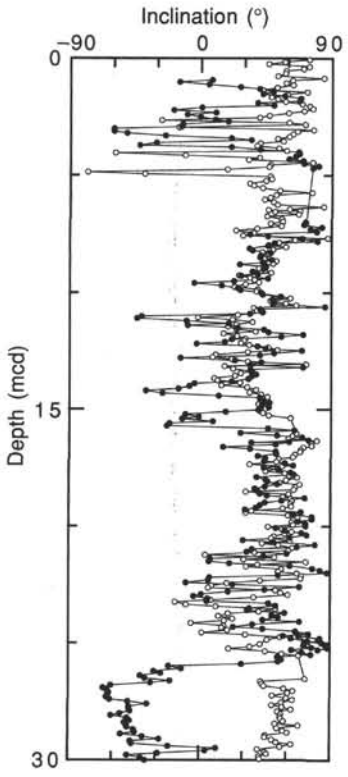

Figure 22. Correlation of paleomagnetic inclination data between Holes 964A and 964D using the composite depth section (see text) between 0 and 30 mcd. Open (closed) circles indicate inclination data obtained on the pass-through magnetometer (cf., Fig. 19) for Hole 964A (Hole 964D). The Matuyama/Brunhes polarity transition is interpreted to occur at 25–26 mbsf in Hole 964D.

gaps and leading to correlation problems between holes (see also "Lithostratigraphy" section, this chapter). Although no single large-scale fault was identified in any of the cores that might explain the correlation difficulty, small normal faults were identified in the correlative interval at the top of Cores 160-964A-8H, 160-964B-8H, and 160-964D-8H and at the bottom of Section 160-964E-4H-4. Interhole correlation estimates of the lithostratigraphic gap in this area (see "Lithostratigraphy" section, this chapter) are in the order of 5–6 m.

Interpretation

It is difficult to explain the distribution of the faults with respect to core coordinates (Fig. 26) without suggesting either that there is a sampling bias with respect to the orientation of the section cut or that some of them were induced by the drilling process. These possibilities are explored further in Kopf and Flecker (this volume).

Figure 26 shows poles to the fault planes corrected to geographic coordinates using the Tensor data. Although there is some doubt about the origin of some of these faults, the systematic northwest to southeast trend of the strike of the faults, as corrected, suggests that part of the fault population measured represents real tectonically generated features. The northeast-southwest strike is parallel to bathymetric lineaments in the area (see "Geological Setting" section, this chapter). Site 964 was drilled on the toe of the Calabrian accretionary wedge. This ridge strikes northeast-southwest, subparallel to the strike of the fault data set obtained here. It is thus possible that the bathymetric features reflect tectonic movement recorded in the faults measured in the Site 964 cores.

COMPOSITE DEPTHS

High-resolution (2–10-cm scale) data collected on whole cores on the MST and percent color reflectance collected on split cores from Holes 964A through 964F were used to determine depth offsets in the composite section. On the composite depth scale, sedimentary features present in adjacent holes are aligned so that they occur at approximately the same depth. Working from the top of the sedimentary sequence, a constant was added to the depth in meters below seafloor for each core in each hole to arrive at a composite depth for that core. The depth offsets that form the composite depth section are given in Table 6. Continuity of the sedimentary sequence was documented for the entire section above the lower turbidite at approximately 105 mcd.

Percent color reflectance (collected at 2-cm intervals) was the primary parameter used for correlation purposes at this site. Magnetic susceptibility data (collected at 5-cm intervals) provided supplemental verification of overlap and depth offsets at several depth intervals. GRAPE wet-bulk density variations were of low amplitude and thus not useful for composite depth construction. Natural gamma-ray data were collected only at Hole 964A.

The percent color reflectance records (550-nm wavelength) and magnetic susceptibility data used to verify core overlap for Site 964 are shown on a composite depth scale in Figures 27 and 28, respectively. The cores from Holes 964A through 964D provide continuous overlap to almost 105 mcd (base of Core 10H in each hole). Cores below this level in each of Holes 964A through 964D could not be tied confidently into the composite section. These lowermost cores consist primarily of a turbidite (see "Lithostratigraphy" section, this chapter) with little or no variation in color reflectance, magnetic susceptibility, or bulk density.

Significant stratigraphic gaps (greater than 2 m) occur in all sequences. The largest gap, nearly 7 m, occurs between Cores 160-964A-8H and 9H. Note that the lower 2–3 m of Core 160-964A-8H most likely correlates to similar features at 84–86 mcd in Holes 964B through 964D. This misalignment results because the shipboard processing software could not separate sections within an individual core. Other large gaps were found between Cores 160-964E-1H and 2H (5 m), 160-964D-4H and 5H (4 m), 160-964C-9H and 10H (4 m), and 160-964B-9H and 10H (3 m). Gaps of 1 or 2 m are common. Significant coring overlap (greater than 50 cm) between cores within one hole occurs only between Cores 160-964E-2H and 3H (nearly 3 m). Confirmation of the continuity of the section in the upper 105 mcd was possible only after Hole 964E was spot cored over the intervals 0–24.5 and 57–85.5 mbsf.

Stretching and compression of the sedimentary features in the aligned cores indicate distortion of the cored sequence. Because much of the distortion occurs within individual cores on depth scales of less than 9 m it was not possible to align many features in the color reflectance and magnetic susceptibility records accurately by simply adding a constant to the mbsf core depth. The section at Site 964 had significantly greater within-core distortion than at Site 963. In many cases, this distortion was the result of high-angle faults removing a section within one core relative to the equivalent core in another hole (see "Structural Geology," "Lithostratigraphy," and "Paleomagnetism" sections, this chapter). Within-core scale changes will require post-cruise processing to align the distorted sedimentary features.

The base of the composite depth construction is at approximately 105 mcd, where between-hole offsets could no longer be estimated. The successive cores were placed at their original mbsf depth plus the accumulated depth offset. From 0 to approximately 92 mbsf (105 mcd), the growth of the mcd scale relative to the mbsf scale is about 13% (Fig. 29).

Following construction of the composite depth section for Site 964, a single spliced record was assembled from the aligned cores.

Table 5. Structural data collected at Site 964.

Core, section, interval (cm)	Depth (mbsf)	Feature	Offset width (cm)	Orientation on core face (degrees)		Second apparent orientation (degrees)		Calculated orientation (degrees)		Geographic orientation (degrees)		Comments
				Apparent dip	Direction	Apparent dip	Direction	Dip	Direction	Dip	Direction	
160-964A-												
2H-1, 89–91	7.69	F	1	85	90	0	72	88	162	88	308	Normal? Drilling disturbance
4H-2, 13–22	27.43	F_2	4	41	90	0	308	55	38	55	184	Normal
4H-2, 20–38	27.5	F_1	5	67	270	0	316	73	226	73	12	F_1 and F_4 older than F_2 and F_3
4H-2, 121–132	28.51	F_3	2	72	270	0	40	76	310	76	96	Normal
4H-2, 126–141	28.56	F_4	4	67	270	0	70	82	340	82	126	Normal
4H-1, 100–127	26.8	F										Listric
4H-1, 135–150	27.15	F_2		70	270	0	56	79	326	79	112	Normal
4H-3, 82–100	29.62	F_1	2	11	270	0	29	13	299	13	85	Normal
4H-3, 93–104	29.73	F_2	4	41	270	0	29	45	299	45	85	Normal
4H-4, 64–77	30.94	F		55	90	0	35	60	125	60	271	Direction unknown
6H-1, 0–13	44.8	F		43	90	35	0	49	53	49	126	Normal
6H-3, 92–101	48.72	F		54	270	310	0	61	229	61	302	Normal
6H-4, 2–10	49.32	F_1	00.5	78	90							Normal
6H-4, 16–30	49.46	F_7		45	270							Normal
6H-4, 23–32	49.53	F_2		45	270							Normal
6H-4, 100–110	50.3	F_3		52	270							Normal
6H-4, 113–120	50.43	F_4	0.5	85	270							Normal
6H-4, 133–139	50.63	F_5	1	54	270	60	0	66	322	66	35	Normal (see VCD form on CD-ROM [back pocket])
6H-4, 133–139	50.63	F_8	1	54	270	82	180	82	191	82	264	Normal (see VCD form on CD-ROM [back pocket])
6H-4, 133–150	50.63	F_6	2.5	65	90	62	0	71	49	71	122	Normal
6H-5, 0–14	50.8	F_1	1	74	90	65	0	76	58	76	131	Normal
6H-5, 32–50	51.12	F_2	3	52	90	71	0	73	24	73	97	Normal
6H-7, 0–24	53.8	F	1.5	72	90							Normal
7H-4, 4–19	58.84	F_1	3	65	90	59	180	70	128	70	359	Normal
7H-4, 24–37	59.04	F_2	4	65	90	40	180	67	111	67	342	Normal
7H-4, 36–45	59.16	F_3	1	58	270	22	180	59	256	59	127	Reverse
7H-4, 45–64	59.25	F_4	3	66	270	28	180	68	293	68	164	Listric normal fault with splay
7H-4, 47–53	59.27	F_5	2	71	270	52	180	73	246	73	117	Normal
7H-4, 50–67	59.3	F_6	0.5	70	270	23	0	70	279	70	150	Normal
7H-4, 92–107	59.72	F_7	1	73	270	66	0	76	304	76	175	Normal
7H-4, 100–114	59.8	F_8	1	85	270	0	40	86	310	86	181	Normal
7H-4, 110–115	59.9	F_9	1									Normal
7H-4, 118–130	59.98	F_{11}	>13	65	90	7	180	65	93	65	324	Normal
7H-4, 119–122	59.99	F_{10}	0.5									Normal
7H-7, 15–45	63.45	F_1	0.5	85	270							Normal, not enough color to see in three dimensions
7H-7, 45–57	63.75	F_2	1	63	90							Normal, not enough color to see in three dimensions
7H-7, 62–76	63.92	F_3	1	71	270							Normal, not enough color to see in three dimensions
7H-7, 115–130	64.45	F_4	2	78	90							Normal, not enough color to see in three dimensions
7H-7, 118–132	64.48	F_5	5	65	90							Normal, not enough color to see in three dimensions
8H-3, 25–35	67.05	F		62	270							Normal
8H-4, 1–12	68.31	F_1		35	270	51	0	55	330	55	163	Normal
8H-4, 1–12	68.31	F_2	1.5	90	270	0	46	90	316	90	149	Normal
8H-4, 111–118	69.41	F_3	>3.5	40	270	60	0	63	334	63	167	Normal
8H-5, 49–57	70.29	F_1	2	45	90	64	180	66	154	66	347	Normal
8H-5, 67–76	70.47	F_2		65	270	12	180	65	264	65	97	Normal(?)
8H-6, 33–34	71.63	F	0.5									Normal
9H-2, 57–66	75.37	FR_1	0.1	69	90	338	0	69	99	69	33	Fracture (change in color due to fluid expulsion)
9H-2, 62–74	75.42	F	8.5	62	270	335	0	63	256	63	190	Reverse
9H-2, 77–94	75.57	FR_2	0.1	72	90	38	0	73	76	73	10	Fracture (change in color due to fluid expulsion)
9H-2, 117–134	75.97	FR_3	0.2	71	270	35	0	71	284	71	218	Fracture (change in color due to fluid expulsion)
10H-3, 50–64	86.3	FR	0.1	70	90	40	0	71	73	71	174	Fracture (change in color due to fluid expulsion)
10H-3, 103–128	87	FR?	<0.1	81	90							Fluid-escape structure
10H-4, 50–64	88	FR	2.5	70	90	5	0	70	88	70	189	Fracture (change in color due to fluid expulsion)
10H-4, 62–77	87.92	FR?	2	76	90	358	0	76	91	76	192	Fluid path (change in color)
10H-5, 42–88	89.22	FR?	0.1 to 0.6	Vertical								Fluid-escape structure
160-964D-												
3H-1, 80–115	14.4	F	3	84	90	0	20	84	110			Steep reverse fault
3H-1, 110–150	14.7	F	3.5	90	0	0	28	90	298			Steep reverse fault
3H-2, 0–38	15.1	F		86	90	0	25	86	115			Steep reverse fault
5H-1, 40–56	33	F	8	65	270	0	350	65	265			Normal fault; sapropel on fault plane
5H-1, 110–150	33.7	F		19	270	0	352	19	262			Normal/reverse?
5H-2, 0–38	34.1	F	3–11	73	270	0	346	73	256			Normal fault, strike-slip
5H-2, 0–31	34.1	F	14	90	0	0	355	90	65			Normal fault

Table 5 (continued).

Core, section, interval (cm)	Depth (mbsf)	Feature	Offset width (cm)	Orientation on core face (degrees)		Second apparent orientation (degrees)		Calculated orientation (degrees)		Geographic orientation (degrees)		Comments
				Apparent dip	Direction	Apparent dip	Direction	Dip	Direction	Dip	Direction	
5H-2, 113–123	35.23	F		62	90	0	0	62	90			Shear zone (see VCD form on CD-ROM [back pocket])
7H-1, 119–142	52.79	F	1.5	70	90	0	336	72	66			Normal fault
7H-3, 71–92	55.31	F	4	72	90	0	342	73	72			Normal fault
7H-5, 120–135	58.8	F	1	62	90							Normal fault
7H-5, 134–150	58.94	F		53	90	Vertical		53	90			Normal fault
7H-6, 0–10	59.1	F		58	90	0	338	60	68			?
7H-6, 36–49	59.46	F		66	90	0	329	64	59			?
8H-1, 8–24	61.18	F	2	78	90	0	45	10	135	10	84	Normal fault
8H-1, 45–52	61.55	F	>10	55	270	0	38	61	308	61	1	Reverse fault
8H-1, 78–95	61.88	F		65	90	0	300	77	210	77	263	Normal fault
8H-3, 8–27	64.18	F	1	79	270	0	330	80	60	80	113	Normal fault
8H-3, 64–86	64.74	F	>9?	73	270	0	180	73	270	73	323	Normal fault
8H-4, 6–20	65.66	F	5	62	270	0	10	62	280	62	333	Normal fault
8H-4, 66–75	66.26	F	4	72	90	0	61	81	151	81	204	Normal fault
8H-5, 93–106	68.03	F	1	56	90	0	315	65	45	65	98	Normal fault
8H-5, 97–100	68.07	F	1	85	270	0	342	85	252	85	305	Normal fault
8H-6, 8–17	68.68	F	1	52	90	0	335	55	65	55	118	Normal fault
8H-6, 119–128	69.79	F	1	51	90	0	340	53	70	53	123	Normal fault
9H-1, 40–54	71	F	3	70	270	0	26	72	296	72	29	Normal fault
9H-1, 68–78	71.28	F	>10	65	270	0	23	67	293	67	26	Normal/reverse?
9H-5, 31–53	76.91	F		68	270	0	25	70	295	70	28	Normal/reverse?
9H-5, 126–143	77.86	F	3	70	90	0	334	72	64	72	157	Normal fault
10H-3, 0–23	83.1	F	4	69	90	0	17	70	107	70	253	Normal fault
10H-3, 12–25	83.22	F		55	90	0	25	58	115	58	261	Normal fault

Note: Feature symbols defined in Table 2 ("Explanatory Notes" chapter, this volume).

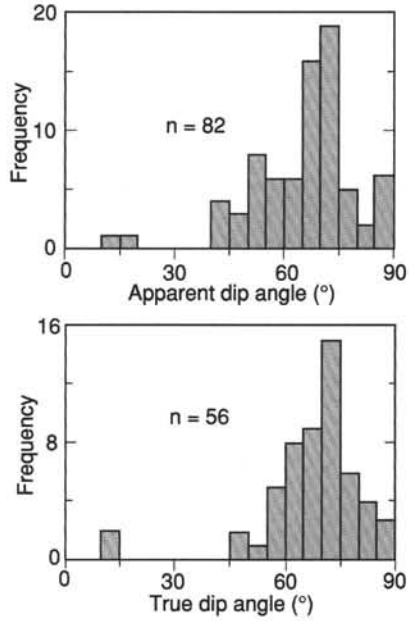

Figure 23. Histogram showing angles of apparent dip and calculated true dip of fault planes from Holes 964A and 964D.

The Site 964 spliced record can be used as a sampling guide to recover a single sedimentary sequence. The spliced record consists primarily of cores from Holes 964A and 964B. Several cores from Holes 964C, 964D, and 964E also were used to construct the sampling splice. Intervals with significant disturbance or distortion were avoided if possible. Normally, the composite depths are aligned so that tie points between adjacent holes occur at exactly the same mcd. However, at Site 964, many cores were cut by faults and had sections missing within the core relative to cores in adjacent holes. Incorporating these missing sections within the splice resulted in a splice record that is longer than the composite depth record. The tie points for the splice are given in Table 7.

All raw data tables of MST and reflectance, as well as a spliced color reflectance table for 550 nm, are on the CD-ROM (back pocket).

INORGANIC GEOCHEMISTRY

Interstitial-water samples were obtained at Site 964 from 1.45 to 94.90 mbsf, using the standard ODP titanium/stainless-steel squeezer (Manheim and Sayles, 1974). In total, eight samples were squeezed (Table 8), and the retrieved pore waters were subsequently analyzed for salinity, alkalinity, chloride, sulfate, bromide, lithium, potassium, rubidium, sodium, calcium, magnesium, strontium, ammonium, and silica using the methods described in the "Explanatory Notes" chapter (this volume).

Organic Matter Degradation

Degradation of sedimentary organic matter affects the pore-water composition at Site 964 to a much lesser extent than at Site 963, in accordance with the much lower sedimentation rates at this site (see "Lithostratigraphy" section, this chapter). The average sedimentation rate is approximately fivefold smaller at Site 964 than it is at Site 963, and accordingly the ammonium pore-water concentration is much lower (Fig. 30). In contrast to Site 963, appreciable sulfate reduction (Fig. 30), or methane generation (see "Organic Geochemistry" section, this chapter), does not seem to take place at Site 964. Based on

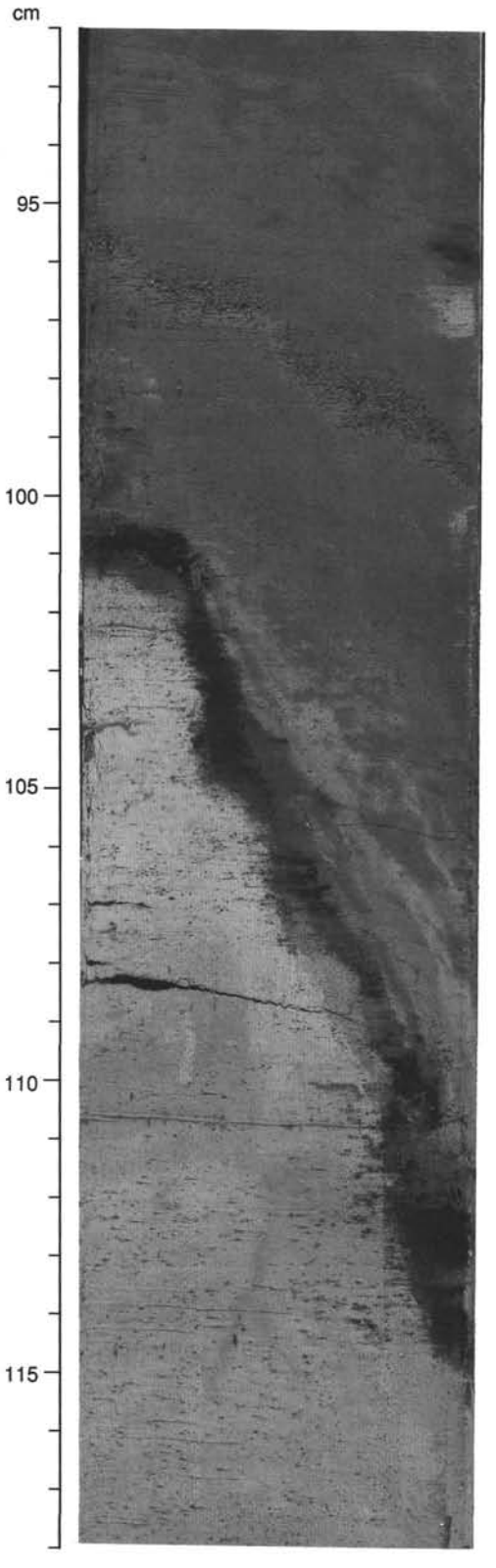

Figure 24. Irregular normal fault at Section 964B-4H-2, 92–118 cm, reflecting the involvement of a sapropel and its clay-rich surrounding sediments in a shear zone. Distinct low-angle kink bands and an anastomosing microfault occur just below the shear zone.

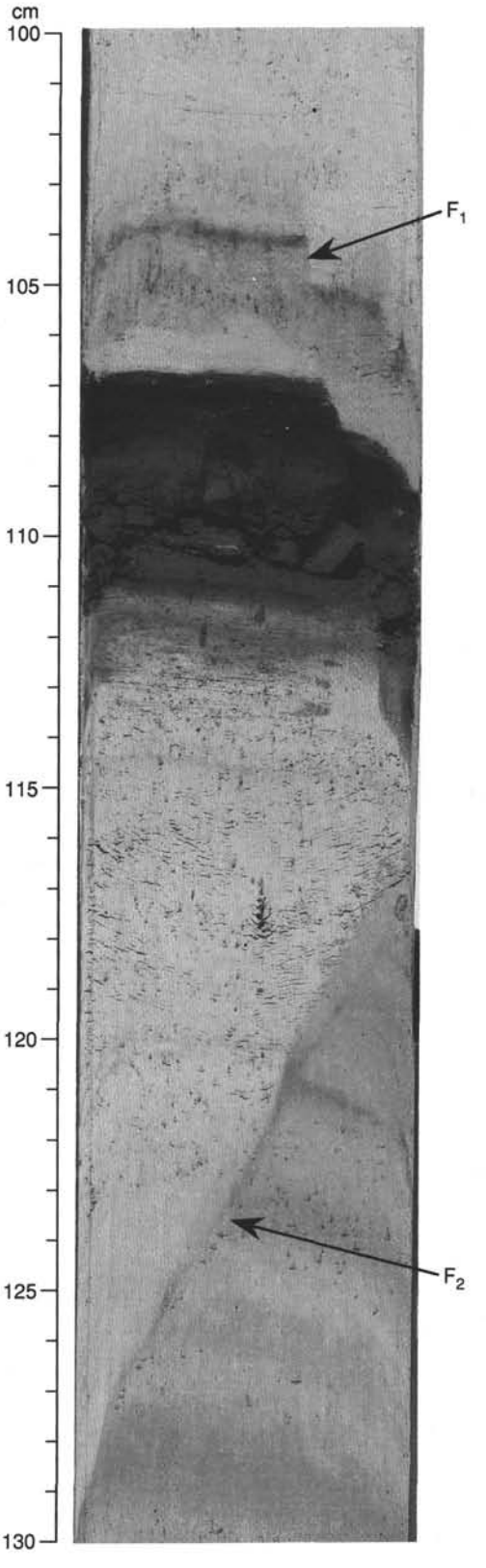

Figure 25. Two high-angle faults in Section 160-964A-7H-4, 100–130 cm. F_1, which has a small normal offset and cuts a sapropel, is difficult to trace across the entire core face. F_2 shows a fault for which it is not possible to determine either the offset or the sense of movement.

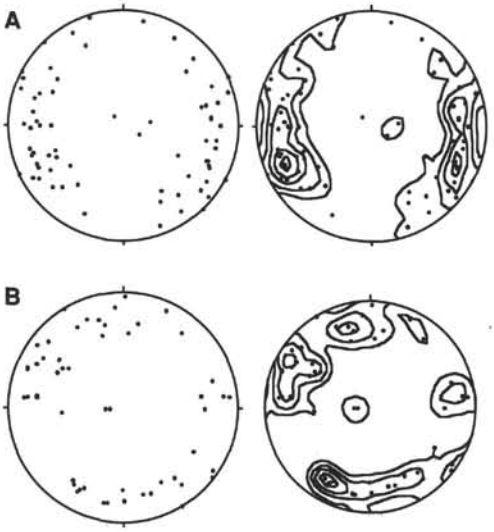

Figure 26. **A.** Poles to fault planes determined from the cores of Holes 964A and 964D. **B.** Poles to faults corrected using Tensor data in Holes 964A and 964D. Data presented both as single measurements and contoured.

the ammonium and alkalinity profiles, organic matter degradation seems to be most pronounced in the upper 5 m (Fig. 30).

The release of ammonium during the decomposition of organic matter in the top 5 m induces ion exchange reactions resulting in the uptake of some ammonium and a concomitant release of lithium. These reactions result in a small increase in the concentration of lithium in the pore water at this interval (Fig. 30). The increase in lithium and the decrease in alkalinity below 25 mbsf are discussed below.

Carbonate Diagenesis

The pore-water profile indicates alkalinity consumption that may result from the precipitation of a carbonate phase or intense alteration of volcanogenic material below a depth of 40 mbsf. Because the abundance of ash layers does not increase with depth (see "Lithostratigraphy" section, this chapter), the latter process cannot be of importance (see also below). Assuming a Redfield C/N ratio of 6.6 for the decomposition of organic matter, we have calculated the expected alkalinity from the ammonium pore-water profile (Fig. 30). It should be noted that we have not made corrections for different diffusivities of bicarbonate and ammonium, nor have we adapted the Redfield C/N ratio to an apparent "Mediterranean sedimentary C/N value" (see "Inorganic Geochemistry" section, "Site 963" chapter, this volume). On the basis of the difference between the calculated and observed alkalinity values, we can state that at most 1.5 mM of carbonate precipitation may have occurred. The slight decrease of pH with depth is in agreement with such precipitation (Fig. 31). Methane-induced sulfate reduction does not seem to contribute to the buildup of an "apparent alkalinity pool," as there is no indication that methane production is of any significance at Site 964 (see "Organic Geochemistry" section, this chapter). The calculated amount of Ca/Mg carbonate precipitation is negligible compared to the observed increases in dissolved calcium, strontium, and magnesium concentrations in the lower part of this site (Fig. 31). These increases seem to be related to elevated salinity values (see below).

Salinity, Chloride, Potassium, Rubidium, and Reactive Silica

Salinity and chloride concentrations increase from a typical Mediterranean bottom-water value of about 610 mM to values that are 17% higher at 100 mbsf (Fig. 32). This magnitude of change is not seen in the sulfate profile, which remains fairly constant with depth (Fig. 30). The increase in chloride is accompanied by increases in magnesium, calcium, strontium, bromide, sodium, lithium, potassium, and rubidium (Figs. 30–33). Usually, a gradual decrease occurs in the potassium and rubidium concentrations vs. depth in marine sediments (see "Inorganic Geochemistry" section, "Site 963" chapter, this volume). Similar uptake reactions most likely take place at Site 964 (Fig. 33). The slightly lower potassium and rubidium concentrations relative to chloride in the upper 60 m support this view. However, this process is masked by a major upward flux of potassium from a deeper source in the sediments.

The silica pore-water profile demonstrates minor variations with depth (i.e., between 140 and 200 µM; Fig. 33). Consequently, no appreciable amounts of amorphous silica seem present (see "Inorganic Chemistry" section, "Site 963" chapter, this volume).

Table 6. Site 964 composite depth section.

Core	Depth (mbsf)	Offset (m)	Depth (mcd)
160-964A-			
1H	0.00	0.00	0.00
2H	6.8	–0.38	6.42
3H	16.3	–0.31	15.99
4H	25.8	0.68	26.48
5H	45.3	1.41	36.71
6H	44.8	2.47	47.27
7H	54.3	3.61	57.91
8H	63.80	4.87	68.67
9H	73.30	13.14	86.44
10H	82.8	12.50	95.30
11H	92.30	12.97	105.27
160-964B-			
1H	0.00	0.06	0.06
2H	8.10	0.50	8.60
3H	17.60	0.90	18.50
4H	27.10	2.64	29.74
5H	36.60	3.63	40.23
6H	46.10	4.49	50.59
7H	55.60	5.79	61.39
8H	65.10	7.80	72.90
9H	74.60	7.80	82.40
10H	84.10	10.41	94.51
11H	93.60	10.50	104.10
160-964C-			
1H	0.00	0.04	0.04
2H	5.10	3.04	8.14
3H	14.60	3.75	18.35
4H	24.10	5.85	29.95
5H	33.60	6.98	40.58
6H	43.10	8.51	51.61
7H	52.60	9.04	61.64
8H	62.10	8.62	70.72
9H	71.60	8.52	80.12
10H	81.10	13.57	94.67
11H	90.60	13.57	104.17
12X	95.60	13.57	109.17
160-964D-			
1H	0.00	0.06	0.06
2H	4.10	2.86	6.96
3H	13.60	2.75	16.35
4H	23.10	1.54	24.64
5H	32.60	5.59	38.19
6H	42.10	6.37	48.47
7H	51.60	7.11	58.71
8H	61.10	8.34	69.44
9H	70.60	10.32	80.92
10H	80.10	10.29	90.39
11H	89.60	14.17	103.77
12H	99.10	15.59	114.69
160-964E-			
1H	0.00	0.37	0.37
2H	5.50	5.86	11.36
3H	15.00	3.66	18.66
4H	57.00	8.18	65.18
5H	66.50	10.36	76.86
6H	76.00	10.47	86.47
160-964F-			
1H	0.00	0.41	0.41
2H	9.10	1.52	10.62
3H	18.60	2.04	20.64

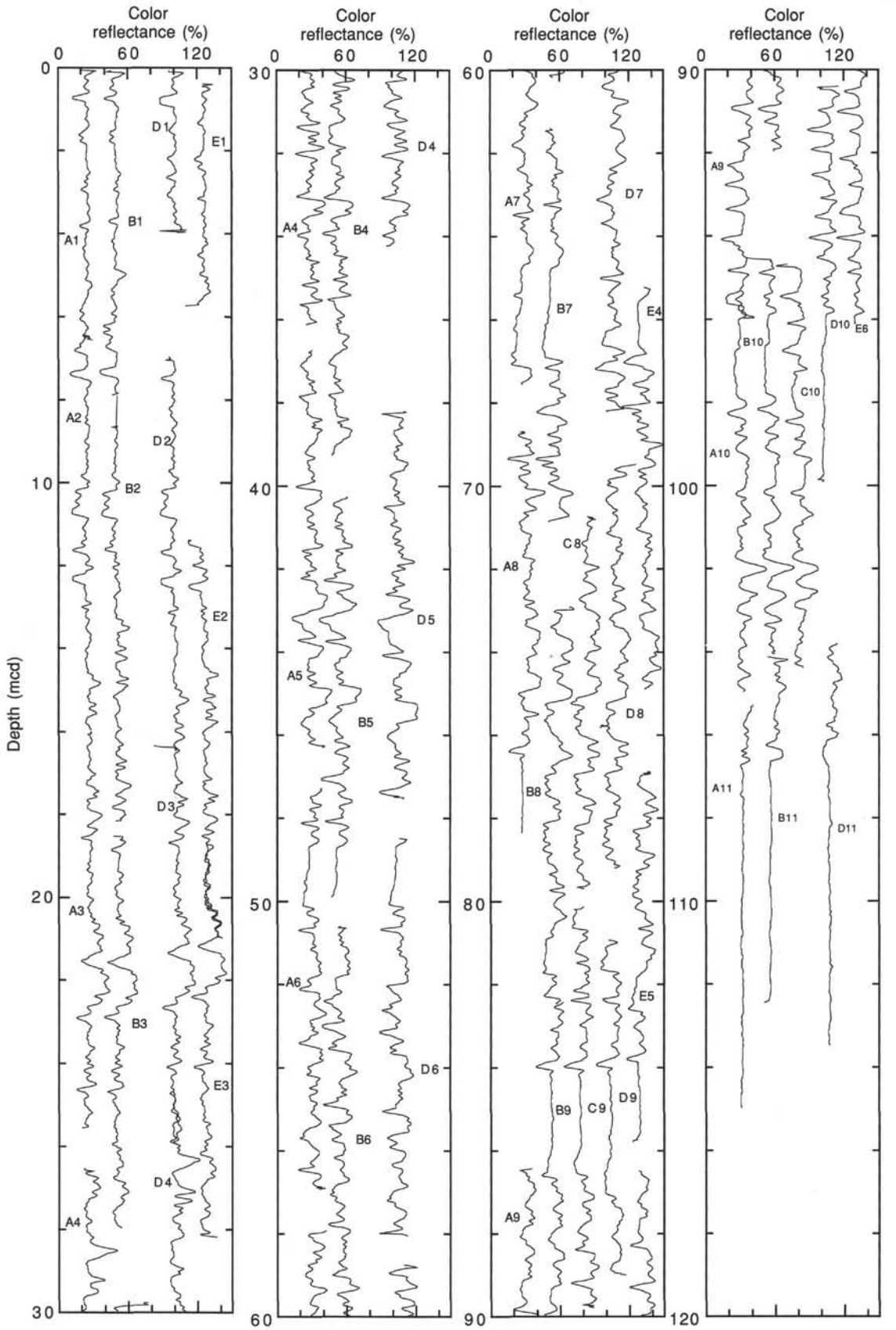

Figure 27. Percent color reflectance (550-nm wavelength) from Site 964 on the composite depth scale. Holes 964A through 964E are offset from each other by a constant (25 instrument units). Cores for each hole are shown (e.g., B3 = Core 160-964B-3H).

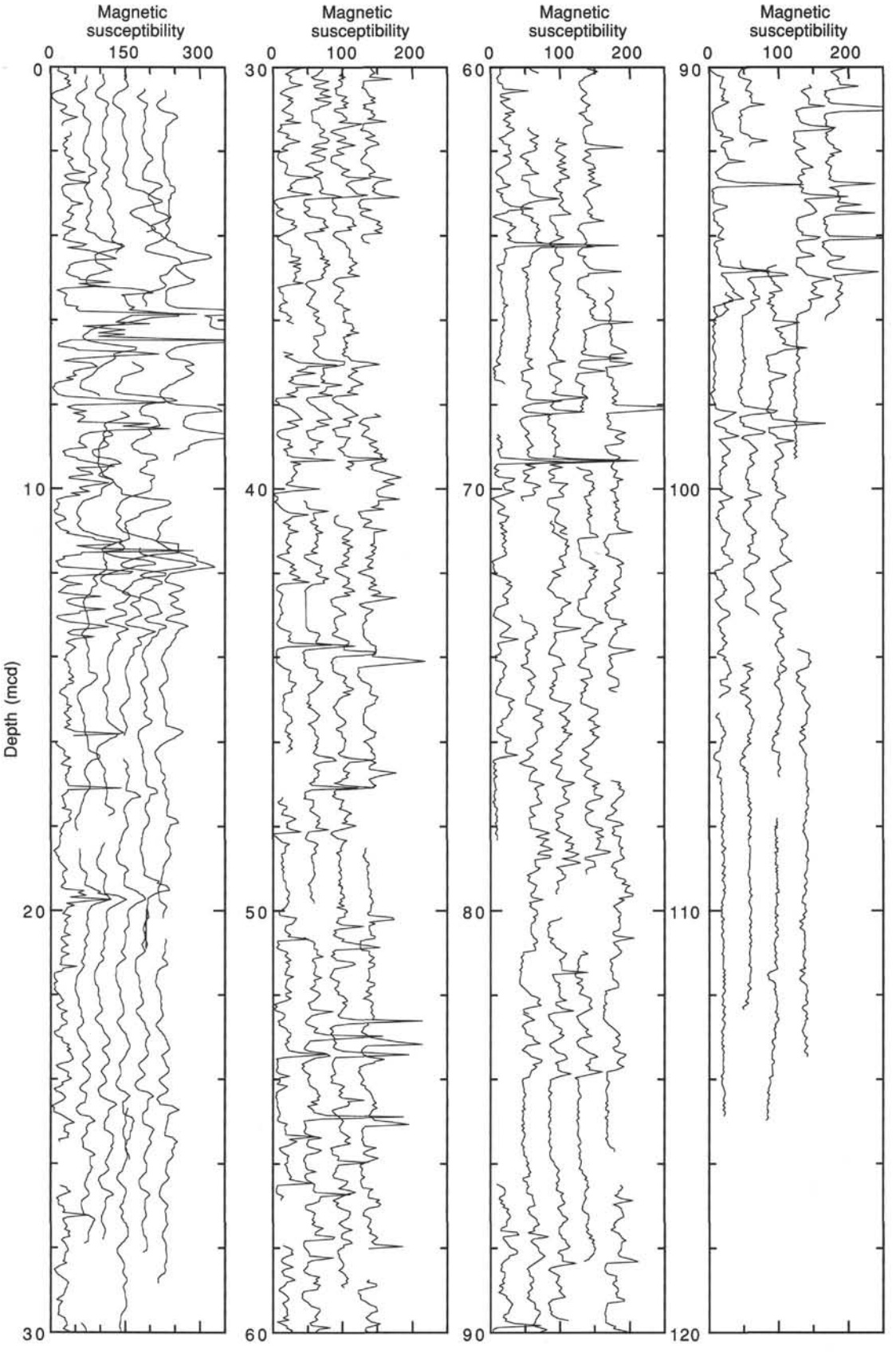

Figure 28. Magnetic susceptibility data (uncorrected instrument units) from Site 964 on the composite depth scale. Holes 964A through 964F are offset from each other by a constant (40 instrument units). Note the different magnetic susceptibility scale for 0–30 mcd.

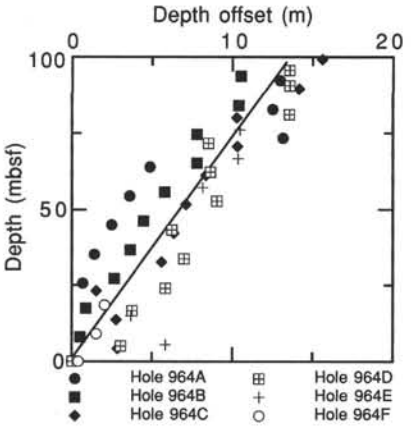

Figure 29. Depth offsets from composite construction relative to mbsf depth indicate "growth" of the composite depth scale with increasing depth.

The large increases that occur in the calcium and magnesium pore-water concentrations are unrelated to interaction with volcanic (ash) layers (Gieskes, 1983). Although ash layers do occur at this site at certain intervals (see "Lithostratigraphy" section, this chapter), their influence on the pore-water chemistry is negligible and a negative correlation between calcium and magnesium concentrations is not seen. Therefore, as at Site 963, the alteration of ash layers seems of minor importance for the alkaline earth element pore-water profiles. In the absence of measurable sulfate reduction and of interaction with volcanic ashes, the increases with depth of calcium, magnesium, and strontium seem determined mostly by upward fluxes related to evaporites.

Evaporite-related Fluxes

In the lower part of Site 964, distinct increases are observed in the concentrations of chloride, sodium, calcium, strontium, magnesium, bromide, and lithium. The relatively large increases especially of lithium and bromide point to the presence of a late-stage evaporite brine at some depth below this site. It is difficult to speculate on the exact origin and depth of such a source, owing to the relatively shallow penetration in the sediments at this site. Extrapolation using an advective diffusion model is therefore highly speculative. Based on the rather limited data set, and assuming similar sediment settings below the recovered intervals, a best possible estimate of 300–800 mbsf can be given for the inferred uppermost limit of brine/evaporite occurrence (see McDuff et al., 1978).

However, based on an extrapolation of the three lowermost pore-water samples to a chloride concentration of 5000 mM and a bromide content of 35 mM (typical late-stage evaporite brine values), it is possible to estimate the chemical composition of the evaporite brine source located in the sediments below this site (see Table 9, Fig. 34). Both extrapolations lead to comparable results and point toward a late-stage evaporite brine with high concentrations of lithium, strontium, calcium, and bromide. Although strontium and calcium may also originate from brine interaction with carbonates, lithium and bromide are predominantly of evaporitic origin.

ORGANIC GEOCHEMISTRY

Volatile Hydrocarbons

As part of the shipboard safety and pollution-prevention monitoring program, hydrocarbon gases were analyzed in each core of Hole 964A by the headspace technique. Only trace concentrations of methane in the range of 2 to 4 ppm were recorded.

Table 7. Site 964 splice tie points.

Hole, core, section, interval (cm)	Depth (mbsf)	Depth (mcd)		Hole, core, section, interval (cm)	Depth (mbsf)	Depth (mcd)
964A-1H-4, 130.0	5.80	5.80	ties to	964B-1H-4, 76.0	5.26	5.80
964B-1H-5, 126.0	7.26	7.80	ties to	964A-2H-1, 98.0	7.78	7.80
964A-2H-6, 126.0	15.56	15.58	ties to	964B-2H-4, 68.0	13.28	15.58
964B-2H-6, 2.0	15.62	17.92	ties to	964A-3H-1, 84.0	17.14	17.92
964A-3H-6, 114.0	24.94	25.72	ties to	964B-3H-5, 16.0	23.76	25.72
964B-3H-7, 6.0	26.66	28.62	ties to	964D-4H-1, 106.0	24.16	28.62
964D-4H-6, 92.0	31.52	35.98	ties to	964B-4H-3, 32.0	30.42	35.98
964B-4H-6, 60.0	35.20	40.76	ties to	964A-5H-1, 116.0	36.46	40.76
964A-5H-7, 2.0	44.32	48.62	ties to	964B-5H-4, 96.0	42.06	48.62
964B-5H-6, 92.0	45.02	51.58	ties to	964D-6H-1, 12.0	42.22	51.58
964D-6H-6, 122.0	50.82	60.18	ties to	964B-6H-5, 48.0	52.58	60.18
964B-6H-6, 78.0	54.38	61.98	ties to	964D-7H-1, 12.0	51.72	61.98
964D-7H-2, 10.0	53.20	63.46	ties to	964A-7H-1, 98.0	55.28	63.46
964A-7H-3, 96.0	58.26	66.44	ties to	964D-7H-3, 148.0	56.08	66.44
964D-7H-5, 42.0	58.02	68.38	ties to	964B-7H-2, 46.0	57.56	68.38
964B-7H-5, 110.0	62.70	73.52	ties to	964E-4H-2, 62.0	59.12	73.52
964E-4H-6, 54.0	65.04	79.44	ties to	964C-8H-2, 50.0	64.10	79.44
964C-8H-5, 28.0	68.38	83.72	ties to	964E-5H-1, 146.0	67.96	83.72
964E-5H-4, 122.0	72.22	87.98	ties to	964C-9H-1, 48.0	72.08	87.98
964C-9H-6, 78.0	79.88	95.78	ties to	964E-6H-2, 32.0	77.82	95.78
964E-6H-6, 90.0	84.40	102.36	ties to	964B-10H-1, 38.0	84.48	102.36
964B-10H-6, 42.0	92.02	109.90	ties to	964A-10H-5, 110.0	89.90	109.90
964A-10H-6, 134.0	91.64	111.64	ties to	964D-11H-1, 18.0	89.78	111.64

Carbonate and Organic Carbon

The abundance of total, inorganic, and organic carbon and of calcium carbonate in sediments from Hole 964A is summarized in Table 10. Random sampling was performed for carbonate analysis. For organic matter assessment, samples were specifically taken from the sapropels.

Carbonate contents are extremely low in most of the sapropels below 30 mbsf (Fig. 35). The occurrence of higher carbonate contents in this interval (i.e., between about 55 and 78 mbsf) results from burrowing and related transfer of overlying carbonate-rich sediment into a sapropel. Shallow sapropels cannot be distinguished from the surrounding sediment on the basis of carbonate content. In general, carbonate contents are high, but variable (Fig. 35). There is a tendency for slightly higher carbonate enrichment in the lower part of the profile drilled at Hole 964A (below 30 mbsf). The highest values approach 80%.

Organic carbon was determined only for a few samples outside the sapropels; the low values obtained confirmed a visual impression (light colored, usually yellowish or brownish) of organic-matter-poor background sediment (Table 10). In contrast to this, all sapropels (at least those that do not grade into the background sediment) contain more than 2% organic carbon; in several of them the concentration exceeds 20%, with a maximum at 24.6% (Table 10, Fig. 35).

Organic Matter Type: C_{org}/N Ratios, Rock-Eval Pyrolysis, and Pyrolysis-gas Chromatography

The C_{org}/N ratios for all sapropels exceed a value of 10 (Table 10; note that ratios were not calculated in intervals with organic carbon contents below 1% because of possible interference with inorganic nitrogen and experimental limitations of precisely determining small absolute quantities of nitrogen). The ratios are between 10 and 15 in the carbonate-rich sapropels within the upper part of the sequence and generally between 15 and 22 in the deeper, carbonate-poor sapropels. According to commonly accepted lines of interpretation (e.g., Emerson and Hedges, 1988), these values indicate that a major proportion of organic matter in the shallower sapropels is terrigenous and that the organic matter in the deeper ones is almost entirely terrigenous. However, this is not in accordance with the results of Rock-Eval pyrolysis (Table 11), which show hydrogen indices for many samples that exceed 400 and some that exceed 500, particularly in the deeper cores of Hole 964A where C_{org}/N values are greater than 15. Consistent with the relationship between organic matter type and el-

Table 8. Results of pore-water analyses for Site 964.

Core, section, interval (cm)	pH	Alkalinity (meq/L)	Salinity (g/kg)	Cl^- (mM)	Mg^{2+} (mM)	Ca^{2+} (mM)	SO_4^{2-} (mM)	NH_4^+ (μM)	SiO_2 (μM)	K^+ (mM)	Br^- (mM)	Sr^{2+} (μM)	Li^+ (μM)	Na^+ (mM)
160-964A-														
2H-5, 145–150	7.50	3.110	38.0	609.00	58.7	12.3	29.11	167	138	11.5	1.1	142	41	530
3H-6, 145–150	7.31	3.200	39.0	616.00	58.2	13.5	28.95	178	161	11.8	1.2	193	43	528
6H-5, 145–150	7.46	3.320	40.0	640.00	60.4	17.1	28.91	253	164	11.8	1.5	347	82	538
9H-4, 140–150	7.25	2.159	42.0	691.00	68.8	23.3	26.32	359	163	13.0	1.8	505	133	562
11H-4, 140–150	7.18	1.707	46.0	729.00	79.5	31.9	28.90	397	205	13.5	2.2	590	164	571
160-964F-														
1H-1, 145–150	7.50	2.432	38.0	614.00	58.8	11.6	31.30	32	137	12.1	1.0	107	34	542
1H-2, 145–150	7.34	2.903	38.0	613.00	58.5	11.8	30.60	66	149	11.8	1.0	120	35	528
1H-3, 145–150	7.41	2.985	38.0	610.00	58.5	11.8	30.70	102	153	12.0	1.0	133	43	528

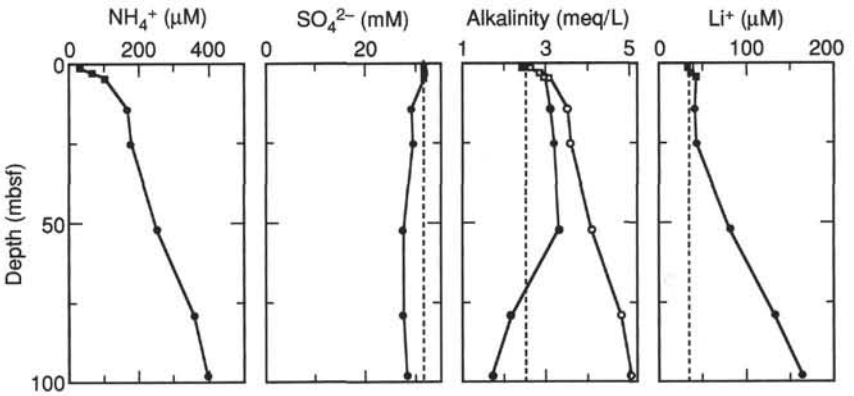

Figure 30. Pore-water vs. depth profiles from Holes 964A (circles) and 964F (squares) for ammonium, sulfate, alkalinity, and lithium. The dashed line indicates the bottom-water concentration. Measured values (solid circles) compared to calculated values (open circles) for alkalinity show that 1.5 mM of carbonate may have precipitated.

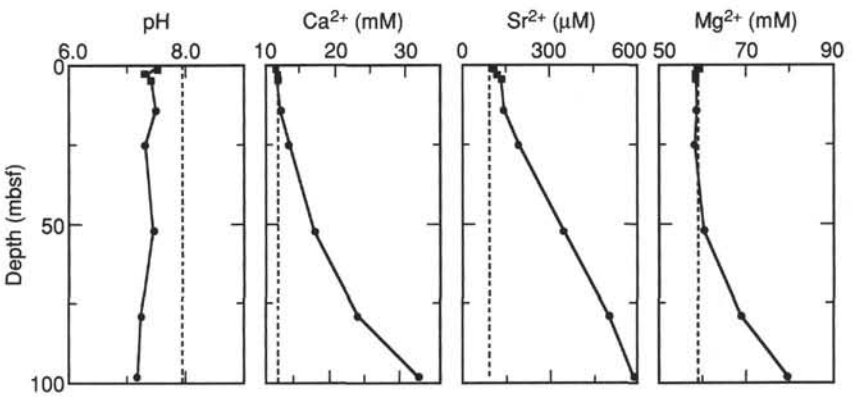

Figure 31. Pore-water vs. depth profiles from Holes 964A (circles) and 964F (squares) for pH, calcium, strontium, and magnesium. The dashed line indicates the bottom-water concentration.

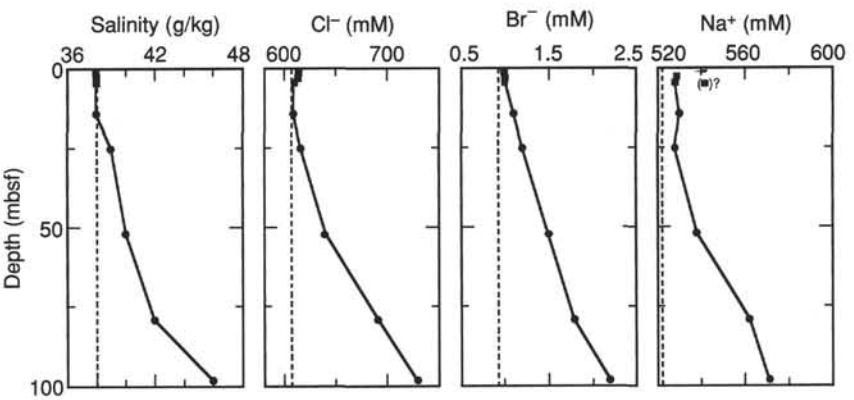

Figure 32. Pore-water vs. depth profiles from Holes 964A (circles) and 964F (squares) for salinity, chloride, bromide, and sodium. The dashed line indicates the bottom-water concentration. An anomalous sample value marked by parentheses and a question mark is not well understood at this time.

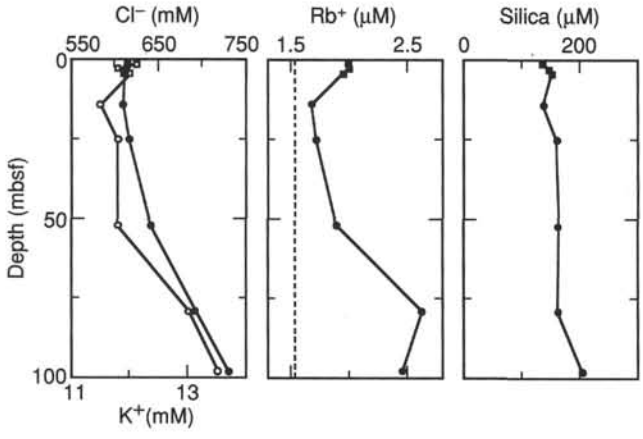

Figure 33. Pore-water vs. depth profiles from Holes 964A (circles) and 964F (squares) for potassium (solid symbols) and chloride (open symbols), rubidium, and reactive silica. The dashed line indicates the bottom-water concentration.

Table 9. Estimated chemical composition (mM/L) of the evaporative brine source located in sediments below Site 964.

Element	Extrapolated to 5000-mM Cl	Extrapolated to 35-mM Br
Na	2200	2100
Mg	1000	1000
Ca	700	700
K	96	90
Br	35	—
Sr	12	14
Li	4	4

emental composition, the oxygen indices show an opposite trend to the hydrogen indices and are high for the organic matter in the shallower sapropels and low in the deeper ones.

The hydrogen indices clearly indicate that none of the sapropels contains entirely unaltered, primary marine organic matter. In addition, there is microscopic evidence for woody higher plant material in the sapropels (see "Lithostratigraphy" section, this volume); this is corroborated by the occurrence of long-chain *n*-alkanes with an odd-to-even carbon number predominance in the extractable bitumen. These experimental results can at least partly explain the moderately high hydrogen indices and the high C_{org}/N ratios. Furthermore, diagenetic alteration must have caused effective removal of labile nitrogen-bearing organic compounds (e.g., amino acids), particularly from the organic matter of the more deeply buried sapropels. This may have occurred by benthic biological activity, as indicated by burrows extending into the sapropels; by microbial sulfate reducers, as suggested by the high amounts of reduced sulfur present (discussed below); by diffusion of molecular oxygen into the sapropels from the surface, which may have "burnt down" the upper parts of some sapropels; or by interaction with mineral-rich fluids.

Pyrolysis-gas chromatography using the Geofina Hydrocarbon Meter monitoring system clearly shows that sapropels in the deeper part of the sequence (below 30 mbsf) consist mainly of marine organic matter. This is inferred from the highly aliphatic nature of the pyrolysis products as expressed in an extended homologous series of *n*-alkane/*n*-alkene pairs that most likely are derived from the thermal decomposition of highly aliphatic biopolymers in fossilized algal cell walls (Fig. 36A). Although no standards were used for quantification, it is estimated from the amount of sediment material used for pyrolysis, organic carbon contents of the samples, and detector response

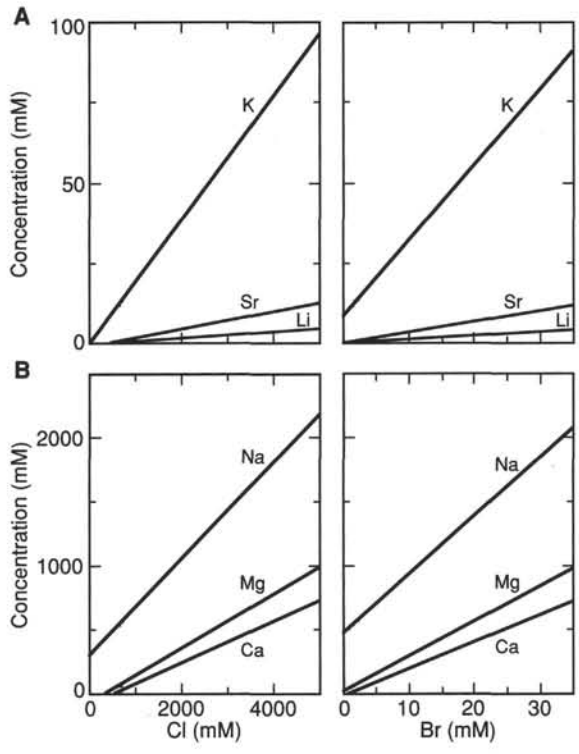

Figure 34. Extrapolation plots for potassium, strontium, and lithium (**A**) and sodium, magnesium, and calcium (**B**) vs. chloride and bromide.

that the average yield of alkanes/alkenes (per unit of organic carbon) from the deeper sapropels is higher than that from the shallower sapropels by at least a factor of 2 or 3. This *n*-alkane/*n*-alkene series is only a minor product in the pyrolysates of the shallow sapropels with moderately high organic carbon contents. The pyrolysates of these samples are more like those of lignin-type material (Fig. 36B) and, thus, would indicate the presence of a relatively higher amount of terrigenous organic matter in these sapropels.

Sulfur

The sulfur values reported in Table 10 are high for all sapropels, but the more deeply buried, carbonate-poor sapropels are particularly enriched. Here, values of 5%–10% are common, and a maximum of 18% sulfur was found in Section 160-964A-9H-6 (note that the sulfur data in Table 10 are representative of the high sulfur concentration values and their variations, but that calibration may be less accurate for values >5% than for lower values). Most of the sulfur is present as pyrite because pyrite concretions were visually detected in the sapropels and abundant disseminated pyrite was observed under the microscope. There is no obvious relationship between organic carbon and sulfur content.

Extractable Bitumen: Assessment of Paleotemperatures

Forty-three sapropel samples were extracted and filtered over a short column filled with aluminum oxide. Terrigenous long-chain *n*-alkanes with odd-to-even carbon number predominance and long-chain alkenones of Prymesiophyte origin were the only compounds that could be identified directly from the complex mixtures in the capillary column gas chromatograms of nonpolar bitumens.

Long-chain alkenones are moderately to highly abundant in all sapropel extracts, so that ratios of di- and triunsaturated C_{37} alkenones (U^k_{37} index) could be determined for a first approximation of paleo-

Table 10. Concentration of total, inorganic, and organic carbon, calcium carbonate, total nitrogen, and sulfur in sediments from Hole 964A.

Core, section, interval (cm)	Depth (mbsf)	Total carbon (%)	Inorganic carbon (%)	Organic carbon (%)	$CaCO_3$ (%)	Nitrogen (%)	Sulfur (%)	C_{org}/N	C_{org}/S
160-964A-									
1H-1, 1–2	0.01		5.22		43.48				
1H-1, 10–11	0.10		7.64		63.64				
1H-1, 55–56	0.55		5.52		45.98				
1H-1, 70–71	0.70	7.60	4.46	3.14	37.15	0.30	1.73	10.5	1.8
1H-1, 120–121	1.20		3.59		29.90				
1H-3, 33–34	3.33		4.29		35.74				
2H-1, 73–74	7.53		3.79		31.57				
2H-1, 94–95	7.74	9.07	3.29	5.78	27.41	0.42	2.18	13.8	2.7
2H-1, 103–104	7.83	6.40	3.53	2.87	29.40	0.27	2.15	10.6	1.3
2H-3, 122–123	11.02	8.06	4.56	3.50	37.98	0.27	2.99	13.0	1.2
2H-3, 130–131	11.10	7.00	4.03	2.97	33.57	0.20	3.36	14.9	0.9
2H-4, 43–44	11.73		2.61		21.74				
2H-4, 69–70	11.99	8.82	1.52	7.30	12.66	0.47	3.93	15.5	1.9
2H-4, 73–74	12.03	7.58	4.01	3.57	33.40	0.28	4.89	12.8	0.7
2H-4, 133–134	12.63	6.93	3.78	3.15	31.49	0.25	2.29	12.6	1.4
2H-4, 143–144	12.73	6.66	4.48	2.18	37.32	0.15	1.98	14.5	1.1
2H-5, 9–10	12.89		3.44		28.66				
3H-2, 80–81	18.60		2.01		16.74				
3H-2, 108–109	18.88	6.87	4.44	2.43	36.99	0.21	2.73	11.6	0.9
3H-4, 104–105	21.84	8.68	5.59	3.09	46.56	0.22	6.01	14.0	0.5
3H-5, 56–57	22.86		6.67		55.56				
3H-5, 92–93	23.22	8.40	5.81	2.59	48.40	0.21	2.36	12.3	1.1
3H-6, 40–41	24.20		4.44		36.99				
3H-6, 113–114	24.93	9.65	4.09	5.56	34.07	0.33	1.97	16.8	2.8
4H-4, 38–39	30.68	10.23	5.28	4.95	43.98	0.35	3.24	14.1	1.5
4H-4, 73–74	31.03		7.81		65.06				
4H-4, 103–104	31.33	10.99	6.74	4.25	56.14	0.29	1.66	14.7	2.6
4H-5, 30–31	32.10		5.67		47.23				
4H-5, 56–57	32.36	16.66	0.28	16.38	2.33	0.86	3.94	19.0	4.2
4H-5, 70–71	32.50		7.73		64.39				
4H-6, 2–3	33.32	11.53	7.18	4.35	59.81	0.29	1.62	15.0	2.7
4H-6, 116–117	34.46		0.84		7.00				
4H-7, 16–17	34.96	7.91	5.22	2.69	43.48	0.26	2.29	10.3	1.2
4H-7, 40–41	35.20		5.22		43.48				
5H-1, 108–109	36.38		7.84		65.31				
5H-1, 114–115	36.44	10.87	6.91	3.96	57.56	0.29	1.25	13.7	3.2
5H-1, 133–134	36.63		5.17		43.07				
5H-2, 95–96	37.75		6.18		51.48				
5H-3, 25–27	38.55	5.16	4.95	0.21	41.23	0.03	0.26		
5H-3, 27–29	38.57	1.91	1.74	0.17	14.49	0.07	0.20		
5H-3, 29–30	38.59	13.42	0.20	13.22	1.67	0.74	2.34	17.9	5.6
5H-3, 30–31	38.60	18.37	0.16	18.21	1.33	0.94	4.46	19.4	4.1
5H-3, 31–32	38.61	14.63	0.41	14.22	3.42	0.74	4.67	19.2	3.0
5H-3, 32–33	38.62	13.96	1.52	12.44	12.66	0.69	4.70	18.0	2.6
5H-3, 33–34	38.63	17.41	0.22	17.19	1.83	0.90	5.80	19.1	3.0
5H-3, 34–35	38.64	8.66	5.11	3.55	42.57	0.29	3.01	12.2	1.2
5H-3, 35–37	38.65	8.35	8.03	0.32	66.89	0.04	0.54		
5H-3, 37–39	38.67	7.95	7.74	0.21	64.47	0.03	0.48		
5H-4, 25–26	40.05		7.48		62.31				
5H-4, 36–37	40.16		8.03		66.89				
5H-4, 102–103	40.82	13.57	0.46	13.11	3.83	0.75	4.19	17.5	3.1
5H-4, 104–105	40.84	2.56	2.19	0.37	18.24	0.07	0.37		
5H-4, 113–114	40.93	5.46	5.37	0.09	44.73	0.03			
5H-5, 34–35	41.64		4.80		39.98				
5H-5, 46–47	41.76	7.67	4.15	3.52	34.57	0.31	2.57	11.4	1.4
5H-5, 54–55	41.84		4.85		40.40				
5H-5, 66–67	41.96		4.23		35.24				
5H-5, 100–101	42.30	20.37	0.27	20.10	2.25	0.93	8.70	21.6	2.3
5H-5, 110–111	42.40	3.81	3.71	0.10	30.90	0.03	0.85		
5H-5, 120–121	42.50		8.21		68.39				
6H-1, 70–71	45.50		6.29		52.40				
6H-1, 84–85	45.64	0.74	0.55	0.19	4.58	0.04	0.29		
6H-1, 86–87	45.66	11.05	3.69	7.36	30.74	0.44	4.88	16.7	1.5
6H-1, 87–88	45.67	9.00	7.02	1.98	58.48	0.15	2.54	13.2	0.8
6H-1, 90–91	45.70		8.29		69.06				
6H-2, 70–71	47.00		7.47		62.23				
6H-3, 41–42	48.21	16.92	0.66	16.26	5.50	0.87	7.47	18.7	2.2
6H-3, 44–45	48.24	8.36	6.11	2.25	50.90	0.15	4.58	15.0	0.5
6H-3, 50–51	48.30		6.89		57.39				
6H-4, 27–28	49.57		7.06		58.81				
6H-4, 32–33	49.62	11.79	0.50	11.29	4.17	0.63	8.89	17.9	1.3
6H-4, 34–35	49.64	3.15	3.07	0.08	25.57	0.04	2.88		
6H-4, 38–39	49.68	11.60	4.49	7.11	37.40	0.42	8.00	16.9	0.9
6H-4, 43–44	49.73		7.92		65.97				
6H-5, 14–15	50.94	24.62	0.28	24.34	2.33	1.18	7.85	20.6	3.1
6H-5, 110–111	51.90		6.34		52.81				
6H-6, 75–76	53.05		3.73		31.07				
6H-6, 83–84	53.13	14.01	4.73	9.28	39.40	0.46	6.10	20.2	1.5
6H-6, 106–107	53.36		3.73		31.07				
6H-7, 8–9	53.88		7.61		63.39				
6H-7, 18–19	53.98	19.01	0.32	18.69	2.67	0.92	9.80	20.3	1.9
6H-7, 24–25	54.04		8.34		69.47				
7H-1, 50–51	54.80		8.27		68.89				
7H-1, 110–111	55.40	7.42	7.25	0.17	60.39	0.01	0.32		
7H-2, 50–51	56.30		7.82		65.14				
7H-2, 110–111	56.90		8.36		69.64				
7H-3, 84–85	58.14	6.33	6.00	0.33	49.98	0.03	0.55		

Table 10 (continued).

Core, section, interval (cm)	Depth (mbsf)	Total carbon (%)	Inorganic carbon (%)	Organic carbon (%)	$CaCO_3$ (%)	Nitrogen (%)	Sulfur (%)	C_{org}/N	C_{org}/S
7H-3, 92–93	58.22	7.05	6.88	0.17	57.31	0.01	0.61		
7H-3, 96–97	58.26		4.24		35.32				
7H-4, 85–86	59.65		7.28		60.64				
7H-4, 99–100	59.79		7.93		66.06				
7H-4, 107–108	59.87	12.40	3.56	8.84	29.65	0.48	5.48	18.4	1.6
7H-4, 116–117	59.96		9.03		75.22				
7H-4, 133–134	60.13		6.30		52.48				
7H-5, 51–52	60.81		8.06		67.14				
7H-5, 110–111	61.40		7.24		60.31				
7H-6, 30–31	62.10		7.66		63.81				
7H-7, 18–19	63.48	8.94	6.56	2.38	54.64	0.16	5.04	14.9	0.5
8H-1, 63–64	64.43		7.38		61.48				
8H-1, 69–70	64.49	14.33	3.19	11.14	26.57	0.59	8.69	18.9	1.3
8H-1, 77–78	64.57		5.34		44.48				
8H-1, 93–94	64.73		4.25		35.40				
8H-2, 40–41	65.70		9.43		78.55				
8H-2, 70–71	66.00		7.35		61.23				
8H-3, 130–131	68.10		8.21		68.39				
8H-4, 80–81	69.10		8.93		74.39				
8H-5, 60–61	70.40		6.37		53.06				
8H-5, 110–111	70.90		6.92		57.64				
8H-6, 17–18	71.47	3.01	2.67	0.34	22.24	0.04	0.21		
8H-6, 22–23	71.52	11.89	7.10	4.79	59.14	0.27	4.70	17.7	1.0
8H-6, 30–31	71.60		7.28		60.64				
8H-7, 30–31	73.10		7.59		63.22				
9H-2, 59–60	75.39		9.39		78.22				
9H-3, 29–30	76.59		8.18		68.14				
9H-3, 42–43	76.72	11.82	4.09	7.73	34.07	0.51	1.50	15.2	5.2
9H-3, 101–102	77.31		9.30		77.47				
9H-4, 60–61	78.40		8.53		71.05				
9H-5, 29–30	79.59	3.56	3.43	0.13	28.57	0.04	0.12		
9H-5, 25–26	79.55		6.14		51.15				
9H-5, 35–36	79.65	15.25	1.74	13.51	14.49	0.77	0.77	17.51	7.5
9H-5, 43–44	79.73		8.23		68.56				
9H-5, 83–84	80.13		7.18		59.81				
9H-5, 89–90	80.19	20.39	0.14	20.25	1.17	1.14	1.14	17.81	7.8
9H-5, 98–99	80.28		7.94		66.14				
9H-6, 7–8	80.87		6.80		56.64				
9H-6, 14–15	80.94	14.78	0.36	14.42	3.00	0.80	18.24	18.0	0.8
9H-6, 18–19	80.98	11.19	3.02	8.17	25.16	0.51	13.93	16.0	0.6
9H-6, 22–23	81.02		6.41		53.40				
9H-6, 71–72	81.51		7.64		63.64				
9H-7, 4–5	82.34	5.34	1.49	3.85	12.41	0.24	2.76	16.0	1.4
9H-7, 34–35	82.64		7.07		58.89				
9H-CC, 25–27	83.11	24.76	0.14	24.62	1.17	1.24	9.66	19.9	2.5
10H-1, 70–71	83.50		7.74		64.47				
10H-2, 30–31	84.60		9.23		76.89				
10H-2, 122–123	85.52		6.60		54.98				
10H-2, 145–146	85.75		2.90		24.16				
10H-3, 4–5	85.84		6.03		50.23				
10H-3, 30–31	86.10		6.51		54.23				
10H-4, 70–71	88.00		9.33		77.72				
10H-5, 20–21	89.00		7.96		66.31				
10H-5, 88–89	89.68		9.31		77.55				
10H-6, 70–71	91.00		7.46		62.14				
10H-7, 10–11	91.90		7.44		61.98				
11H-1, 70–71	93.00		7.76		64.64				
11H-1, 107–108	93.37		8.09		67.39				
11H-3, 70–71	96.00		7.76		64.64				
11H-5, 70–71	99.00		7.76		64.64				
11H-7, 40–41	101.70		7.82		65.14				

sea-surface temperatures based on the calibrations of Prahl and Wakeham (1987), Brassell (1993), and Sikes and Volkman (1993). All the extracts yielded similar temperature values. Although the ratios calculated from the gas chromatograms may provide a reasonable approximation of the relative temperature changes with age, mass spectrometric search for compounds possibly co-eluting with the alkenones (particularly with the $C_{37:3}$ ketone at low concentrations) is necessary to validate absolute temperatures. For this reason, absolute temperatures are not tabulated here. Figure 37 shows that sea-surface temperatures were highly variable during the Holocene and the late and middle Pleistocene, down to a depth of about 30 mbsf; they show a range of approximately 7°C between 17° and 24°C regardless of the calibration used. In the early Pleistocene (approximately 30–50 mbsf) and the Pliocene (below about 50 mbsf) temperatures gradually increased and were less variable. The alkenone sea-surface temperature pattern is generally in accordance with the results of previous geochemical studies on Mediterranean sapropels (ten Haven, 1986; ten Haven et al., 1987; K.C. Emeis, pers. comm., 1995) and the current understanding of climate development during the past few million years.

PHYSICAL PROPERTIES

Physical properties were measured in all cores obtained at Site 964. Measurements were conducted on all whole-round core sections, excluding core catchers, using the MST, which comprises the GRAPE, *P*-wave velocity logger, natural gamma-ray device, and magnetic susceptibility meter. Thermal conductivity was also measured in whole-core sections (see "Explanatory Notes" chapter, this volume, for technical details of these procedures). In addition, a detailed suite of physical property measurements was performed on

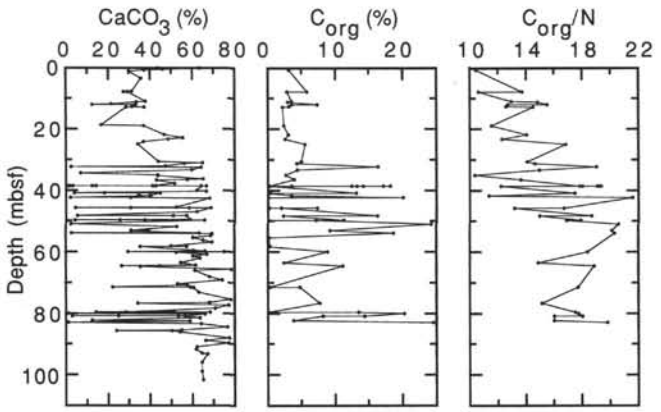

Figure 35. Concentrations of calcium carbonate and organic carbon and the ratio of organic carbon to total nitrogen in sediments at Hole 964A.

samples from two split sections of each core from Hole 964A; these measurements included dry- and wet-bulk density, grain density, porosity, water content, and void ratio. Vane shear strength and compressional wave velocities were measured in split core sections from Hole 964A as well. The results are listed in Tables 12 through 15 and are shown graphically in Figures 38 through 44. In this section, we describe the downhole distribution of selected physical properties of Hole 964A.

Index Properties

The measured index properties include measurements of mass and volume of selected sediment samples, from which water content, bulk and dry density, bulk and dry porosity, void ratio, and grain density were calculated (Table 12).

Measured wet-bulk density generally increases with depth (Fig. 38), owing to compaction and diagenesis. Bulk density values show an increase from approximately 1.7 to 1.9 g/cm^3. Water content, expressed relative to dry weight, varies from more than 40% just below the seafloor to less than 30% at depths exceeding 80 mbsf (Fig. 38).

GRAPE Density

GRAPE density (Fig. 39) shows an overall increase with depth in Hole 964A, and the rate of density increase seems constant, except between 60 and 95 mbsf, where the density is stable. The GRAPE data, from the seafloor down to 95 mbsf, are highly scattered. Below 95 mbsf, the scatter decreases significantly, concurrent with the sedimentary transition from alternating layers of calcareous oozes, volcanic ash, and sapropels to more homogeneous turbidites. A comparison of GRAPE density with the wet-bulk density index property shows general agreement between the two, although GRAPE density values are overall lower than index property bulk density. This is most likely because the GRAPE density was measured in undrained whole-round cores in their liners, which have a higher water content than discrete index properties samples taken from split cores.

Compressional Wave Velocities

Compressional wave velocity was measured parallel and normal (Table 13, Fig. 40A) to the core axis on split cores from Hole 964A using the digital sonic velocimeter system. Velocities generally increase with depth, from 1.50 km/s at the seafloor to 1.6 km/s at 60 mbsf, stabilize at about 1.62 km/s to 95 mbsf, and then increase again to 1.64 km/s. A similar trend of velocity variation was measured in the MST, although the precision of these measurements is affected by measuring through the core liner (Fig. 40B). The velocity patterns at Hole 964A are consistent with the measured index properties discussed above; in particular, the downhole distribution of porosity and water content is reflected in the velocity.

Shear Strength

Measurements of shear strength, using a mechanical vane, were made on split cores from Hole 964A, concurrent with the measurement of compressional wave velocity. Owing to a failure in the system, the results are reliable only to a depth of 45 mbsf. Values range from 5 to 260 kPa and generally increase with depth (Table 14, Fig. 41).

Magnetic Susceptibility

Figure 42 shows the distribution of magnetic susceptibility with depth for Hole 964A. The measurements, although scattered, seem to show a decrease in the magnetic susceptibility from the seafloor to 40 mbsf. Below 95 mbsf, magnetic susceptibility values show less scatter, confirming the sedimentary transition at 95 mbsf from alternating layers of calcareous oozes, sapropels, and volcanic ash to turbidites.

Natural Gamma-ray Radiation

NGR values decrease at a constant rate from about 30 to 20 counts per second (cps) (Fig. 43). The transition from the variable lithology of oozes, volcanic ashes, and sapropels to homogeneous turbidites is characterized by reduced scatter of the NGR values.

Thermal Conductivity

Thermal conductivity at Hole 964A was sampled in Sections 2 and 5 of each core. The measurements show an overall variation between approximately 1.0 and 1.4 W/(m · K) (Table 15, Fig. 44) and do not reflect the fine stratification pattern found in this borehole.

Relationship Between Physical Properties and Lithology

In general, Hole 964A shows two principal lithologies: a series of calcareous oozes from the seafloor to a depth of 95 mbsf is underlain by turbidites (see "Lithostratigraphy" section, this chapter). However, the oozes comprise alternating strata of sapropels and sporadic layers of volcanic ash. MST data are highly scattered at 0–95 mbsf, but less scattered below 95 mbsf, where the lithology changes from rhythmic layering to homogeneous turbidites. Physical properties measured at Hole 964A reflect compaction and diagenetic processes that took place at depths down to 95 mbsf. We suggest that compaction is the primary cause for the variation of the physical properties down to a depth of 50 mbsf (Figs. 38–41). A good correlation exists between *P*-wave velocity, shear strength, water content, and density.

SUMMARY AND CONCLUSIONS

Site 964 (36°15.63′N, 17°45.00′E, beneath 3657 m of water) is located at the foot of the Calabrian Ridge on a small bathymetric high. Here, an upper sedimentary unit of approximately 200 ms TWT overlies a strong seismic reflector that dips slightly to the northeast. The high is interpreted as being on the toe of the Calabrian accretionary prism near the Ionian Abyssal Plain. Based on piston-core information, the location was chosen to recover a Pliocene to Pleistocene sedimentary record of sapropel formation in the Ionian Basin. Our objectives were (1) to recover a deep-water sedimentary sequence that records the history of sapropel deposition in the Ionian Basin and the variations in deep-water formation from the Pliocene to the Holocene and (2) to establish a high-resolution stratigraphy based on pa-

Table 11. Results of Rock-Eval analysis for Hole 964A.

Core, section, interval (cm)	Depth (mbsf)	S_1 (mg/g)	S_2 (mg/g)	S_3 (mg/g)	TOC (%)	PC	HI	OI	T_{max} (°C)	PI	S_2/S_3
160-694A-											
1H-1, 70–71	0.70	1.39	5.98	4.98	3.14	0.61	190	158	413	0.19	1.20
2H-1, 94–95	7.74	2.48	14.99	7.06	5.78	1.45	259	122	415	0.14	2.12
2H-1, 103–104	7.83	1.15	4.55	4.55	2.87	0.47	158	158	403	0.20	1.00
2H-3, 122–123	11.02	1.49	7.38	5.35	3.50	0.73	210	152	412	0.17	1.38
2H-3, 130–131	11.10	1.50	5.91	5.02	2.97	0.61	198	169	403	0.20	1.18
2H-4, 69–70	11.99	6.41	22.64	6.71	7.30	2.42	310	91	408	0.22	3.37
2H-4, 73–74	12.03	2.12	8.55	5.05	3.57	0.88	239	141	407	0.20	1.69
2H-4, 133–134	12.63	1.40	7.22	4.27	3.15	0.71	229	135	415	0.16	1.69
2H-4, 143–144	12.73	0.64	3.00	3.79	2.18	0.30	137	173	412	0.18	0.79
3H-2, 108–109	18.88	0.78	4.33	3.95	2.43	0.42	178	162	413	0.15	1.10
3H-4, 104–105	21.84	1.35	9.29	4.11	3.00	0.88	309	137	418	0.13	2.26
3H-5, 92–93	23.22	0.89	5.62	3.69	2.59	0.54	216	142	419	0.14	1.52
3H-6, 113–114	24.93	2.97	18.87	5.79	5.56	1.82	339	104	420	0.14	3.26
4H-4, 38–39	30.68	2.02	13.68	4.30	4.95	1.30	276	86	427	0.13	3.18
4H-4, 103–104	31.33	1.85	10.59	3.96	4.25	1.03	249	93	428	0.15	2.67
4H-6, 2–3	33.32	3.21	13.50	3.77	4.35	1.39	310	86	420	0.19	3.58
4H-7, 16–17	34.96	1.24	6.20	2.82	2.69	0.62	230	104	418	0.17	2.19
5H-1, 114–115	36.44	1.44	8.73	3.83	3.90	0.84	223	98	419	0.14	2.27
5H-3, 29–30	38.59	8.50	49.51	6.21	13.22	4.83	374	46	428	0.15	7.97
5H-3, 30–31	38.60	14.66	65.48	7.71	18.21	6.67	359	42	424	0.18	8.49
5H-3, 31–32	38.61	13.89	53.45	5.83	14.22	5.61	375	40	409	0.21	9.16
5H-3, 32–33	38.62	9.66	44.81	6.65	12.44	4.53	360	53	428	0.18	6.73
5H-3, 33–34	38.63	13.93	63.99	7.46	17.19	6.49	372	43	424	0.18	8.57
5H-3, 34–35	38.64	1.14	6.98	3.44	3.55	0.67	196	96	422	0.14	2.02
5H-4, 102–103	40.82	7.52	48.42	6.16	13.11	4.66	369	46	432	0.13	7.86
5H-5, 100–101	42.30	18.47	71.34	7.50	20.10	7.48	354	37	414	0.21	9.51
6H-1, 86–87	45.66	4.91	28.56	4.87	7.36	2.78	388	66	415	0.15	5.86
6H-3, 41–42	48.21	11.08	68.34	7.25	16.26	6.61	420	44	417	0.14	9.42
6H-3, 44–45	48.24	0.89	5.48	2.47	2.25	0.53	243	109	409	0.14	2.21
6H-4, 32–33	49.62	8.31	47.63	5.11	11.29	4.66	421	45	415	0.15	9.32
6H-4, 38–39	49.68	3.65	27.43	4.75	7.11	2.59	385	66	417	0.12	5.77
6H-5, 14–15	50.94	27.28	126.83	8.46	24.30	12.84	521	34	419	0.18	14.99
6H-6, 83–84	53.13	7.16	47.57	5.59	9.28	4.56	512	60	419	0.13	8.50
6H-7, 18–19	53.98	20.12	88.85	6.91	18.69	9.08	475	36	415	0.18	12.85
7H-4, 107–108	59.87	6.85	42.37	5.15	8.84	4.10	479	58	415	0.14	8.22
7H-7, 18–19	63.48	0.87	6.86	2.15	2.38	0.64	288	90	421	0.11	3.19
8H-1, 69–70	64.49	10.92	52.74	5.15	11.14	5.30	473	46	418	0.17	10.24
8H-6, 22–23	71.52	2.68	20.70	3.14	4.79	1.94	432	65	421	0.11	6.59
9H-3, 42–43	76.72	3.03	27.33	4.57	7.30	2.53	374	62	417	0.10	5.98
9H-5, 35–36	79.65	7.43	49.27	5.98	13.51	4.72	364	44	418	0.13	8.23
9H-5, 89–90	80.19	14.54	83.89	7.51	20.20	8.20	415	37	418	0.15	11.17
9H-6, 14–15	80.94	8.84	61.80	5.86	14.42	5.88	428	40	418	0.13	10.54
9H-6, 18–19	80.98	3.05	24.35	4.88	8.17	2.28	298	59	415	0.11	4.98
9H-7, 4–5	82.34	1.04	10.74	3.08	3.85	0.98	278	80	426	0.09	3.48
9H-CC, 25–27	83.11	16.99	113.27	8.27	24.62	10.85	460	33	424	0.13	13.69

Notes: TOC = total organic carbon; PC = petroleum potential as pyrolyzable carbon; HI = hydrogen index; OI = oxygen index; PI = production index; see the "Explanatory Notes" chapter (this volume) for units for these parameters.

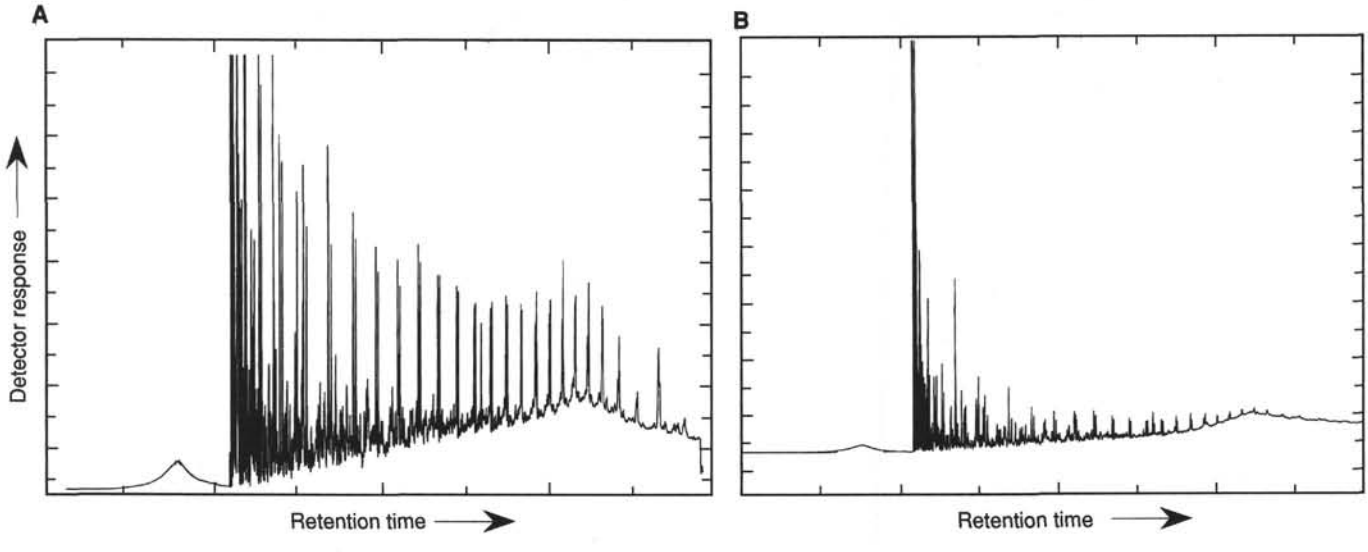

Figure 36. Pyrolysis-gas chromatograms of two sapropels from Hole 964A. **A.** Sample 160-964A-6H-5, 14–15 cm. **B.** Sample 160-964A-2H-4, 69–70 cm.

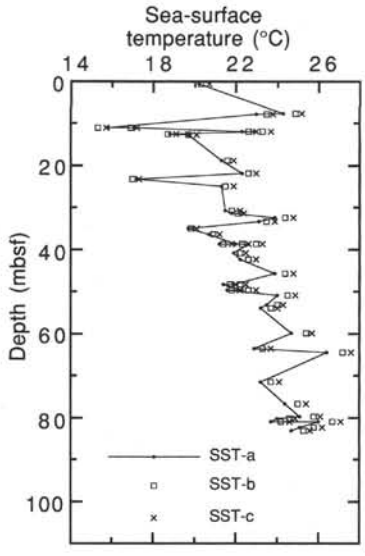

Figure 37. Variation of paleo-sea-surface temperature (SST) during times of sapropel deposition plotted against depth in Hole 964A. Temperatures were calculated from the alkenone unsaturation index (U^{k}_{37}) according to the calibrations of (a) Sikes and Volkman (1993), (b) Prahl and Wakeham (1987), and (c) Brassell (1993).

leontological, geochemical, magnetic, and lithologic properties and to correlate it with coeval sequences in Calabria.

Six holes were drilled at Site 964 to a maximum depth of 112 mbsf. Recovery and core quality in the APC cores and the sole XCB Core 160-964C-12X were excellent (average recovery 102%), and a complete sediment section was recovered that spans the lower Pliocene to the Holocene. Each hole contained locally discontinuous and tectonically attenuated sedimentary sequences. The striking sedimentological features and detailed records of physical properties (most notably color reflectance) of the sediment provided unambiguous markers that greatly facilitated correlation among the holes. High-resolution core logs were also used during operations on site to ascertain if a complete record had been recovered and to identify poorly constrained intervals to be cored again.

Outstanding features of the sequence recovered at Site 964 are the occurrence of more than 50 distinct sapropels in the composite section, the occurrence of numerous ash layers and ashy turbidites, and marked color banding of the sediments. The host sediments comprise light-colored (brownish to greenish) clayey nannofossil ooze, nannofossil ooze, and nannofossil clays. Some of the light-colored intervals are interpreted as normally graded turbidites (decimeters to meters thick). Limited intervals of foraminifer sand were recovered in the lower parts of the sequence. Tuffs are present as discrete beds, and volcanic glass is disseminated throughout. The sapropels, which are centimeters to decimeters thick, are enriched in pyrite, plant material, and amorphous organic matter. Individual sapropels display a wide range of depositional and postdepositional features that include laminations, bioturbation, and oxidation fronts (burn-down). Together, the sedimentological and physical features in the sapropels, ash layers, and turbidites permitted detailed correlation among the holes and the construction of complete sections despite erosional hiatuses at the bases of turbidites, high-angle extensional faults, and possible fault-like drilling artifacts.

Organic carbon concentrations in the sapropels reach up to 25 wt%, values that prior to Leg 160 were known only from Mesozoic black shales and sapropelic coals. Based on the amount of hydrocarbons liberated by pyrolysis, the organic matter is interpreted to be of mixed marine and terrigenous origin with a more strongly pronounced marine character in the older sapropels. High organic carbon concentrations are associated with high sulfur concentrations of up to 10 wt% and are inversely correlated with carbonate content (0–80 wt%).

Stratigraphic control was achieved using calcareous nannofossils and planktonic foraminifers; siliceous microfossils were not found. The 16 biostratigraphic events recognized in Hole 964A range in age from the late early Pliocene to the late Pleistocene. The occurrence of sapropel S1 in the uppermost section demonstrates that the Holocene is present. Based on composite depth, the resulting age vs. depth curve reveals that the sedimentation rate at Site 964 varied between 4 and 73 m/m.y., with an average of 30 m/m.y. Initial evaluation of planktonic foraminifers in sapropels, as compared to surrounding lithologies, suggests that these sapropels are characterized by unique environmental conditions at the sea surface and have distinct assemblages that differ between individual sapropels.

Constructing the magnetostratigraphic record at Site 964 was hampered by suspected overprints that could not be removed with the maximum fields that could be applied in the shipboard laboratory. However, the detailed records of individual holes hold promise for successful shore-based work on a composite section.

Sulfate is never depleted in the cores and methane concentrations are very low. Pore-water gradients point to some carbonate precipitation below 60 mbsf, however, and gradients of dissolved cations imply that solutions characteristic of late-stage brine, possibly derived from dissolving evaporites at depth, are present below the penetration depth of our holes.

The setting of the site at the toe of the Calabrian accretionary wedge carries significant tectonic information concerning the processes of final closure of the Ionian Basin, a Tethyan remnant. The cobblestone topography at Site 964 is clearly tectonically controlled in view of the evidence of high-angle normal faulting observed in the cores and inferred from the sedimentary record.

Site 964 was a success: we were able to compile a complete sequence of sedimentation since the late early Pliocene, which includes more than 50 sapropels and numerous discrete layers of tephra. The sequence recovered is calcareous and contains evidence for cyclic variations of conditions in the bottom water, an assumption that will be tested by benthic isotope and faunal analyses. The sapropels, some of which are extremely rich in organic carbon, will undoubtedly help answer questions related to the origin and significance of black shales in the Mesozoic oceans.

REFERENCES

Belderson, R.H., Kenyon, N.W., and Stride, A.H., 1972. Comparisons between narrow-beam and conventional echo-soundings from the Mediterranean Ridge. *Mar. Geol.*, 12:M11–M15.

Béthoux, J.-P., 1993. Mediterranean sapropel formation, dynamic and climatic viewpoints. *Oceanol. Acta*, 16:127–133.

Blechschmidt, G., Cita, M.B., Mazzei, R., and Salvatori, G. 1982. Stratigraphy of the Western Mediterranean and Southern Calabrian Ridges, Eastern Mediterranean. *Mar. Micropaleontol.*, 7:101–134.

Brassell, S.C., 1993. Applications of biomarkers for delineating marine paleoclimatic fluctuations during the Pleistocene. *In* Engel, M.H., and Macko, S.A. (Eds.), *Organic Geochemistry: Principles and Applications:* New York (Plenum), 699–738.

Camerlenghi, A., Cita, M.B., and Ricciuto, T.S., 1992. Geological evidence of mud diaprism on the Mediterranean Ridge accretionary complex. *Earth Planet. Sci. Lett.*, 109:493–506.

Castradori, D., 1993. Calcareous nannofossil biostratigraphy and biochronology in eastern Mediterranean deep-sea cores. *Riv. Ital. Paleontol. Stratigr.*, 99:107–126.

Cita, M.B., 1975. Planktonic foraminiferal biozonation of the Mediterranean Pliocene deep-sea record: a revision. *Riv. Ital. Paleontol. Stratigr.*, 81:527–544.

Cita, M.B., Maccagni, A., and Pirovano, G., 1982. Tsunami as triggering mechanism of homogenites recorded in areas of the eastern Mediterra-

nean characterized by "cobblestone topography." *In* Saxov, S., and Niewenhuis, J.K. (Eds.), *Marine Slides and Other Mass Movements.* NATO Conf. Ser. 4, Mar. Sci., 6:233–260.

Dekkers, M.J., Langereis, C.G., Vriend, S.P., van Santvoort, P.J.M., and de Lange, G.J., 1994. Fuzzy c-means cluster analysis of early diagenetic effects on natural remanent magnetization acquisition in a 1.1 Myr piston core from the Central Mediterranean. *Phys. Earth Planet. Inter.,* 85:155–171.

Emerson, S., and Hedges, J.I., 1988. Processes controlling the organic carbon content of open ocean sediments. *Paleoceanography,* 3:621–634.

Emery K.O., Heezen, B.C., and Allan, T.D., 1966. Bathymetry of the eastern Mediterranean Sea. *Deep-Sea Res.,* 13:173–192.

Finetti, I., 1982. Structure, stratigraphy and evolution of central Mediterranean. *Boll. Geofis. Teor. Appl.,* 24:247–315.

Gieskes, J.M., 1983. Interstitial waters of deep sea sediments. *In* Chester, J.P., and Riley, R. (Eds.), *Chemical Oceanography* (Vol. 6): New York (Academic), 221–269.

Higgs, N.C., Thomson, J., Wilson, T.R.S., and Croudace, I.W., 1994. Modification and complete removal of eastern Mediterranean sapropels by postdepositional oxidation. *Geology,* 22:423–426.

Hilgen, F.J., 1991a. Astronomical calibration of Gauss to Matuyama sapropels in the Mediterranean and implication for the geomagnetic polarity time scale. *Earth Planet. Sci. Lett.,* 104:226–244.

———, 1991b. Extension of the astronomically calibrated (polarity) time scale to the Miocene/Pliocene boundary. *Earth Planet. Sci. Lett.,* 107:349–368.

Hsü, K.J., Montadert, L., et al., 1978. *Init. Repts. DSDP,* 42 (Pt. 1): Washington (U.S. Govt. Printing Office).

Kastens, K.A., 1981. Structural causes of and sedimentological effects of "cobblestone topography" in the Eastern Mediterranean [Ph.D. dissert.]. Scripps Institution of Oceanography, La Jolla, CA.

Kastens, K.A., 1984. Earthquakes as a triggering mechanism for debris flows and turbidites on the Calabrian Ridge. *Mar. Geol.,* 55:13–33.

Kastens, K.A., and Cita, M.B., 1981. Tsunami-induced sediment transport in the abyssal Mediterranean Sea. *Geol. Soc. Am. Bull.,* 92:845–857.

Manheim, F.T., and Sayles, F.L., 1974. Composition and origin of interstitial waters of marine sediments based on deep sea drill cores. *In* Goldberg, E.D. (Ed.), *The Sea* (Vol. 5): New York (Wiley Interscience), 527–568.

McCoy, F.W., Jr., 1974. Late Quaternary sedimentation in the Eastern Mediterranean Sea [Ph.D. thesis]. Harvard University, Cambridge, MA.

McDuff, R.E., Gieskes, J.M., and Lawrence, J.R., 1978. Interstitial water studies, Leg 42A. *In* Hsü, K.J., Montadert, L., et al., *Init. Repts. DSDP,* 42 (Pt. 1): Washington (U.S. Govt. Printing Office), 561–568.

Mulder, C.J., Lehner, P., and Allen, D.C.K., 1975. Structural evolution of the Neogene salt basins in the Eastern Mediterranean and Red Sea. *Geol. Mijnbouw,* 54:208–221.

Murat, A., 1991. Enrégistrement sédimentaire des paléoenvironnements Quaternaires en Mediterranée Orientale [Ph.D. dissert.]. University of Perpignan, France.

Prahl, F.G., and Wakeham, S.G., 1987. Calibration of unsaturation patterns in long-chain ketone compositions for paleotemperature assessment. *Nature,* 330:367–369.

Rio, D., Sprovieri, R., and Di Stefano, E., 1994. The Gelasian stage: a proposal of a new chronostratigraphic unit of the Pliocene series. *Riv. Ital. Paleontol. Stratigr.,* 100:103–124.

Rohling, E.J., 1994. Review and new aspects concerning the formation of eastern Mediterranean sapropels. *Mar. Geol.,* 122:1–28.

Ryan, W.B.F., Hsü, K.J., et al., 1973. *Init. Repts. DSDP,* 13 (Pts. 1 and 2): Washington (U.S. Govt. Printing Office).

Sanvoisin, R., d'Onofrio, S., Lucchi, R., Violanti, D., and Castradori, D., 1993. 1 Ma paleoclimatic record from the Eastern Mediterranean—MARFLUX project: first results of a micropaleontological and sedimentological investigation of a long piston core from the Calabrian Ridge. *Il Quaternario,* 6:169–188.

Sikes, E.L., and Volkman, J.K., 1993. Calibration of alkenone unsaturation ratios ($U_{37}^{k'}$) for paleotemperature estimation in cold polar waters. *Geochim. Cosmochim. Acta,* 57:1883–1889.

Spaak, P., 1981. The distribution of the *Globorotalia inflata* group in the Mediterranean Pliocene. *Proc. K. Ned. Akad. Wet., Ser. B,* 84:201–215.

Spiegler, D., and Rögl, F., 1992. Bolboforma (Protophyta, incertae sedis) im Oligozän und Miozän des Mediterran und der Zentralen Paratethys. *Ann. Naturhist. Mus. Wien,* 94:59–95.

Sprovieri, R., 1993. Pliocene–early Pleistocene astronomically forced planktonic Foraminifera abundance fluctuations and chronology of Mediterranean calcareous plankton bio-events. *Riv. Ital. Paleontol. Stratigr.,* 99:371–414.

Stanley, D.J., 1977. Recent tectonic overprint on cobblestone deposition in the northwestern Hellenic arc. *In* Biju-Duval, B., and Montadert, L. (Eds.), *Structural History of the Mediterranean Basins.* Ed. Technip, 433–466.

Suess, E., 1980. Particulate organic carbon flux in the oceans: surface productivity and oxygen utilization. *Nature,* 288:260–263.

ten Haven, L., 1986. Organic and inorganic aspects of Mediterranean late Quaternary sapropels and Messinian evaporitic deposits [Ph.D. thesis]. University of Utrecht, The Netherlands. *Geol. Utraiectina,* 46.

ten Haven, H.L., Baas, M., de Leeuw, J.W., and Schenck, P.A., 1987. Late Quaternary Mediterranean sapropels, I. On the origin of organic matter in sapropel S_7. *Mar. Geol.,* 75:137–156.

Ms 160IR-105

NOTE: Core-description forms ("barrel sheets") and core photographs can be found in Section 5, beginning on page 535. Forms containing smear-slide data can be found in Section 6, beginning on page 951. Color reflectance, physical properties, chemistry, and thin-section data are presented on the CD-ROM (back pocket).

Table 12. Index properties measured on the cores from Hole 964A.

Core, section, interval (cm)	Depth (mbsf)	Water content (wt%)	Porosity (vol%)	Bulk density (g/cm³)		Grain density (g/cm³)		Dry density (g/cm³)	
				Method B	Method C	Method B	Method C	Method B	Method C
160-964A-									
1H-2, 20–22	1.70	38.13	61.63	1.76	1.07	3.14	1.10	1.09	0.66
1H-5, 20–22	6.20	41.49	70.91	1.62	0.99	2.77	0.96	0.95	0.58
2H-2, 20–22	8.50	32.56	48.28	1.97	1.85	3.57	3.02	1.33	1.25
2H-5, 20–22	13.00	37.83	60.85	1.78	1.71	3.22	2.87	1.11	1.06
3H-2, 20–22	18.00	37.65	60.38	1.84	1.71	3.52	2.88	1.15	1.07
3H-5, 20–22	22.50	33.95	51.41	1.88	1.79	3.30	2.92	1.24	1.18
4H-2, 20–22	27.50	34.50	52.66	2.00	1.79	4.04	2.93	1.31	1.17
4H-5, 20–22	32.00	35.60	55.29	1.83	1.74	3.23	2.83	1.18	1.12
5H-2, 139–141	38.19	33.51	50.40	1.58	1.76	2.17	2.76	1.05	1.17
5H-5, 130–132	42.60	32.42	47.98	1.75	1.78	2.66	2.75	1.18	1.20

Only part of this table is reproduced here. The entire table appears on the CD-ROM (back pocket).

Table 13. Compressional wave velocity measured in cores from Hole 964A.

Core, section, interval (cm)	Depth (mbsf)	Measurement type	Velocity (km/s)
160-964A-			
1H-2, 22.5	1.73	DSV 1	1.55
1H-2, 23.5	1.74	DSV 2	1.571
1H-5, 25.8	6.26	DSV 1	1.531
1H-5, 26.7	6.27	DSV 2	1.52
2H-2, 28	8.58	DSV 2	1.44
2H-2, 28.5	8.59	DSV 1	1.549
2H-5, 29	14.38	DSV 1	1.578
2H-5, 29	14.41	DSV 2	1.561
3H-2, 27.9	18.08	DSV 1	1.544
3H-2, 29.3	18.09	DSV 2	1.551

Note: Direct DSV measurements.

Only part of this table is reproduced here. The entire table appears on the CD-ROM (back pocket).

Table 14. Vane shear strength measured in cores from Hole 964A.

Core, section, interval (cm)	Depth (mbsf)	Strength (kPa)
160-964A-		
1H-2, 22.6	1.73	5.6
1H-5, 26.4	6.27	7.4
2H-2, 26.9	8.57	9.3
2H-2, 114.2	9.44	16.4
3H-2, 26.7	18.07	14
3H-5, 26	22.56	20.6
4H-2, 26.8	27.57	22.5
4H-5, 29.1	32.09	20.9
5H-2, 146.5	38.27	26.2
5H-5, 128.5	42.59	22.9

Only part of this table is reproduced here. The entire table appears on the CD-ROM (back pocket).

Table 15. Thermal conductivity measured in cores from Hole 964A.

Core, section, interval (cm)	Depth (mbsf)	Thermal conductivity (W/[m · K])
160-964A-		
1H-2, 50	2.00	1.20
1H-5, 50	6.50	1.10
2H-2, 50	8.80	1.18
2H-5, 50	13.30	1.07
3H-2, 50	18.30	1.44
3H-5, 50	22.80	1.15
4H-2, 50	27.80	0.95
4H-5, 50	32.30	1.15
5H-2, 50	37.30	1.24
5H-5, 50	41.80	1.05

Only part of this table is reproduced here. The entire table appears on the CD-ROM (back pocket).

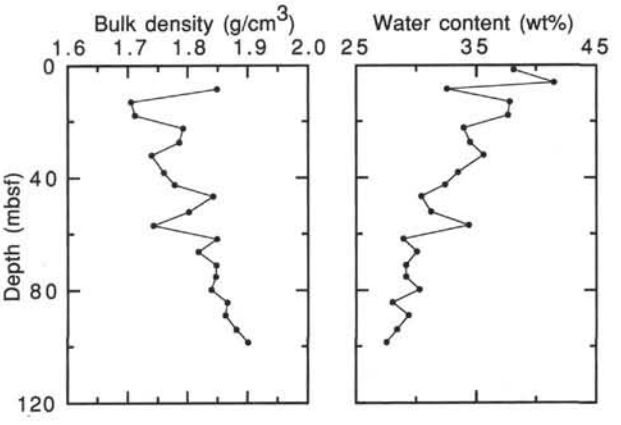

Figure 38. Index properties measured in cores from Hole 964A.

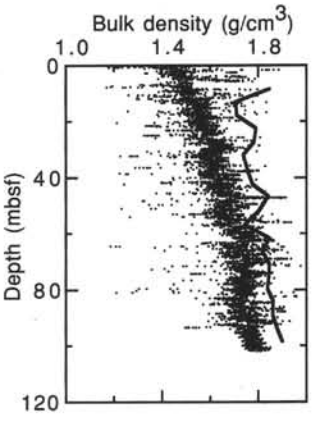

Figure 39. Bulk density measured with the GRAPE and from index property measurements (line).

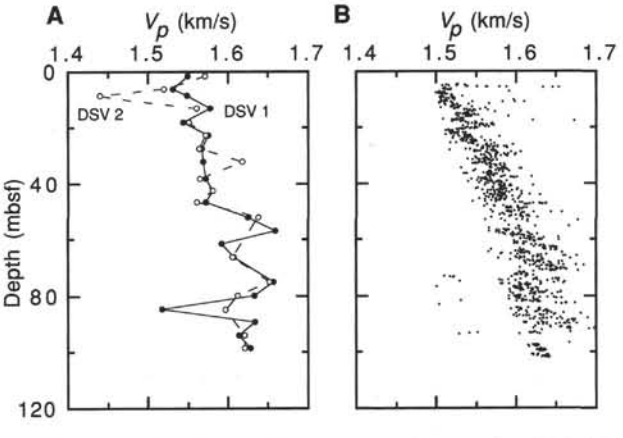

Figure 40. Compressional wave velocity measured in cores from Hole 964A. **A.** Direct measurement in split core sections. DSV 1 = parallel to core axis; DSV 2 = perpendicular to core axis. **B.** MST measurements through the liner of whole core sections (perpendicular to core axis).

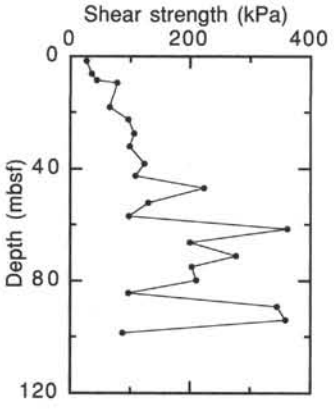

Figure 41. Vane shear strength measured in cores from Hole 964A.

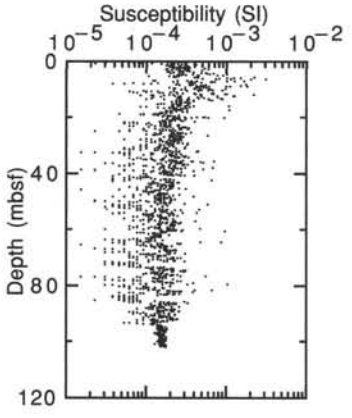

Figure 42. Magnetic susceptibility measured with the MST on cores from Hole 964A.

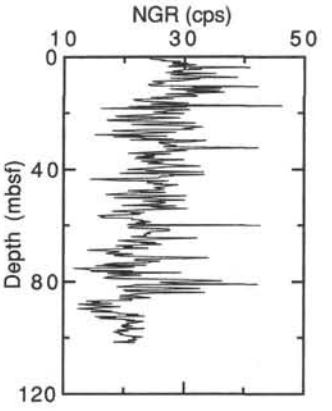

Figure 43. Natural gamma-ray radiation measured with the MST on cores from Hole 964A.

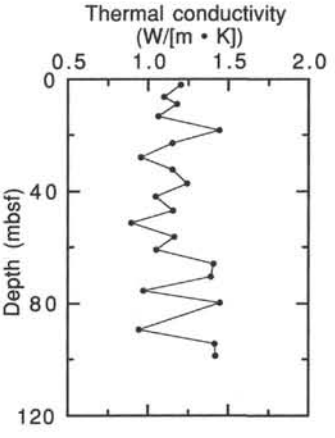

Figure 44. Thermal conductivity measured in cores from Hole 964A.